

Politecnico di Torino

DEPARTMENT OF MECHANICAL AND AEROSPACE ENGINEERING
MASTER OF SCIENCE IN AEROSPACE ENGINEERING

Investigating the local heat transfer effects on an upscaled additively manufacturing induced roughness surface

Supervisors

Prof. Dario PASTRONE

Prof. Andrea FERRERO

Dr.-Ing. Mats KINELL

Candidate

Beniamino MECJA

In collaboration with

SIEMENS energy

July 2026

Abstract

Siemens Energy AB is leading the energy transition by developing cutting-edge technologies to make this shift faster. This thesis work focuses on gas turbines and the approaches involved in the company's current R&D efforts.

Additive Manufacturing (AM) is becoming a very interesting technology for the design of gas turbine cooling channels, enabling the production of very complex geometries at a relatively low cost. AM has the potential to replace conventional manufacturing methods, thereby increasing the operational life of the component, reducing maintenance operations, and boosting the performance of the machine.

The key aspect of AM is the surface roughness (SR) originating during the process, which can significantly enhance heat transfer mechanisms. For this reason, at *Siemens Energy*'s Fluid Dynamics Laboratory, the Surface Roughness Heat Transfer (SRHT) rig was designed to evaluate the effects of SR parameters on heat transfer. By using Infrared Thermography (IRT), the local behavior of heat transfer can be investigated. Unlike the test samples studied in other rigs within the Fluid Dynamics Laboratory, the SRHT rig employs upscaled models derived from real AM components. At this stage of the research, *Siemens Energy* aims to understand which SR parameters most significantly influence convective heat transfer. In this work, the effects of roughness element density were investigated alongside their size. Initially, these SR parameters were studied separately and subsequently combined together. This provided a deeper understanding of how the same heat transfer coefficient (HTC) distribution can be reached with different geometry configurations.

The rig has not undergone any significant modifications since it was first lengthened by Gissi. The positions of the thermocouples were reviewed and slightly changed for better temperature measurements along the duct. Furthermore, a sensitivity analysis was conducted regarding the camera inclination. Although the results are influenced by this tilt, the resulting error can be mitigated through a proper camera setup. Moreover, thermal boundary layer plots are presented, alongside comparisons with the Particle Image Velocimetry (PIV) rig to gain a deeper insight into heat transfer phenomena from a fluid-dynamic perspective. Additionally, a comparison with the quasi-Steady State Heat Transfer (qSSHT) rig is included to show how different methodologies lead to the same results. Finally, to continue the parametric study, new models were designed and manufactured to expand the available dataset.

Contents

1 Introduction **1**
- 1.1 Motivation . . . 1
- 1.2 Literature Review . . . 3
- 1.3 Research Objectives . . . 5
- 1.4 Thesis Outline . . . 5

2 Theoretical Background **7**
- 2.1 Gas Turbine . . . 7
- 2.2 Turbine Blade Cooling . . . 11
  - 2.2.1 Internal Cooling . . . 12
  - 2.2.2 External Cooling . . . 14
  - 2.2.3 Thermal Barrier Coating . . . 14
- 2.3 Additive Manufacturing . . . 15
- 2.4 Roughness Parameters . . . 19
  - 2.4.1 Roughness Heigh Parameters . . . 21
  - 2.4.2 Roughness Density Parameters . . . 23
  - 2.4.3 Roughness Spectral Parameters . . . 24
- 2.5 Fundamentals of Heat Transfer . . . 26
  - 2.5.1 Conduction . . . 26
  - 2.5.2 Convection . . . 28
  - 2.5.3 Radiation . . . 29
- 2.6 Infrared Thermography IRT . . . 30
  - 2.6.1 Black Body Radiation . . . 31
  - 2.6.2 Realy Body Radiation . . . 33
  - 2.6.3 IR Scanner . . . 34
- 2.7 Boundary Layer Theory . . . 35
  - 2.7.1 Laminar and Turbulent Flows . . . 36
  - 2.7.2 Momentum Boundary Layer . . . 37
  - 2.7.3 Thermal Boundary Layer . . . 39
  - 2.7.4 Turbulent Flow over Rough Surface . . . 42
- 2.8 Wall Bounded Turbulent Flows . . . 45
  - 2.8.1 Heat Transfer Correlations . . . 49

3 Research Methodology **51**
3.1 SRHT Rig . . . 51
3.2 Working Principle . . . 52
3.3 Analogue Rough Surface Modelling . . . 54
3.4 SRHT-rig Setup . . . 56
3.4.1 Test Rig . . . 58
3.4.2 Heater . . . 59
3.4.3 IR Camera . . . 59
3.4.4 IR Window . . . 63
3.4.5 IR Paint . . . 63
3.4.6 Data Acquisition Systems . . . 64
3.5 Experimental Data Acquisition . . . 65
3.6 Data Processing . . . 66
3.6.1 IR Video . . . 66
3.6.2 Mapping . . . 68
3.6.3 C3D Software . . . 70
3.6.4 Underlying Equations . . . 75
3.7 Uncertainty Analysis . . . 77

4 Experimental Results **83**
4.1 Rig Modification . . . 83
4.2 Nusselt Results . . . 85
4.3 Density Effect . . . 92
4.4 Thermal Boundary Layer . . . 95
4.5 PIV Comparison . . . 100
4.6 qSSHT Comparison . . . 103

5 Conclusion and Future work **105**
5.1 Conclusion . . . 105
5.2 Future Work . . . 105

Bibliography **109**

Nomenclature **117**

List of Figures

1.1 Global average annual energy investment by sector and technology in the Net Zero Emission (NZE) Scenario [72] . . . 2
1.2 Comparison between the number of publications per year on rough-wall heat and momentum transfer [87] . . . 4

2.1 Siemens Energy SGT-700 [93] . . . 8
2.2 The Brayton thermodynamic cycle [28] . . . 10
2.3 Overall cycle efficiency as a function of the firing temperature and pressure ratio[36] . . . 10
2.4 Evolution of turbine blade cooling technology [74] . . . 11
2.5 Different representations of gas turbine blade cooling technologies [42] 12
2.6 Various high performance rib turbulators [21] . . . 13
2.7 Schematic of film-cooling concept . . . 14
2.8 Global AM market trend [58] . . . 15
2.9 Overall workflow of the additive manufacturing process [76] . . . 16
2.10 Angled SEM micrographs of an Inconel coupon detailing roughness features [50] . . . 17
2.11 Metallic AM techniques classification based on the form of metallic materials employed [58] . . . 18
2.12 Surfaces with different wavelengths but the same amplitude [87] . . . 19
2.13 Examples of 2D and 3D roughness elements . . . 20
2.14 Surface Roughness height profile . . . 21
2.15 Surface sketches to illustrate frontal solidity and plan solidity [85] . . . 23
2.16 Surface sketches to illustrate spectral parameters [85] . . . 25
2.17 Conduction, convection, and radiation heat transfer modes [37] . . . 26
2.18 Schematic representation of heat conduction through a wall . . . 27
2.19 One-dimensional assumption for conduction heat transfer . . . 27
2.20 Schematic representation of convection mode . . . 28
2.21 Convection classification [37] . . . 29
2.22 Spectrum of electromagnetic radiation [37] . . . 30
2.23 Spectral blackbody emissive power . . . 32
2.24 Comparison between a blackbody and a real surface: (a) spectral distribution and (b) directional distribution . . . 33
2.25 Infrared scanning radiometer scheme [94] . . . 34

2.26 Development of velocity and temperature boundary layer 35
2.27 Boundary layer transition 36
2.28 Normalized velocity profile u^+ vs y^+ [25] 39
2.29 Turbulent rough flows regimes 42
2.30 Equivalent sand-grain roughness 43
2.31 Schematic of rough-wall boundary layer problem 44
2.32 Mean velocity profiles of experimental turbulent flows over 2D bars and 3D mesh [33, 35] 45
2.33 Hydrodynamic boundary layer development in a circular tube 46
2.34 Moody Diagram 48
2.35 Thermal boundary layer development in a heated circular tube 49
2.36 Axial variation of the convective heat transfer coefficient for flow in a tube 49

3.1 Schematic representation of the SRHT rig operation [86] 52
3.2 Schematic diagram of the SRHT rig 53
3.3 Typical bulk flow *Re* spectrum for natural and industrial heat transfer [87] 54
3.4 Surface roughness measurements 54
3.5 SEM images 55
3.6 CAD models of the upscaled surface roughness plates 57
3.7 CAD model of the SRHT rig 59
3.8 IR camera focus procedure 61
3.9 IR camera and calibration device 62
3.10 IR camera calibration curve and its regression error [86] 62
3.11 Top view of the IR window 63
3.12 Data Acquisition System 64
3.13 Elliptical ROI 67
3.14 Reference Points 67
3.15 Schematic representation of the main contributions to the detected signal 69
3.16 Mesh of the reduced CAD model in *Siemens NX* 69
3.17 Mapping Procedure 72
3.18 C3D Mapping Region 73
3.19 Temperature field after conjugate simulation 74
3.20 HTC spatial distribution after the calibration simulation 74
3.21 Globally avereged Nusselt number for each test 80
3.22 Laterally averaged Nusselt number along the streamwise direction for all five tests 80
3.23 (a) Mean local Nusselt number spatial distribution over the five test cases. (b) Standard deviation of the local Nusselt number. (c) Percentage error of the local Nusselt number 81

4.1 Modification of the final thermocouple position 84
4.2 Transient thermocouple's temperature readings 84
4.3 Globally averaged Nu along streamwise direction $Re = 25000$ 86
4.4 Globally and laterally averaged Nu along streamwise direction $Re = 25000$ 87

4.5 Globally and laterally averaged Nu along streamwise direction $Re = 10000$ 87
4.6 Experimental Nusselt Map $Re = 25000$ 89
4.7 Experimental Nusselt Enhancement Map $Re = 25000$ 90
4.8 Experimental Nusselt Map comparison between the four rough models at $Re = 25000$ and in the last window 91
4.9 Spatial density calculation from the CAD model 92
4.10 Density Effect on the $Nu - Re$ plot for Rz_{015} 94
4.11 Density Effect on the $Nu - Re$ plot for Rz_{030} 94
4.12 Reynolds Effect on the $Nu - A_s/A_{tot}$ plot for Rz_{015} 95
4.13 Reynolds Effect on the $Nu - A_s/A_{tot}$ plot for Rz_{030} 96
4.14 $Nu - Re$ plot with all the parametric geometries tested in the SRHT rig 96
4.15 Geometry Comparison 97
4.16 Thermal boundary layer rake 98
4.17 Thermal boundary layer profile for Rz_{015} 99
4.18 Thermal boundary layer profile for Rz_{030} 99
4.19 Mean flow streamlines obtained from PIV data that depicts the organization of the various recirculation regions around ribs of varying length [59] 100
4.20 Surface spots analyzed for the PIV comparison 101
4.21 Mean Velocity Field from PIV results [92] 101
4.22 Vortex Shedding behind Spot 1 [92] 102
4.23 Smooth test objects comparison between SRHT and q-SSHT rigs 103

5.1 Geometrical Plot 106

List of Tables

2.1 Infrared spectral bands 31
2.2 Values of roughness Reynolds number limits for different roughness types 42

3.1 Rough test object dimensions. 56
3.2 Python code parameters for rough model generation 58
3.3 Surface roughness parameters of the analyzed configurations 58
3.4 Flow straightener dimensions 59
3.5 Test section's geometrical dimensions. 60
3.6 Accura Xtreme Grey thermal properties in axial and radial directions . 60
3.7 *Titanium 560M technical details* 61
3.8 Values of the fitting curve parameters 62
3.9 Optical properties of the IR window and black paint 63
3.10 Experimental and Fluid-Dynamic Conditions 66
3.11 Mesh Generation Properties 71
3.12 Boundary conditions applied to the numerical model 72
3.13 Angles setup for sensitivity analysis 79

4.1 SR parameters of the investigated roughness models 93

Chapter 1

Introduction

In this chapter, the objectives and the motivations of the present thesis work, conducted at *Siemens Energy AB* Fluid Dynamics Laboratory, are presented. A brief review of the relevant literature is provided to better understand the current state of research. The chapter concludes with an outline of the thesis structure.

1.1 Motivation

Every industrial sector is involved in the energy transition. The global electricity demand is expected to double over the next 20 years according to the *International Energy Agency* [72].

Renewable energy sources emerge as a feasible solution for this demanding goal. According to Figure 1.1 investments increase rapidly in electricity, infrastructure and end-use sectors; fossil fuel investments decrease and low-emissions fuel investments increase. Thanks to their versatility, gas turbines find extensive application across many industrial sectors involved in the energy transition. They are making a substantial contribution in the power generation sector, particularly in combined-cycle power plants, where their high efficiency contributes to reducing greenhouse gas emissions. Gas turbines are also increasingly important in the aviation industry, where the adoption of sustainable aviation fuels and other low-carbon fuel concepts is being actively explored. In addition, they are employed in a wide range of industrial applications, as extensively discussed in [72].

The analysis presented in Papapetrou at al. [60] provides insights into the potential for waste heat exploitation, especially at low temperature range, which can be used as a first indication of the market size for technologies that can recover and use heat, either upgrading it (heat pumps) or converting it to electricity (heat to power engines).

Siemens Energy has invested heavily in R&D to enhance gas turbine efficiency. Key initiatives include the adoption of sustainable alternative fuels, research into advanced

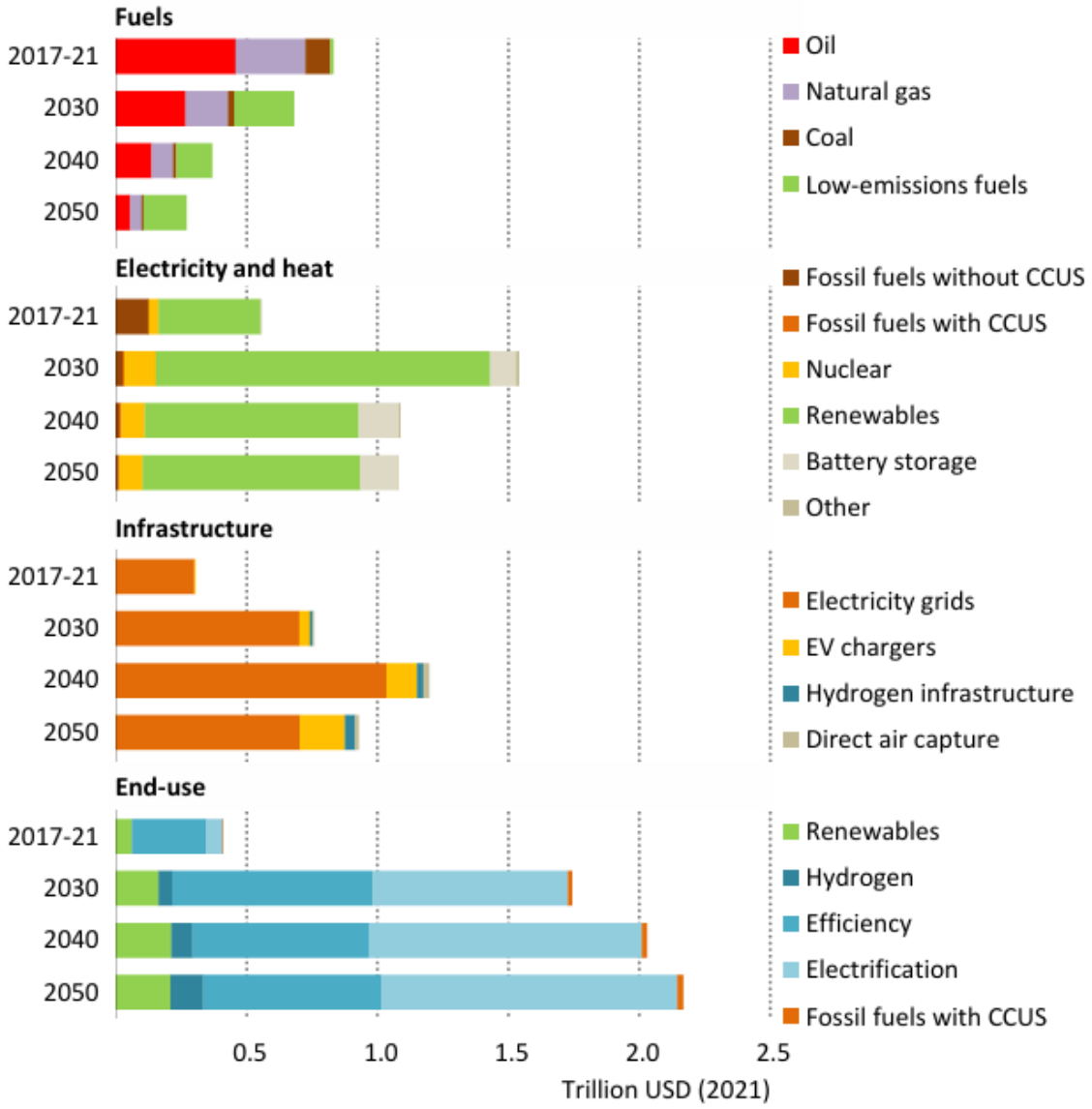


Figure 1.1: Global average annual energy investment by sector and technology in the Net Zero Emission (NZE) Scenario [72]

alloys and manufacturing processes, and the development of new engineering methodologies.

Additive Manufacturing is undoubtedly an emerging process that can improve the thermal performance and, more importantly, the efficiency of gas turbines. While the induced SR is beneficial for heat transfer, the resulting pressure losses must be carefully assessed. From an AM component, it is possible to evaluate several surface roughness parameters through many methods. Not only understanding the main mechanism involved in convective heat transfer, but also identifying the most relevant SR parameters is the main objective of this experimental work.

1.2 Literature Review

This section provides a brief overview of past and current research on convective heat transfer. In the literature, many studies are available on the effects of surface roughness unrelated to the AM process, where both real and artificially created roughness have been investigated.

One of the pioneering works was conducted by Nikuradse [3, 6], where the concept of *sand grain roughness* was introduced. Many experiments were carried out covering pipes, channels and flat surfaces with small, uniform sand grains. In this way, the effect of roughness on pressure losses was estimated. Colebrook and White [5] introduced the concept of *equivalent sand-grain roughness*, which enables the representation of real roughness with the sand grain concept that produces the same hydraulic losses. Surface roughness can significantly influence fluid dynamics and heat transfer in convective flows by inducing perturbations in the velocity profile, which affect surface drag, turbulent mixing, and heat transfer [70]. The study of roughness in turbulent flows was pioneered by Hagen and Darcy [1, 2] who found that roughness affected pressure drop by increasing the drag force and blockage effects [70, 97].

Accurate and reliable correlations for both friction factors and heat transfer coefficients are crucial for engineering calculations, especially for gas turbine cooling channels. Developing these correlations requires high-quality experimental data, high-fidelity numerical simulations, and in-depth studies to enhance the understanding of flow dynamics. Stimpson et al. [48] investigated the effects of surface roughness on both the fluid dynamics and heat transfer characteristics in Direct Metal Laser Sintering (DMLS) channels. Several flow conditions, channel shapes, and materials were investigated, and the results were presented in terms of friction factors and Nusselt numbers. Pagani [73] investigated the thermo-hydraulic performance of both straight and complex mini-channels manufactured via Selective Laser Melting (SLM), proposing a new friction factor correlation for straight channels. Kadivar et al. [88] studied the influence of roughness density and Prandtl number on Laser-based Powder Bed Fusion (L-PBF) rough samples. The work comprises both an experimental and numerical evaluation. Heat transfer and flow friction were observed to increase with roughness density until reaching an asymptotic upper limit across all Prandtl values. The inves-

tigation of regular multiscale cuboid elements was performed by Medjnoun et al. [71] to assess the velocity field and drag reduction with a power-law decreasing element size.

Several researchers have studied the influence of key surface roughness parameters on turbulent flows. Regarding drag reduction, Flack et al. [44] experimentally analyzed the effect of modifying surface skewness. From the previous work of the authors, they confirmed that both root-mean-square roughness height and skewness represent key parameters for scaling the skin friction factor. Effective slope on ratchet-type surface was analyzed by Zhdanov [90], using a numerical approach. The results reveal a significant impact on the mean flow field around the ratchet canopy. One of the few experimental studies that closely resembles the work developed in this thesis is the aerodynamic and heat transfer investigation on distributed hemispherical roughness elements. Leon et al. [63] kept the geometric configuration unaltered and varied the ratio of boundary layer thickness to roughness height. Modifying the fluid-dynamic conditions under a constant geometry setup enabled the prediction of mean friction coefficients and the formulation of a Stanton number correlation for the investigated coupons.

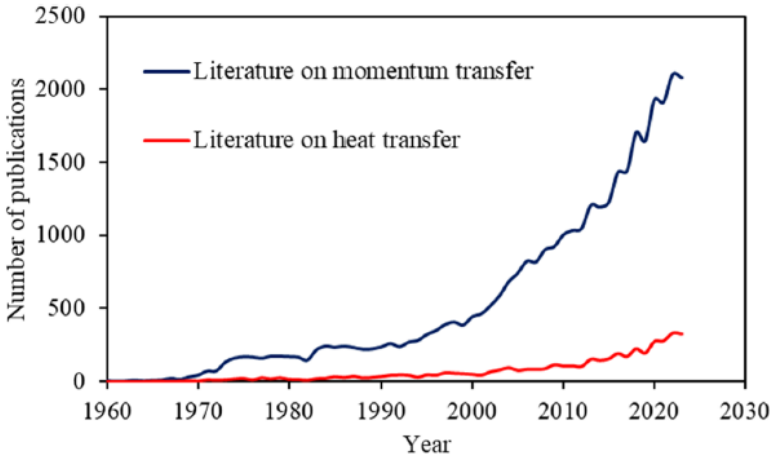


Figure 1.2: Comparison between the number of publications per year on rough-wall heat and momentum transfer [87]

In the aforementioned experimental and numerical works, several researchers have studied the effects of AM processes and the impact of key surface roughness (SR) parameters on regular roughness distributions. To address the gap in heat transfer literature highlighted in Figure 1.2, this thesis continues the parametric study started by Jankovskis [91]. In his experimental campaign the effect of roughness element size was analyzed. Key SR parameters affecting heat transfer are analyzed to generate a dataset for developing accurate correlations for randomly distributed rough elements. The spatial density distribution of the spheres was studied here, alongside particle height.

The challenge of convective heat transfer over rough walls involves accurately pre-

dicting both skin friction and heat transfer characteristics. Currently, no universal predictive method exists due to an incomplete understanding of the effects of diverse roughness topologies on the flow. For this reason, the experimental work carried out in the SRHT rig aims to understand flow behavior on different rough configurations from a heat transfer perspective.

1.3 Research Objectives

In this experimental work, many aspects related to heat transfer effects on AM components were studied. The research questions are listed below, and this thesis was developed based on them.

- Which are the mechanisms that mostly influnce the convective heat transfer on additively manufactured components?
- Which SR parameters mostly impact convective heat transfer in the upscaled models?
- In what way the roughness impact on both the thermal boundary layer and fluid dynamic behavior?

While many of these questions have been addressed, several complex aspects have yet to be fully understood. Moreover, as future research involves testing new geometries, additional SR parameters will be incorporated into the discussion.

1.4 Thesis Outline

The structure of the present work is listed below:

- *Chapter 2* provides the theoretical background, beginning with an overview of gas turbines and advancing to AM processes, convective heat transfer theory, IRT methodologies, and fundamental fluid dynamics.
- *Chapter 3* details the methodology employed in the SRHT rig.
- *Chapter 4* presents the final results, including the modifications that the SRHT rig has undergone.
- *Chapter 5* summarizes the main results and outlines recommendations for future developments.

Chapter 2

Theoretical Background

This chapter provides the theoretical framework and the physical principles underlying the experimental work developed in this study. The chapter begins with an introduction to the fundamental concepts of gas turbines, followed by an overview of Additive Manufacturing (AM) processes, highlighting their key advantages and limitations. Subsequently, a comprehensive classification of surface roughness parameters is established.

The second part of the chapter focuses on the heat transfer concepts required for the present investigation, followed by an introduction to Infrared Thermography (IRT), which represents the primary measurement technique employed in the SRHT rig. Finally, an overview of turbulent boundary layer theory is provided, particularly on wall-bounded turbulent flows.

2.1 Gas Turbine

Gas turbines are used for aircraft propulsion and power generation [36]. Significant progress in gas turbine technology has been reached through continuous developments in material engineering, coating systems, and advanced cooling methodologies. However, the aerothermal design of advanced gas turbines remains a complex challenge.

The operation of a gas turbine is governed by the *Brayton thermodynamic cycle*. For simple power generation applications, a generator is normally coupled to the gas turbine, whereby the mechanical work generated by the turbine is converted to useful electrical energy. In aviation the exhaust gases are used to produce thrust. The main components of a gas turbine are listed below and shown in Figure 2.1:

- *Air Intake System*: by drawing clean and filtered air into the machine, the air intake system safeguards the compressor section against dust and contaminants.
- *Compressor Section*: it increases the pressure of the incoming air before combus-

tion. Higher-pressure air improves fuel burning and helps achieve greater power output.

- *Combustion Chamber*: it mixes high-pressure air with fuel and ignites the mixture to produce high-temperature gases.
- *Turbine Section*: the turbine blades extract energy from the expanding hot gases and they are the most stressed components from an aerothermal and structural point of view.
- *Exhaust System*: once the energy is extracted by the turbine blades, the remaining gases are released through the exhaust and, in a combined cycle power plant, hot gases are used to generate additional power thanks to a steam turbine.

The turbine and compressor sections are mechanically connected through a shaft. The shaft transfers mechanical power from the expanding gases to the rotating elements and the generator. Any shaft imbalance or failure can lead to serious turbine shutdowns, making alignment and vibration monitoring essential [95]. The *Fuel System* controls fuel delivery to the combustion chamber. *Bearing and Lubrication System* support the rotating shaft, reducing friction between moving parts, and ensuring smooth operation and adequate cooling, respectively.

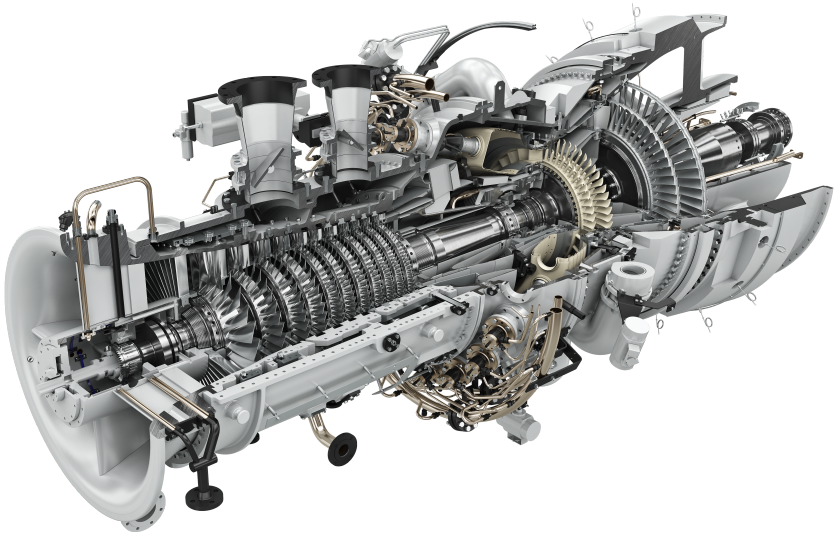


Figure 2.1: Siemens Energy SGT-700 [93]

The ideal Brayton cycle consists of two isentropic and two isobaric processes. The two isentropic processes refer to the compression and expansion while the two isobaric processes represent the combustion and the exhaust processes. When a heat recovery

device, such as a heat exchanger, is mounted downstream of the exhaust section, the plant operates as a cogeneration or combined-cycle system. Conversely, if no heat recovery system is present, the gas turbine operates in a standard open cycle.

Using a simplified version of the first law of thermodynamics to the air-standard Brayton cycle, assuming no changes in kinetic and potential energies and so working with a steady state flow process, it is possible to express the work of compressore W_c, the work of the turbine W_t and the heat added to the system Q_{23} as enthalpy differences, as reported in the following equations:

$$W_c = \dot{m}_a(h_2 - h_1)$$
$$W_t = (\dot{m}_a + \dot{m}_f)(h_3 - h_4)$$
$$Q_{2,3} = \dot{m}_f \times \mathrm{LHV}_{\mathrm{fuel}} = (\dot{m}_a + \dot{m}_f)h_3 - \dot{m}_a h_2$$

where $\dot{m}_a$ is the air mass flow, $\dot{m}_f$ is the fuel mass flow, $\mathrm{LHV}_{\mathrm{fuel}}$ is the lower heating value of the fuel. The total output work W_{cyc} is defined as:

$$W_{cyc} = W_t - W_c$$

The overall adiabatic thermal cycle efficiency can be written:

$$\eta_{cyc} = \frac{W_{cyc}}{Q_{23}}$$

The two main drivers for increasing gas turbine efficiency are the pressure ratio r_p and the turbine inlet temperature (TIT). By introducing the cold air-standard assumptions (such as constant specific heats), the expression for thermal efficiency can be simplified as a function of the pressure ratio alone, thereby thermal efficiency of the ideal cycle.

$$\eta_{\mathrm{ideal}} = \left(1 - \frac{1}{r_p^{\frac{\gamma-1}{\gamma}}}\right)$$

where γ is the ratio of the specific heats. Considering the same pressure ratio between the compressor and the turbine and using the isentropic equation it is possible to write the ideal thermal efficiency as:

$$\eta_{ideal} = 1 - \frac{T_4}{T_3}$$

Figure 2.3 shows the combined effects of the pressure ratio and TIT on the overall adiabatic thermal cycle efficiency. The efficiency tends to increase as the pressure ratio

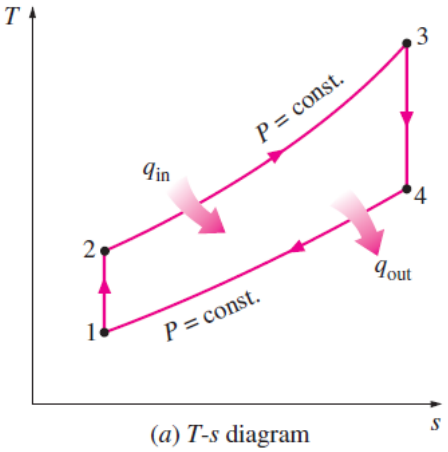


Figure 2.2: The Brayton thermodynamic cycle [28]

increases, for a fixed TIT. However, increasing the pressure ratio beyond the optimal value at any given TIT can actually result in lowering the overall cycle efficiency. Furthermore, an excessive pressure ratio leads to critical issues, such as overheating the air in the compressor section, not having enough cold air for turbine cooling and inducing fluid dynamic instabilities. For these reasons the gas turbine industry is focusing on technologies that can enable higher TIT.

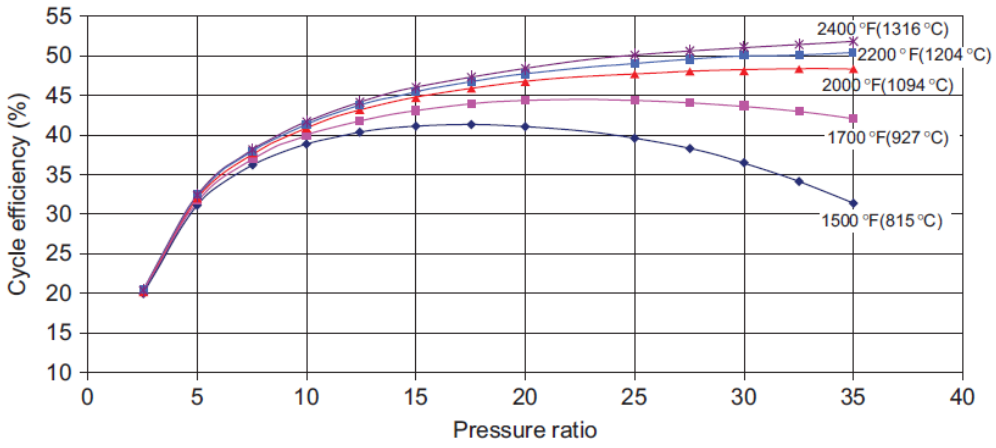


Figure 2.3: Overall cycle efficiency as a function of the firing temperature and pressure ratio[36]

For actual gas turbine applications, the overall thermal efficiency can be expressed by incorporating the efficiencies of both the compressor and the turbine into the cycle analysis:

$$\eta_{\text{real}} = \left(1 - \frac{1}{r_p^{\frac{\gamma-1}{\gamma}}}\right) \cdot \frac{\eta_t T_3 - \frac{T_1}{\eta_c} r_p^{\frac{\gamma-1}{\gamma}}}{T_3 - T_1 - \frac{T_1}{\eta_c}\left(r_p^{\frac{\gamma-1}{\gamma}} - 1\right)}$$

Further informations about real cycle gas turbine, combined cycle and gas turbine performance can be found in [28, 36]

2.2 Turbine Blade Cooling

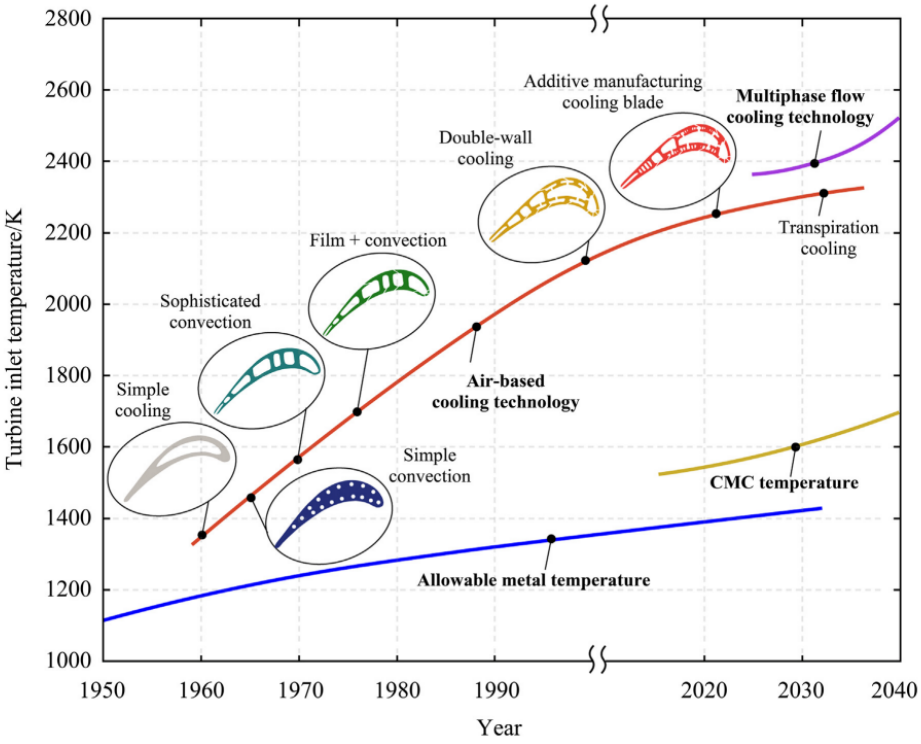


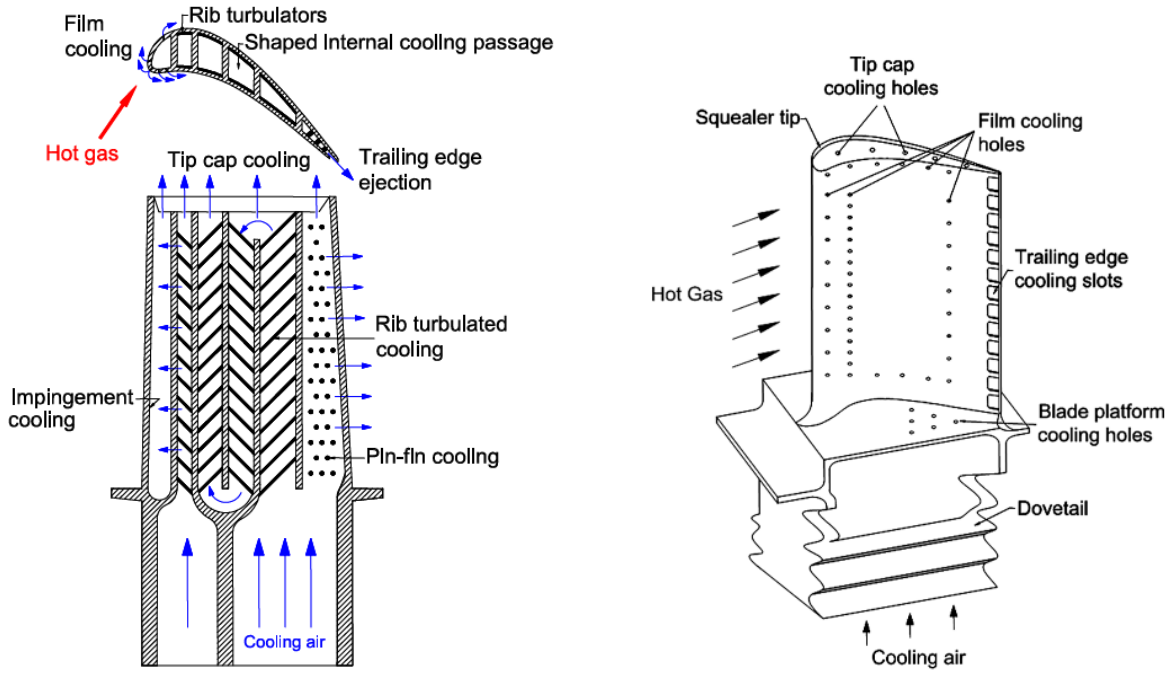
Figure 2.4: Evolution of turbine blade cooling technology [74]

Modern gas turbines work under demanding high temperatures, high pressures and high rotational speeds in order to improve thermal efficiency and power output. Since the temperature distribution on the turbine blades is not uniform, a combination of various cooling techniques is necessary. Figure 2.5(a) shows the combination of both internal and external cooling methods. This section aims to present the most consolidated cooling technologies adopted in gas turbines applications.

Over the past decades the TIT has increased to over 1900 K, far exceeding the allowable temperatures of turbine blade material. Figure 2.4 reportes the evolution over the last years of the cooling technologies. The three main categories into which cooling technologies can be divided are:

- *Internal Cooling*: the bleed air passes through internal channels inside the blade, removing heat via forced convection.
- *External Cooling*: the cooling air exits through small holes on the blade's surface, creating a protective thin layer of cooler air that protects the component from the hot gas stream.
- *Thermal Barrier Coating (TBC)*: a thin layer of a ceramic, high-temperature resistant material is applied to the blade surface to extend component lifespan and allow for higher operating temperatures.

2.2.1 Internal Cooling



(a) Schematic 2D cooling flow

(b) 3D blade cooling scheme

Figure 2.5: Different representations of gas turbine blade cooling technologies [42]

The cooling air is forced to pass through internal channels, removing heat via forced convection. The earliest cooling schemes employed smooth, circular passages. Significant advancements were made based on the concept of heat transfer surface area augmentation. In this framework, the induced SR from AM processes can play a key role in future cooling technologies. Apart from the forced air through complex internal channels of the turbine blades, other methods are employed together such as jet impingement, rib turbulators and pin-fins.

Jet Impingement is commonly used in the leading edge region, where the stagnation of the mainstream gas produces high heat loads on the airfoils. The cooling air passes

through discrete holes, forming high-velocity jets that impact directly against the internal target surface of the blade. In recent years, impingement studies have considered the use of non-circular holes in the creation of discrete jets.

Rib Turbulators are largely employed along the mid-chord of the turbine blades airfoil. They constantly trip the boundary layer and force it to reattach to the surface downstream of the rib. The first ribs implemented were oriented perpendicular to the coolant flow. Skewing the ribs, so they are angled with respect to the cooling air, provided increased heat transfer enhancements [14, 15, 18]. The secondary flows that originates promote mixing between hot and cold air. In Figure 2.6 several rib turbulator configurations are shown, including *V-shape* ribs, continuous and broken ribs. These studies have confirmed the initial finding that broken ribs outperform continuous ribs, and V-shaped ribs offer superior performance compared to angled ribs.

Pin-Fins are used in the trailing edge region where very high thermal loads occur in a confined space [42]. They simultaneously extend the heat transfer surface area and provide structural support between the pressure and suction sides. The thermal enhancement is driven by both intense flow turbulence through the pin matrix and the generation of localized three-dimensional horseshoe vortices at the pin-endwall junctions.

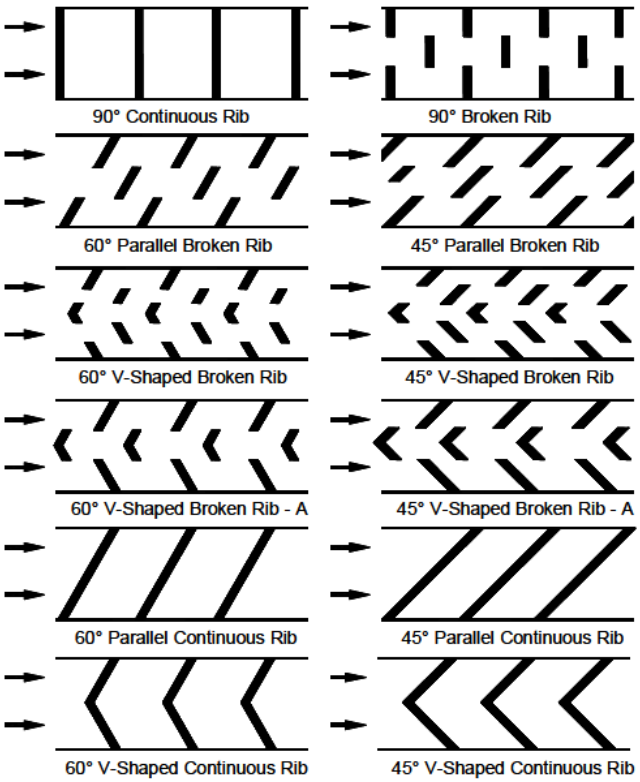


Figure 2.6: Various high performance rib turbulators [21]

2.2.2 External Cooling

External cooling techniques aim to create a thin, cold and protective air layer in order to protect the component from the hot combustion gases.

Film Cooling is based on introducing a secondary fluid at one or more discrete locations along a surface exposed to a high-temperature environment to protect that surface not only in the immediate region of injection but also in the downstream region. Figure 2.7 reportes a schematic representation of the film cooling concept. An extensive analysis of film cooling can be found in [39].

Transpiration Cooling represents the ideal evolution of film cooling where instead of discharging coolant through discrete holes, it utilizes a porous material to transpire a continuous and uniform protective layer. Thermal efficiency is maximized and coolant consumption is drastically reduced.

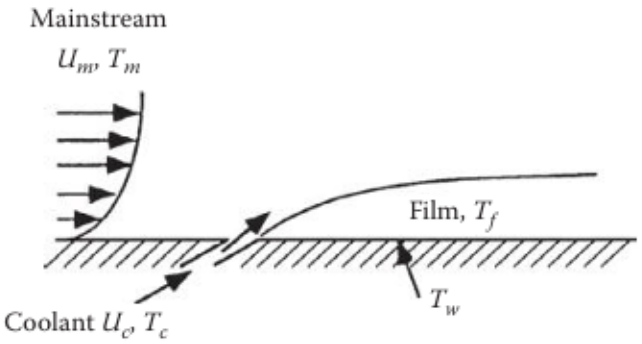


Figure 2.7: Schematic of film-cooling concept

2.2.3 Thermal Barrier Coating

TBCs act as an insulating shield, reducing heat propagation through the material [75]. TBCs play a significant role of protecting parts of gas turbine, internal combustion engine and other systems which operating at high temperatures. Normally TBCs are one or more layered coatings that involve a bond coat and a ceramic top coat. The bond coat gives assurance against oxidation by shaping a layer of defensive oxide between the bond coat and top coat called as thermally grown oxide (TGO), whereas top coat provides thermal protection to the super alloy. Yttria-Stabilized Zirconia (YSZ) is heavily favoured for top coat, as its thermal expansion coefficient is close to super composite materials and it exhibits low thermal conductivity at elevated temperatures.

For safer operation, the turbine blades in modern engines use nickel-based superalloys at metal temperatures well below 1400 K. Using TBCs allow for a 110 K to 170 K higher TIT, thereby enhancing turbine efficiency. Two main deposition techniques are conventionally used to apply Thermal Barrier Coatings:

- *Air Plasma Spray (APS)*: characterized by a lamellar (or splat-like) microstructure with high porosity, which results in a low thermal conductivity.

- *Electron Beam Physical Vapor Deposition (EBPVD)*: characterized by a columnar microstructure, which provides high strain tolerance despite its denser nature and relatively higher thermal conductivity.

The performance of TBC is related to the technique employed and to the coating thickness [42]. The utilization of TBCs, alongside the internal cooling, give significant increments in the workability of the engines at higher temperatures. Continuous research and investigation in thermal barrier materials is conducted by evaluating and analyzing their high-temperature behaviour and various failure modes. Vagge and Ghogare [75] summarize the state of the art of materials employed for TBCs.

2.3 Additive Manufacturing

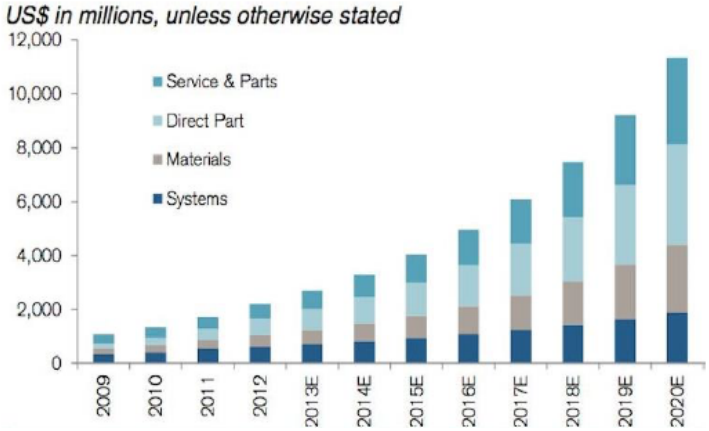


Figure 2.8: Global AM market trend [58]

Additive Manufacturing (AM) is an advanced manufacturing technique that builds parts by tracing their cross-section, layer by layer. This technology offers distinct advantages over conventional manufacturing techniques, most notably, the ability to create intricate geometries without the need for dedicated tooling. The manufacturing cost does not increase with rising geometric complexity. According to the ASTM standard [38], this manufacturing method is defined as follows:

"A process of joining materials to make objects from 3D model data, usually layer upon layer, as opposed to subtractive manufacturing methods" [58].

Figure 2.8 shows the rapid growth of the AM market over recent years. Beginning as a rapid prototyping tool, AM has matured into a comprehensive manufacturing solution, embracing a wide range of materials, such as polymers, metals, ceramics, and composites [76].

There are significant limitations regarding the mechanical strength of AM parts. The particle fusion process results in microstructures and porosities that are difficult to

predict and have a significant impact on the mechanical properties of the part. Despite the limitations, AM could be advantageous for static components subjected to high temperatures, such as combustor liners or high-pressure turbine vanes within gas turbine engines. To become a widely recognized manufacturing standard, AM must overcome some technical challenges. One of the primary challenges is the printing velocity, which, despite significant improvements, remains slow for mass production applications, limiting its feasibility to prototyping and small-scale manufacturing. The material limitation is slowly becoming less demanding since the range of materials suitable for 3D printing is expanding. Furthermore, the resolution and surface finish of printed objects require extensive post-processing to meet industry standards, adding time and cost to the manufacturing process.

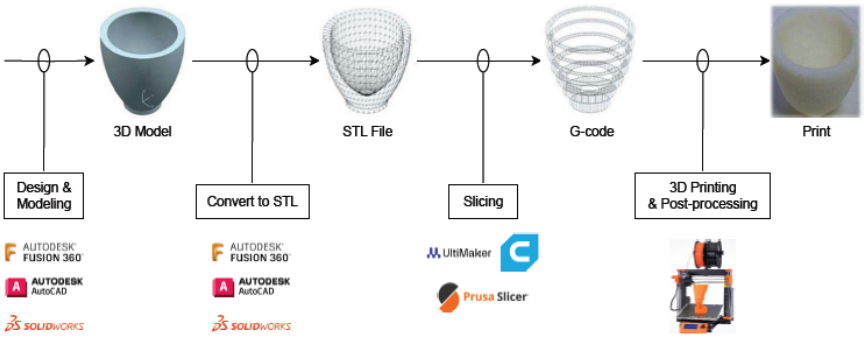


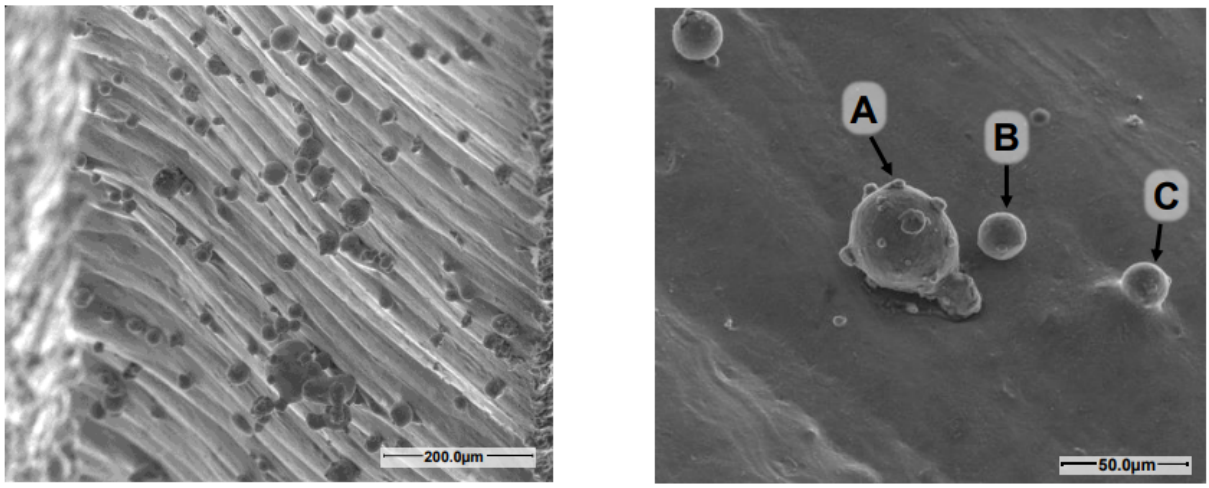
Figure 2.9: Overall workflow of the additive manufacturing process [76]

Figure 2.9 displays a schematic representation of the steps typically incolved during the AM process, regardless of the specific technique employed. These steps are described below:

- *CAD Design & Modelling*: utilizing CAD software, designers and engineers can craft detailed and complex models of the final object. During its creation, the CAD model must account for several factors, such as the specific printing material, the inherent constraints of the 3D printing technology, and the part orientation, all of which significantly affect the quality of the final output.
- *STL Conversion*: the 3D CAD model is then exported as a *Standard Tessellation Language* (STL) file. The STL files can be considered the bridge between digital design and physical realization. This process involves transforming a 3D design into a format that 3D printers can interpret. The STL format simplifies the model by breaking down its surface into a series of triangles. Each triangle is described by the coordinates of its vertices and the direction of its normal. The resolution of an STL file depends on the size of the triangles. Smaller triangles result in higher resolution, producing more detailed prints, but at the cost of increasing the file size.
- *Slicing*: the STL file is converted into thin and horizontal layers by using specific software. G-code is generated during this stage; this meticulous programming

language for Computer Numerical Control (CNC) machinery provides comprehensive instructions for the printer's movements.

- *3D Printing & Post-Processing*: following the machine setup detailed in [76], the fabrication begins as the printer's nozzle or energy source follows the G-code toolpaths. The choice of material is crucial and is selected based on the object's intended use. Once printed, components undergo post-processing to achieve the required physical and aesthetic properties. Surface finishing techniques include sanding, polishing, or chemical bathing.



(a) Low magnification view

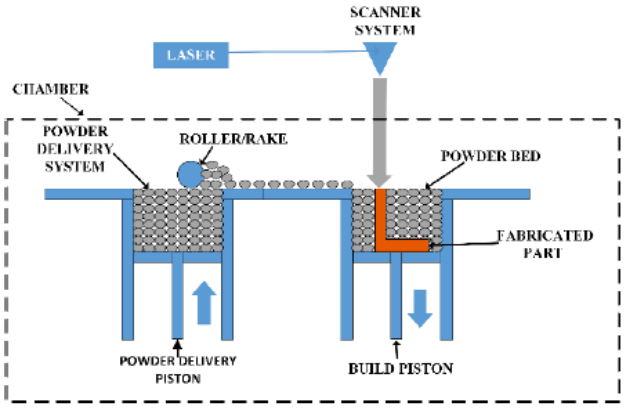
(b) High magnification view

Figure 2.10: Angled SEM micrographs of an Inconel coupon detailing roughness features [50]

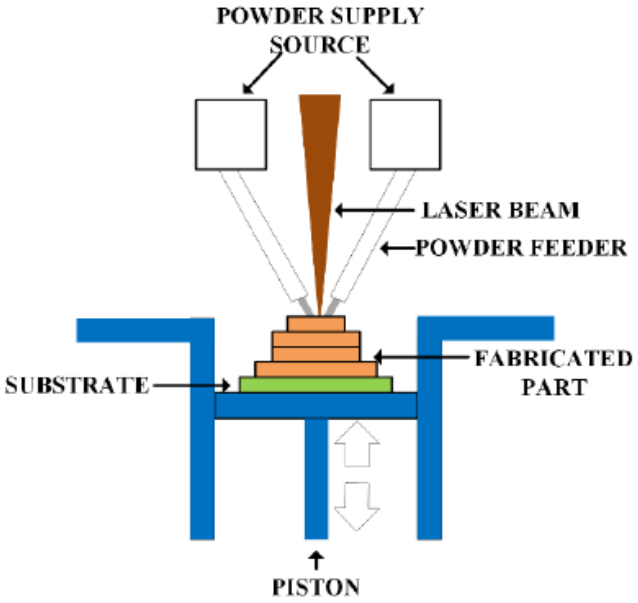
Figure 2.10 displays the typical SR features originating during the AM process. Spherical elements are commonly observed in different sizes, usually generating merged structures, as reported in Figure 2.10(b). The large SR might be a problem for metal parts production, as stated by Zhou [76]. It is this specific aspect of AM that is studied in this experimental work. Since the SR of small AM channels can enhance heat transfer, predicting its impact on associated pressure losses has gained considerable research interest.

Since the general AM methodology has been introduced, a brief overview regarding the most well-established techniques is given. Gebisa and Lemu [58] reported a classification based on the build volume. Moreover, they proposed a categorization based on the metallic material used, which is outlined below:

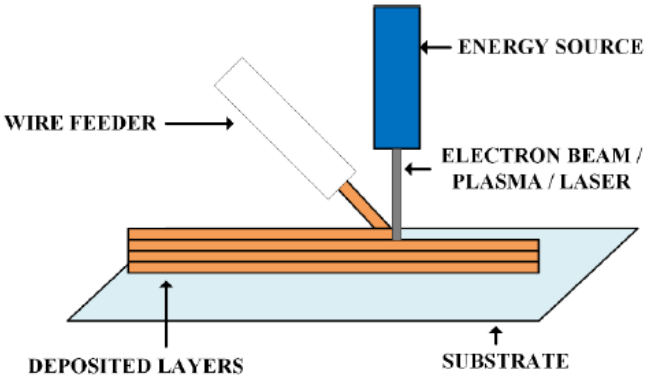
1. *Powder Bed AM techniques*: the metal powder is solidified, layer by layer. Once one layer of a powder from the powder bed is melted by an energy source, such as a laser beam, the deposited layer solidifies by fusing together powder particles. The build piston then moves down one step so the next layer of metal powder is supplied by the powder delivery piston that moves upward and then the powder



(a) Illustration of Powder Bed AM technique



(b) Illustration of Powder Feed AM technique



(c) Illustration of Wire Feed AM technique

Figure 2.11: Metallic AM techniques classification based on the form of metallic materials employed [58]

is spread by the roller or rake. Then this powder layer is solidified by the laser. Some techniques that employ this system are *Electron Beam Melting* (EBM), *Direct Metal Laser Sintering* (DMLS), *Selective Laser Melting* (SLM) and many more.

2. *Powder Feed AM techniques*: the metal powder from the powder supply source is ejected through the powder feeder into the substrate. Once the first layer of powder is melted by the laser beam and solidified, the next layer of powder is spread through the powder feeder, and this process is repeated until the part is completed. *Direct Metal Deposition* (DMD) belongs to this category.
3. *Wire Feed AM techniques*: wire feed AM techniques build parts from metallic wires in a layer-by-layer fashion. The wire is fed through the wire feeder to the substrate, where it is melted by an electron beam or plasma.

It should be noted that AM techniques that do not employ metallic materials are not mentioned in this specific classification. However, a comprehensive review across all material classes is provided by Zhou et al. [76]. Their work offers detailed discussions on *Vat Polymerization*, *Material Jetting* (MJ), *Selective Laser Sintering* (SLS), and other manufacturing methods.

The future of AM lies in material innovation and integration with conventional manufacturing techniques. AM continues to redefine manufacturing boundaries, steering industrial production toward a scalable, on-demand, and fully customized paradigm.

2.4 Roughness Parameters

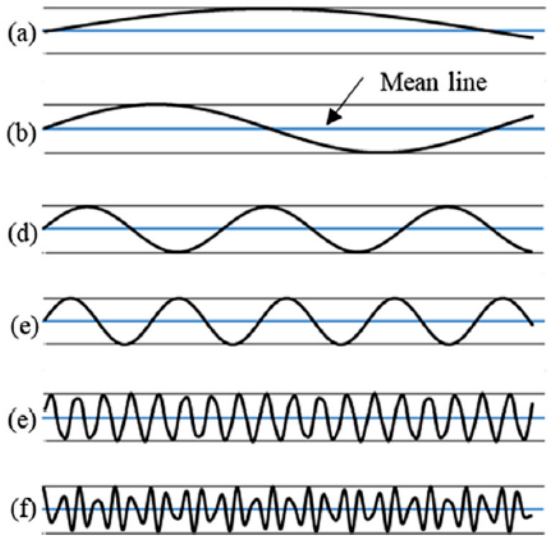


Figure 2.12: Surfaces with different wavelengths but the same amplitude [87]

During every manufacturing process no surface can be considered perfectly smooth, especially in AM process. Generally, the surface texture comprises a series of geo-

metrical irregularities that are randomly or uniformly extended over a smooth surface [32]. The spatial frequency of these irregularities defines the components of the surface texture, as shown in Figure 2.12 Geometrical features with a high frequency are considered *roughness*, while irregularities with a medium frequency are referred to as *waviness*. Finally, those characterized by a low frequency are known as *surface form* which is no longer considered as surface texture. Napoli et al. [31] introduced the *effective slope* to distinguish between roughness and waviness [70]. Yuan and Piomelli, together with Forooghi, proposed a classification based on the critical values of the effective slope to distinguish these configurations [45, 51].

Several texture parameters characterize the surface roughness, and they might differ in shape, frequency, and dimension. For this reason, it is necessary to establish precise definitions to define these surface characteristics. Technical reviews and industrial standards are used as a reference for SR parameters evaluation [70, 85, 87]. A single parameter cannot fully characterize the coupled fluid-dynamic and thermal performance. Consequently, a multi-parametric approach becomes indispensable.

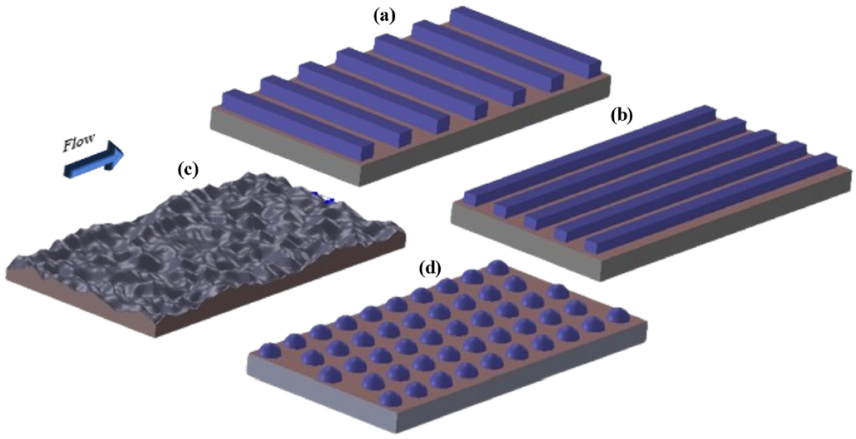


Figure 2.13: Examples of 2D and 3D roughness elements

The flow characteristics over rough surfaces should be expressed in terms of statistical surface properties in order to be compatible with the stochastic nature of irregular roughness distributions. As mentioned, the effectiveness of surface roughness in achieving substantial heat transfer improvement has yet to be verified alongside the resulting pressure losses and increase in drag. Roughness involves topographical features ranging from a few micrometers to a few millimeters [70]. As shown in Figure 2.13, SR can be divided into two groups:

- 2D roughness: this roughness refers to surfaces with a linear profile, varying in only one direction, such as spanwise or streamwise ribs and grooves with different cross-sections [64, 67].
- 3D roughness: this roughness refers to surfaces with a real height map consisting of regualar or irregualr roughness elements systematically or randomly dis-

tributed. These 3D features usually occur as a consequence of manufacturing processes or due to erosion, deposition corrosion [69].

Following this primary qualitative classification, the SR properties can be categorized more precisely and rigorously:

- *Roughness Height Parameters*: the primary characteristic of roughness is its height, which is often considered the most dominant parameter. Using height parameters alone oversimplify the complex nature of surface texture.
- *Roughness Density Parameters*: they represent the available area exposed to the flow. They can be considered as a representation of the surface density.
- *Roughness Spectral Parameters*: they quantify the frequency composition of the surface profile.

2.4.1 Roughness Heigh Parameters

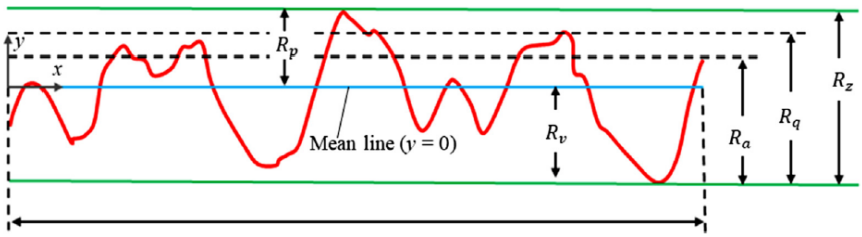


Figure 2.14: Surface Roughness height profile

A surface parameter can be calculated either along a linear sampling profile or on a sampling area. The parameters defined over the profile sampling length, also known as R-parameters, are widely used and more common, while those identified based on the sampling area, known as S-parameters, provide more comprehensive insights. The typical process to compute these height parameters involves using a heightmap to characterize the surface based on the vertical deviations of the roughness profile from a reference line or plane. Considering $z(x,y)$ as the surface elevation relative to the $z = 0$ level, the heightmap can be seen as:

$$z(x,y) = \bar{z} + z'(x,y)$$

where $\bar{z}$ is the mean height, while $z'(x,y)$ is the local deviation from the mean. The boundaries along the x and y directions are l_x and l_y, respectively. Further details regarding all the roughness height parameters can be found in Gadelmawla et al. work [24]. Only the most relevant parameters for this experimental work, evaluated over both a sampling line and a sampling area, are presented below to ensure a rigorous analysis.

2.4.1.1 Arithmetic Mean Roughness

The *arithmetic average height* parameter is defined as the average absolute deviation of roughness irregularities from the mean line over one sampling line (area). It is an easy parameter to define and measure, which gives a first indication of surface elevation.

$$R_a = \frac{1}{l_x} \int_0^{l_x} |z'(x,y)|\, dx$$

$$S_a = \frac{1}{l_x l_y} \int_0^{l_x} \int_0^{l_y} |z'(x,y)|\, dxdy$$

2.4.1.2 Root Mean Square Roughness

The *root mean square* represents the standard deviation of the distribution of surface heights and it is widely employed due to its sensitive to large deviations from the mean value.

$$R_q = \sqrt{\frac{1}{l_x} \int_0^{l_x} (z'(x,y))^2\, dx}$$

$$S_q = \sqrt{\frac{1}{l_x l_y} \int_0^{l_x} \int_0^{l_y} (z'(x,y))^2\, dxdy}$$

2.4.1.3 N-Points Height

This SR parameter defines the maximum peak-to-valley height, expressed as $S_t = S_p + S_v$ (or R_t for linear profiles), where S_p and S_v represent the maximum peak height and the maximum valley depth within the evaluation area, respectively. Because S_t is highly sensitive to local anomalies and can vary significantly between different sampling areas, an N-point average peak-to-valley height is often used, expressed as:

$$R_z = \sum_{i=1}^{N} R_{ti} = \sum_{i=1}^{N} (R_{pi} + R_{vi})$$

$$S_z = \sum_{i=1}^{N} S_{ti} = \sum_{i=1}^{N} (S_{pi} + S_{vi})$$

where $N = 5$ (ISO standar) or $N = 10$ (DIN) is typically employed. This parameter is more sensitive to occasional high peaks or deep valleys, such as those that occurs during AM processes.

2.4.2 Roughness Density Parameters

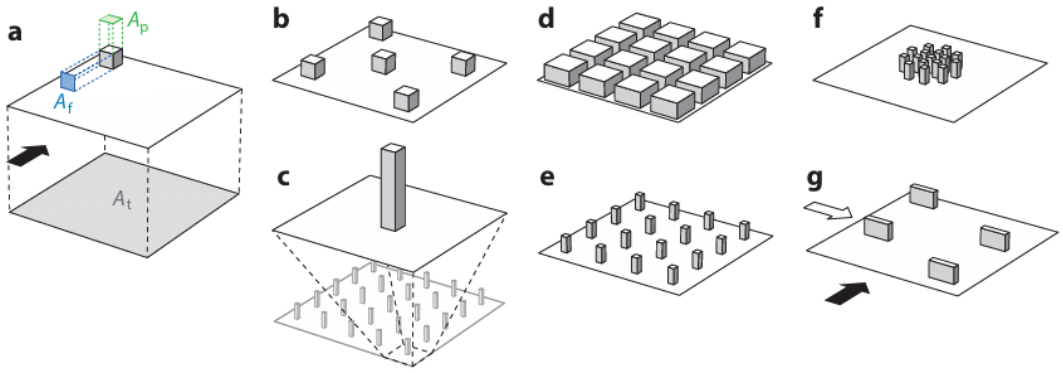


Figure 2.15: Surface sketches to illustrate frontal solidity and plan solidity [85]

The use of density parameters, combined with the heigh parameters, can help to better understand and correlate heat transfer and fluid-dynamic over rough models for several topographical surfaces. The spatial distribution can be identified by the *frontal solidity* λ_f, *effective slope* ES, and *roughness density* Λ_s.

2.4.2.1 Frontal Solidity

The frontal solidity λ_f quantifies the available area exposed to pressure drag and provides a measure of density. The roughness density, specifically the frontal solidity λ_f, controls the flow impingement mechanism on the windward surface [23]. Using Figure 2.15 as a reference, the frontal solidity can be defined as the ratio of the projected frontal area A_f to the total plan area A_t:

$$\lambda_f = \frac{A_f}{A_t}$$

Very sparsely packed or isolated roughness elements, as well as very densely packed ones, both tend toward hydraulically smooth conditions. In the former case, large expanses of smooth surface exist between elements, whereas in the latter, individual elements are sheltered from the flow due to their close proximity to neighbors. Between these two extreme regimes, there is typically a broad range ($0.1 < \lambda_f < 0.3$) where the drag coefficient reaches its maximum [85]. Similar to friction drag, the heat transfer performance exhibits a significant enhancement within this same range of $0.1 < \lambda_f < 0.3$. Conversely, for $\lambda_f \geq 0.3$, a pronounced sheltering effect occurs. However this parameter alone is insufficient to fully characterize the flow. Indeed, while at very-low λ_f the surface drag behaves as a smooth wall because the roughness exposure to the flow is minimal, at high densities the elements become tightly spaced and shelter each other, establishing a distinct skimming flow regime.

2.4.2.2 Effective Slope

The effective slope can be defined as the mean absolute gradient of a rough surface along the streamwise or spanwise directions. This measure is equivalent to twice the frontal solidity $ES = 2\lambda_f$. The value of the effective slope along the flow direction is of particular interest for the characterization of flow over rough walls. A low ES indicates rough elements are either sparsely packed or short wavelenght steep roughness. The former is known as k-type roughness, while the latter is referred to as d-type roughness, which are further discussed by Kadivar et al. [87]. The effective slope, with respect to the streamwise and spanwise directions respectively, is defined as follows:

$$ES_x = \frac{1}{l_x l_y} \int_0^{l_x} \int_0^{l_y} \left| \frac{\partial z'(x,y)}{\partial x} \right| dxdy$$

$$ES_y = \frac{1}{l_x l_y} \int_0^{l_x} \int_0^{l_y} \left| \frac{\partial z'(x,y)}{\partial y} \right| dxdy$$

2.4.2.3 Roughness Density

The roughness density Λ_s is defined as:

$$\Lambda_s = \frac{1}{\lambda_f} \frac{A_f}{A_w}$$

where A_w is the total windward wetted surface area. The local value of Λ_s is linked with the local roughness angle defined below:

$$\alpha_z = \arctan\left(\frac{\partial z'(x,y)}{\partial x} \right)$$

2.4.3 Roughness Spectral Parameters

The density parameters combined with the spectral parameters can enhance the prediction of drag.

2.4.3.1 Plan Solidity

The plan solidity λ_p is defined as the ratio of the roughness plan area A_p to the total plan area A_t, as displayed in Figure 2.15. This parameter provides a quantitative measure of both the roughness element density and the overall surface morphology.

$$\lambda_p = \frac{A_p}{A_t}$$

A high plan solidity suggests densely packed arrangements while cases with low plan solidity imply sparsely packed arrangements. Usually the ratio λ_f/λ_p can be used to capture information about the aspect ratio of the rough element. However, this cannot be true when the elements are clustered.

2.4.3.2 Skewness

The skewness parameter measures the asymmetry of the surface elevation distribution. Positively skewed surfaces are typically spiky surfaces with many peaks, while negatively skewed surfaces are characterized by a pitted morphology with many valleys, as illustrated in Figure 2.16.

$$S_{sk} = \frac{1}{S_q^3} \int_0^{l_x} \int_0^{l_y} (z'(x,y))^3 \, dxdy$$

2.4.3.3 Kurtosis

The kurtosis is a measure of flatness of roughness, defined as:

$$S_{ku} = \frac{1}{S_q^4} \int_0^{l_x} \int_0^{l_y} (z'(x,y))^4 \, dxdy$$

When $S_{ku} < 3$ the distribution is referred to as platykurtik, indicating the absence of extreme features such as high peaks and low valleys on the surface. Whem $S_{ku} > 3$ the distribution is known as leptokurtic, indicating a prevalence of extreme features.

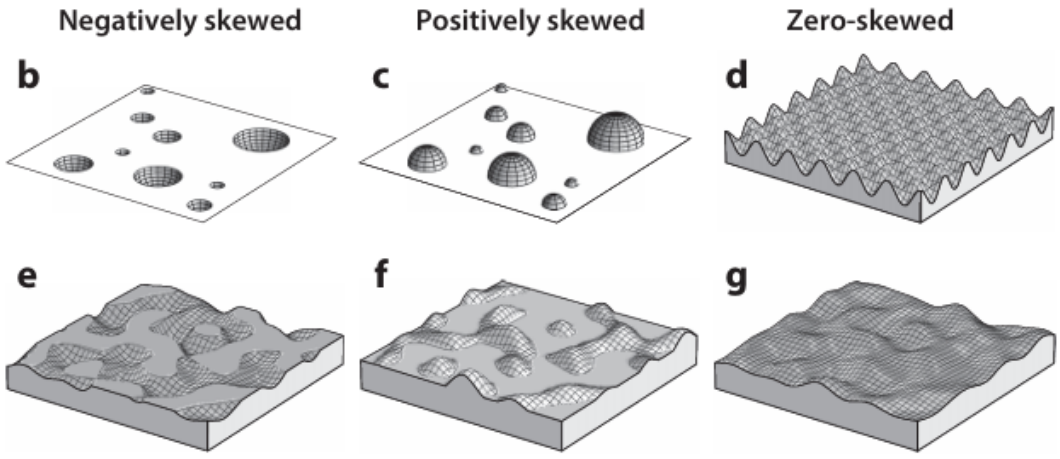


Figure 2.16: Surface sketches to illustrate spectral parameters [85]

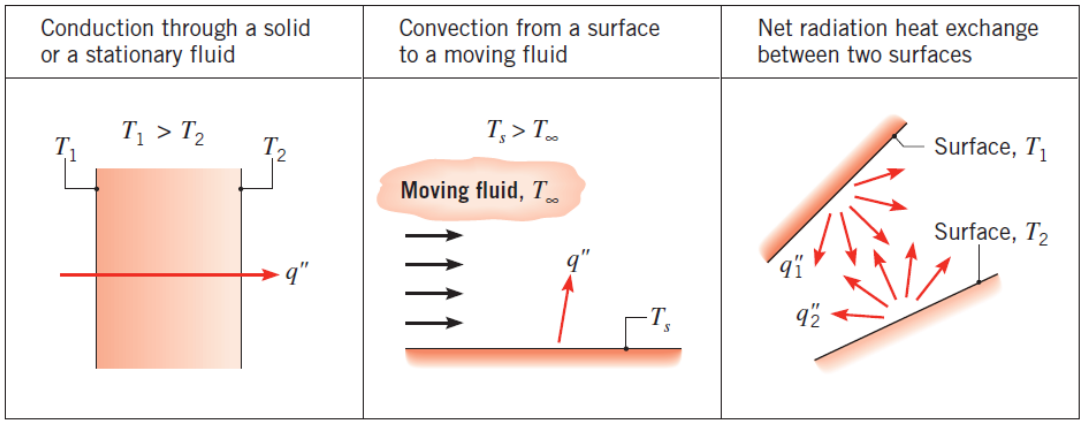


Figure 2.17: Conduction, convection, and radiation heat transfer modes [37]

2.5 Fundamentals of Heat Transfer

Energy can be transferred by work or heat between a system and its surroundings. In this section, a general overview of the fundamental heat transfer mechanisms is provided. Heat transfer can be defined as the thermal energy which is in transit due to a spatial temperature difference [37]. Heat transfer can be quantified in terms of appropriate rate equations. These equations may be used to compute the amount of energy being transferred per unit time. Figure 2.17 shows the three heat transfer modes that will be introduced here and described in the following sections:

1. *Conduction* occurs when a temperature gradient exists in a stationary medium, which may be a solid or a fluid.

2. *Convection* happens between a surface and a moving fluid when they are at different temperatures.

3. *Radiation* involves all surfaces at a non-zero absolute temperature which continuously emit energy via electromagnetic waves through the mechanism of thermal radiation.

2.5.1 Conduction

Conduction is the transport of energy in a medium due to a temperature gradient and the physical mechanism is one of random atomic or molecular activity, as displayed in Figure 2.18. This heat mechanism can be seen as the transfer of energy from the more energetic to the less energetic particles of a substance due to interactions between the particles themselves. In the presence of a temperature gradient, energy transfer by conduction must then occur in the direction of decreasing temperature. The governing rate equation is known as *Fourier's law*. By adopting the one-dimensional assumption, Fourier's law can be expressed using the temperature distribution $T(x)$:

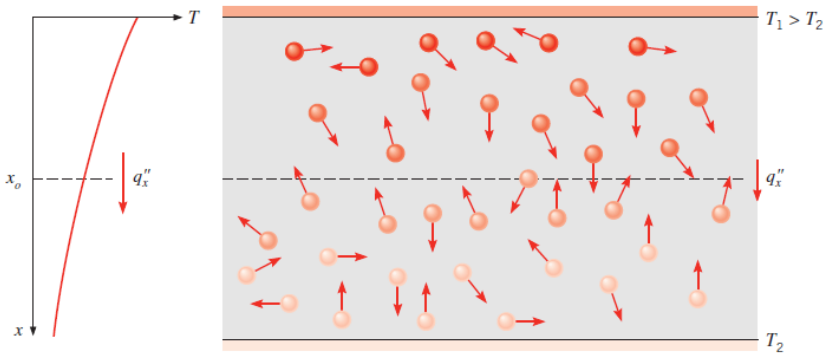


Figure 2.18: Schematic representation of heat conduction through a wall

$$\dot{q}_x = -k\frac{dT}{dx}$$

The parameter k represents the *thermal conductivity* (W/(m · K)) and is an intrinsic transport property of the material. The heat flux $\dot{q}_x$ (W/m^2), which in Figure 2.18 is expressed as q''_x, represents the heat transfer rate in the x-direction per unit area perpendicular to the direction of transfer, and it is directly proportional to the local temperature gradient, dT/dx. The negative sign dictattes that thermal energy is inherently transferred in the direction of decreasing temperature.

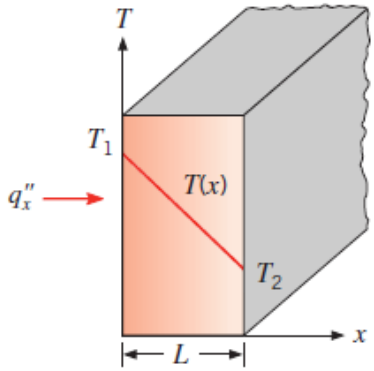


Figure 2.19: One-dimensional assumption for conduction heat transfer

Under the steady state conditions and with a linear temperature distribution through the wall, as reported in Figure 2.19, the heat flux can be written as:

$$\dot{q}_x = -k\frac{dT}{dx} = -k\frac{T_2 - T_1}{L}$$

Then the *heat rate* by conduction q_x through a plane wall of area A is then the product of the flux and the area $q_x = \dot{q}_x \cdot A$. However, Fourier's law is applicable to transient,

multidimensional conduction in complex geometries. Further details regarding the generalized conduction rate equation and thermal conductivity can be found in Incropera [37].

2.5.2 Convection

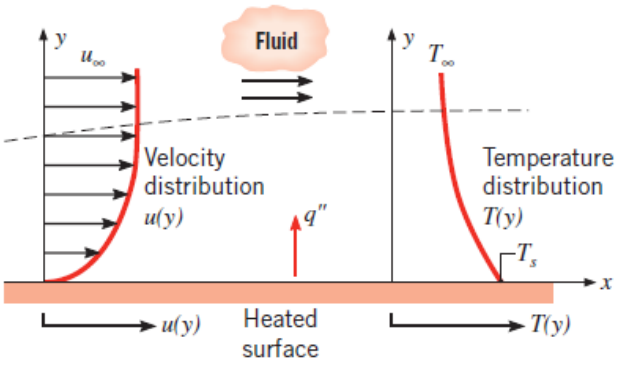


Figure 2.20: Schematic representation of convection mode

Convection consists of two physical mechanisms. In addition to energy transfer due to random molecular motion, energy is also transferred by the bulk motion of the fluid. This fluid motion, in the presence of a temperature gradient, contributes to heat transfer. Due to fluid-surface interactions, a region develops within the fluid where the velocity ranges from zero at the surface to the free-stream velocity u_∞, as shown in Figure 2.20 . This thin region is known as *velocity boundary layer*. The contribution due to random molecular motion is relevant near the surface where the fluid velocity is low. The contribution due to bulk fluid motion originates from the fact that the boundary layer grows as the flow progresses in the x-direction. Moreover, if the surface and flow temperatures differ, there will be a region of the fluid through which the temperature varies from T_s at $y = 0$ to T_∞ in the outer flow. This region is called *thermal boundary layer* and may be smaller, larger, or the same size as that through which the velocity varies. In any case, when $T_s > T_\infty$ convection heat transfer will occur from surface to the outer flow.

Convection heat transfer may be classified according to the nature of the flow. Figure 2.21 shows a typical overview of these transport modes. When the flow is caused by an external agent, the mechanism is classified as *forced convection*, while the *free convection* occurs when the flow is induced by buoyancy forces, which are due to density differences caused by temperature variations in the fluid. However, there are two other phenomena within the convection mode related more to latent heat exchange. This is usually associated with a phase change, such as in the *boiling* and *condensation*. Regardless of the nature of the convection heat transfer processes, the governing rate equation is expressed as follows:

$$\dot{q} = h(T_s - T_\infty)$$

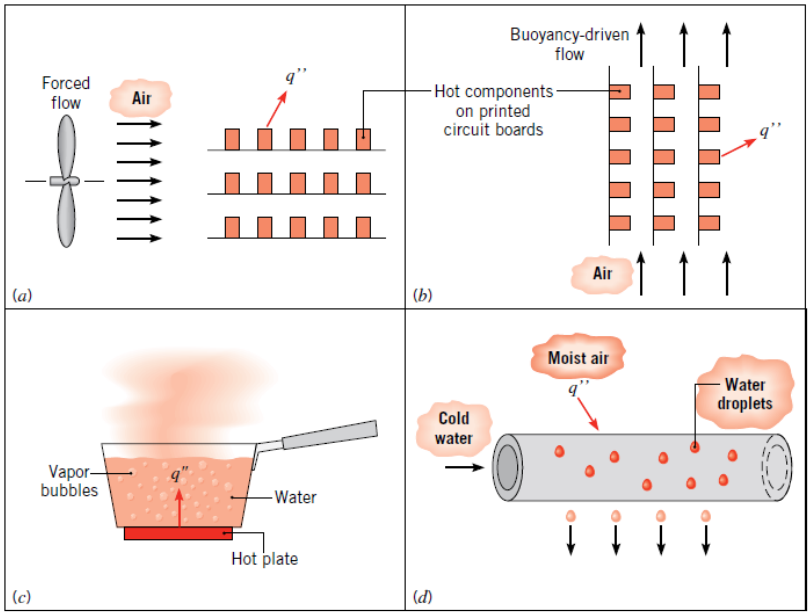


Figure 2.21: Convection classification [37]

where the convective heat flux $\dot{q}$ is proportional to the difference between the surface and fluid temperatures, T_s and T_∞ respectively. T_s and T_w are often used interchangeably to denote the wall temperature. This equation is also known as *Newton's law of cooling*. The parameter h is the convection heat transfer coefficient (HTC), the key objective of this thesis work. Any study of convection ultimately reduces to a study of the means by which the HTC may be determined.

2.5.3 Radiation

Thermal radiation is energy emitted by matter that is at a nonzero temperature. The emission may be attributed to changes in the electron configurations of the constituent atoms or molecules. The energy of the radiation field is transported by electromagnetic waves. Moreover,radiation transport does not require the presence of a material medium. Radiation that is emitted by the surface originates from the thermal energy of matter bounded by the surface and the rate at which energy is released per unit area is referred to as the *surface emissive power E*. The *Stefan-Boltzman law* establishes an upper limit to the maximum emissive power:

$$E_b = \sigma T_s^4$$

where T_s is the absolute temperature of the surface and σ is the Stefan Boltzman constant ($\sigma = 5.670 \times 10^{-8} \mathrm{W/(m^2 \cdot K^4)}$). This type of surface is also known as ideal radiator or blackbody. Further details will be provided within the IRT section. However, the real emissive power is less than that of a blackbody at the same T_s and is given by:

$$E = \epsilon \sigma T_s^4$$

where ϵ is a radiative property of the surface called *emissivity*. This property provides a measure of how efficiently a surface emits energy relative to a blackbody. It depends on surface material and finish. When a medium is between two exchanging bodies, the transferred energy may be partially or completely absorbed, reflected, or may even pass through the medium without attenuation. This is the working principle of an IR scanner, which can detect the temperature of a body without touching it.

2.6 Infrared Thermography IRT

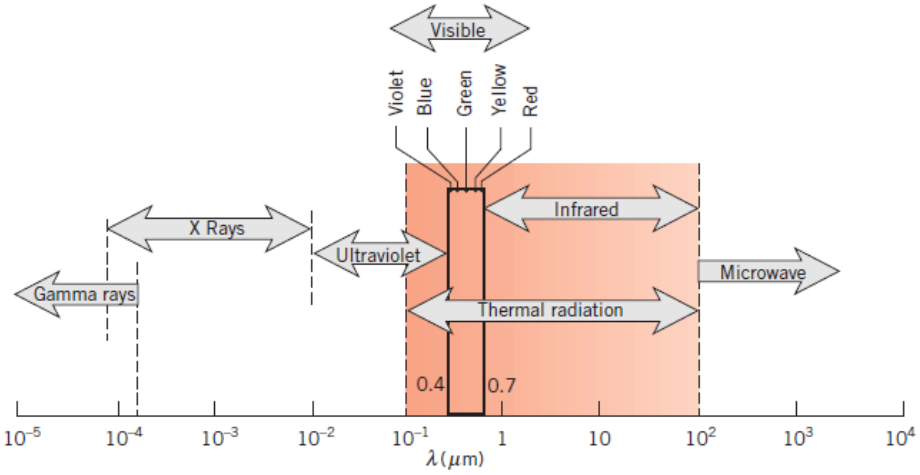


Figure 2.22: Spectrum of electromagnetic radiation [37]

Infrared Thermography is a non-destructive testing technique which has advanced rapidly in recent years [66]. IRT provides a two-dimensional, non-contact approach for surface temperature measurements. The infrared scanning radiometer detects the electromagnetic energy radiated within a specific IR spectral band by an object and converts it into an electronic video signal. The amount of thermal radiation that is absorbed or emitted, as well as its subsequent propagation, depends not only on the intrinsic nature of the material and its surface finish, but also on the local thermodynamic state and the specific wavelength of the considered electromagnetic wave. The wavelength λ is related to the wave frequency f by the speed of light within the medium, c, according to the following relation:

$$\lambda = \frac{c}{f}$$

The speed of propagation in a generic medium is related to the propagation speed in vacuum c_0 by this relationship:

$$c = \frac{c_0}{n}$$

where n is the dimensionless *index of refraction* of the medium. The frequency f is the only quantity which depends only on the source of the electromagnetic wave. The entire electromagnetic spectrum is divided into a number of wavelength intervals, called *spectral bands*, displayed in Figure 2.22. The *thermal radiation*, which is the relevant portion of the spectrum for heat transfer experiments, includes part of the ultraviolet and all of the visible and IR bands. In particular, when a body is at ambient temperature most of the energy is radiated in the infrared spectral band. Moreover, the IR band can be divided into four sub-bands reported in Table 2.1. Most of the currently used IR camera temperature detectors are sensitive in either the MIR or LIR wavelength. Using detectors within this wavelength range is beneficial due to the high atmospheric transmissivity (or low absorption) within these windows. Therefore, coating a body with a thin layer of opaque material (such as a dull enamel) can completely modify its surface radiation properties. This approach is highly effective when using an IR camera to measure surface temperatures, particularly for high-reflectivity materials.

Infrared Bands	λ [μm]
Near Infrared (NIR)	0.76 – 3
Middle Infrared (MIR)	3 – 6
Long Infrared (LIR)	6 – 15
Far Infrared (FIR)	15 – 1000

Table 2.1: Infrared spectral bands

2.6.1 Black Body Radiation

For a given body surface temperature, the energy emitted by radiation per unit surface area and unit time depends on the material nature of the body and its surface characteristics. The concept of *blackbody* is used to formulate fundamental radiative laws before extending them to real surfaces. A blackbody has the property of being a perfect emitter and absorber of radiation. It is able to absorb all the incident radiation, regardless of wavelength and direction. For a fixed temperature and wavelength, it emits the maximum possible amount of radiation. Moreover, a blackbody emits radiation uniformly in all possible directions.

There are several approaches used to idealized blackbody behaviour. Since the visible band is a very small part of the complete spectrum, in general a black-colored surface is usually a good approximation of an ideal blackbody. Moreover, a good physical approximation of a blackbody is an isothermal cavity featuring a very small opening. Any incident thermal radiation entering the cavity through this aperture undergoes multiple internal reflections before potentially escaping back through the same opening.

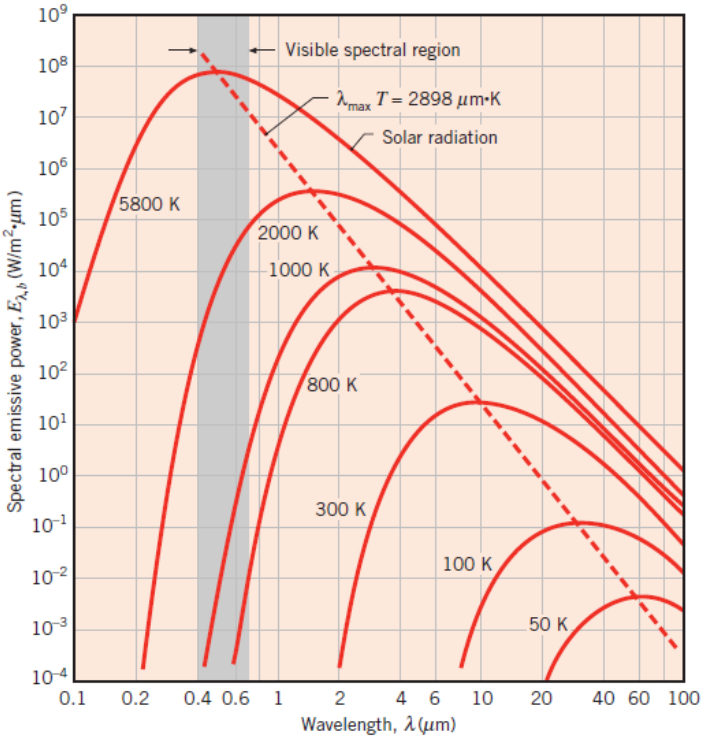


Figure 2.23: Spectral blackbody emissive power

During each consecutive reflection, a fraction of the radiative energy is absorbed by the internal cavity walls. Consequently, the net radiation that eventually leaves through the small hole is effectively negligible, making the aperture behave as a near-perfect blackbody absorber. The fundamental relation that governs the radiative energy flux per unit wavelength, referred to as the *blackbody spectral hemispherical emissive power*, $E_{b\lambda}$ (W/m^3), emitted by a blackbody into a vacuum, is defined by *Planck's law*:

$$E_{b\lambda}(\lambda, T) = \frac{C_1}{\lambda^5 \left(e^{\frac{C_2}{\lambda T}} - 1 \right)}$$

where T is the absolute body temperature and C_1 and C_2 are the first and the second radiation constants. The emitted radiation is a continuous function of the wavelength and each isothermal curve tends to zero for both very large and very small values of λ, having a maximum at some intermediate wavelength. Upon an increase in the blackbody's temperature, the position of this maximum shifts towards smaller wavelengths (dashed straight line). The *Wien's displacement law* enables to find the maximum wavelength λ_{max} at which a black body emits its maximum spectral emissive power as a function of its temperature.

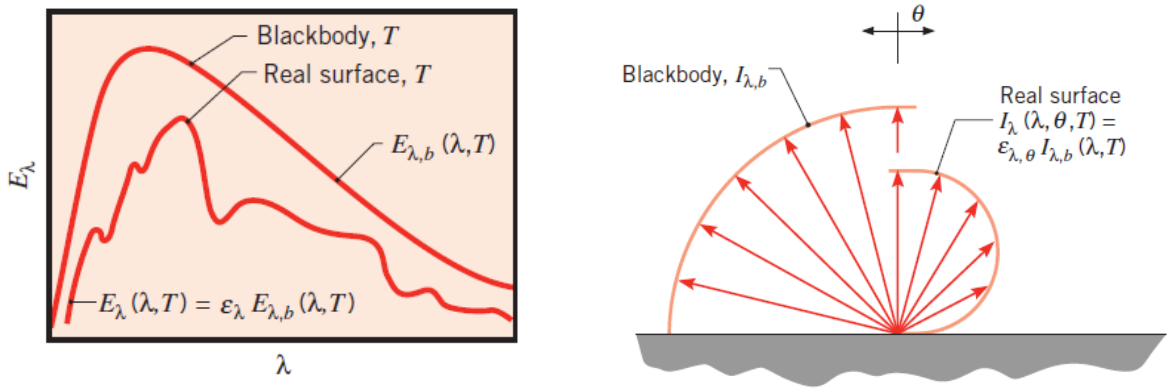
$$\lambda_{\max} T = 2898\ \mu\text{m} \cdot \text{K}$$

Since IR camera detectors capture only a limited band of the whole electromagnetic spectrum, for IR experiments it is more convenient to perform a definite integral of Planck's law in order to find the energy flux sensed by the detector in a certain band $\lambda_1 - \lambda_2$:

$$E_{b,\lambda_1-\lambda_2}(T) = \int_{\lambda_1}^{\lambda_2} E_{b\lambda}(\lambda, T)\, d\lambda$$

2.6.2 Realy Body Radiation

Figure 2.24(a) displays a comparison between the blackbody emitted radiation and the real surface emission. The latter is clearly smaller than the blackbody emission, while both compared at the same body temperature. The blackbody curve represents an upper limit for real bodies. Figure 2.24(b) shows a preferred propagation direction for real bodies instead of diffuse distribution of the blackbody.



(a) Spectral distribution.

(b) Directional distribution.

Figure 2.24: Comparison between a blackbody and a real surface: (a) spectral distribution and (b) directional distribution

The emissivity that accounts for emission over all wavelengths and in all directions is the total, hemispherical emissivity, which is the ratio of the total emissive power of a real surface to the total emissive power of a blackbody at the same temperature.

$$\epsilon(T) = \frac{E(T)}{E_b(T)}$$

When irradiation impinges upon a real slab of finite thickness, only a fraction of this energy is absorbed. The remaining fraction may be partially reflected and partially transmitted across the slab medium. Denoting the absorbed fraction of irradiation as α_r, the reflected fraction as ρ_r, and the transmitted fraction as τ_r, the principle of conservation of energy requires that:

$$\alpha_r + \rho_r + \tau_r = 1$$

where α_r, ρ_r and τ_r are respectively called *absorptivity*, *reflectivity* and *transmittivity* coefficients of the body. They are bounded between zero and unity. They depend on the nature of the slab material, its surface finish, its thermodynamic state as well as on the wavelength and direction of the impinging radiation. More details about real radiation can be found in [29, 37, 94].

2.6.3 IR Scanner

Figure 2.25 shows a schematic configuration of an infrared scanning radiometer. Thermal radiation, entering the scanner, is collected by an optical system and sent into a temperature detector which is sensitive within the selected IR band. The electrical signal generated by the detector is acquired by a video frame grabber and is processed by a dedicated electronic board in order to obtain a temperature map of the scanned scene.

The optical system of an IR scanner is similar to that of a standard camera working in the visible band except for the material that constitutes the optical components that must be transparent in the considered infrared band. The material used for the optical system differs for the specific IR band. In the MIR band are typically used silicon, sapphire, calcium fluoride, magnesium fluoride, whereas for the LIR band germanium, zinc selenide, zinc sulphide, sodium chloride, potassium bromide.

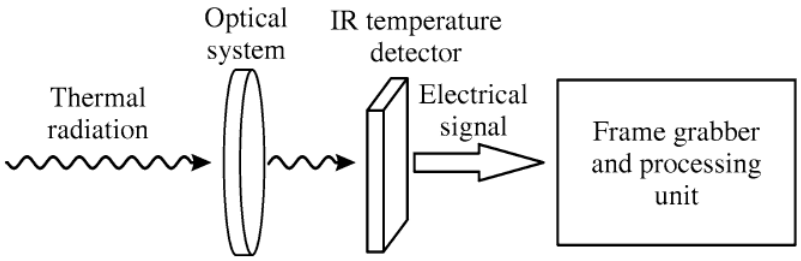


Figure 2.25: Infrared scanning radiometer scheme [94]

In the early infrared cameras a scanning mechanism was used to direct the radiation of different points of the field of view (FOV) onto a single temperature detector. Radiation, coming from the target object is first collected by the lens and subsequently deflected by a quite complex mirror system. Actually, the field of view is scanned in different ways, along the horizontal or vertical directions. The temperature detector of an infrared scanner is the core device that enables the conversion of the impinging radiation into an electrical signal. IR temperature detectors are normally divided into two broad classes which differ according their working principles:

1. *Thermal Detectors*: the incident radiation changes one of the electrical properties of the detector due to a temperature modification of the detector itself.

2. *Photon Detectors*: also known as quantum or photonic detectors, the photons of the incident radiation directly interact with the electrons of the detector material.

For the thermal detectors the electrical response is linked with the absorbed energy, whereas for the photon detectors it is proportional to the number of absorbed photons by the detector material. Modern IR cameras employ a two-dimensional array of pixels, known as *focal plane array* (FPA) detector. One of the technical challenges for these devices is to ensure uniform performance across all sensing elements. The number of pixels defines the spatial resolution performance of the scanner.

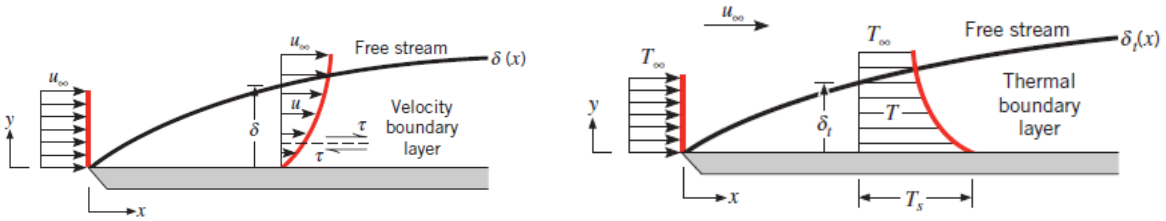
The acquisition frequency is an important parameter for the measurement of the convective heat transfer coefficients during transient phenomena and is mainly connected with the detector response time. It should be noted that the acquisition frequency is limited by the minimum integration time needed by a detector pixel to accurately measure the temperature of the target object. Many IR detectors are integrated directly with their cooling systems (typically thermoelectric or Stirling coolers) to ensure optimal performance. Further details on spatial resolution, acquisition frequency, and calibration, are discussed by Carlomagno and Astarita [94].

2.7 Boundary Layer Theory

Boundary layers are essential for understanding convective heat and mass transfer. Their velocity and thermal profiles are governed by momentum and thermal diffusivity, which relate to each other through the *Prandtl number*:

$$Pr = \frac{\nu}{\alpha}$$

with ν and α representing the kinematic viscosity and thermal diffusivity respectively. If $Pr > 1$ it means that momentum boundary layer thickness is greater than thermal boundary layer thickness. Instead, when $Pr < 1$ it happens the exact oppposite.



(a) Momentum boundary layer (b) Thermal boundary layer

Figure 2.26: Development of velocity and temperature boundary layer

As shown in Figure 2.26 for flow over a flat surface, fluid particles contacting the wall experience a velocity reduction relative to the upstream flow, ultimately reaching a velocity of zero at the solid boundary. These particles then act to retard the motion

of particles in the adjoint fluid layer until at a distance $y = \delta$ from the wall, where these effects become negligible. This retardation is due to the *shear stress* τ acting parallel to the fluid velocity. With increasing distance y from the surface, the x velocity component of the fluid, u, must then increase until it approaches the free stream value u_∞.

The quantity δ is named *momentum boundary layer thickness* and it is defined as the value of y for which $u = 0.99u_\infty$. The fluid flow is characterized by two distinct regions, a thin fluid layer in which velocity gradients and shear stresses are significant, and a region outside the boundary layer in which velocity gradients and shear stresses are negligible.

The thermal boundary layer must develop if the fluid free stream and surface temperatures are different. If this happens a temperature gradient between the surface and the free stream is developed. The region of the fluid in which these temperature gradients exist is the *thermal boundary layer thickness* δ_t, which is defined as the value of y for which the ratio $(T_w - T)/(T_w - T_\infty) = 0.99$, where,$T_w$ is the wall temperature and T_∞ is the free stream temperature.

2.7.1 Laminar and Turbulent Flows

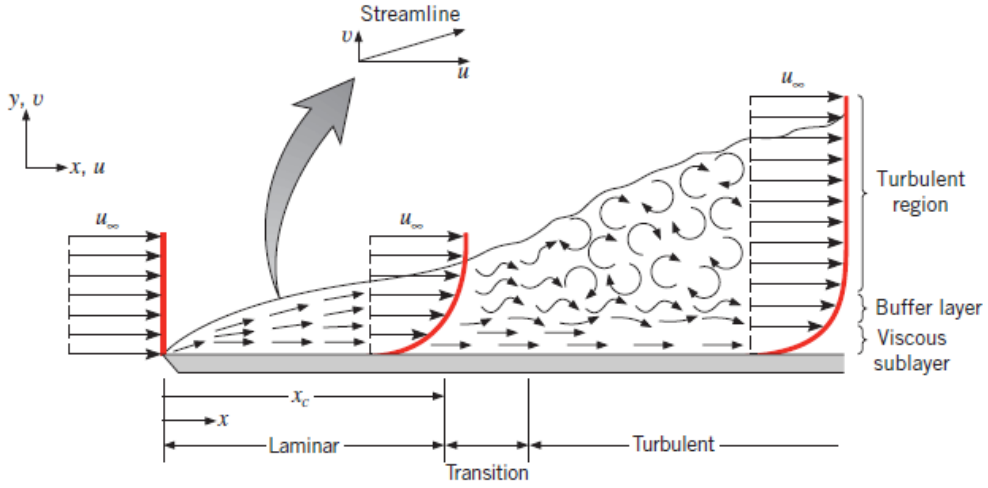


Figure 2.27: Boundary layer transition

Figure 2.27 displays the boundary layer development over a flat surface. Several differences exist between laminar and turbulent regimes, with the laminar regime anticipates the turbulent one.

In the laminar boundary layer, the fluid flow is highly ordered until a transition zone is reached. Conversely, in the turbulent region the flow is highly chaotic, characterized by random three-dimensional motion, mixing effects, and fluid-dynamic structures called *velocity streaks*, which promote fluid motion from low-velocity to high-velocity regions [26].

As a result of the interactions that lead to chaotic flow conditions, velocity and pressure fluctuations occur at any point within the turbulent boundary layer. To analyze turbulent flows, physical quantities are split into a time-averaged and a fluctuating component using the *Reynolds decomposition*. The time-averaged component is calculated over a time scale larger than that of the turbulent fluctuations. Specifically, the velocity components, pressure (p), and temperature (T) can be decomposed as follows:

$$\begin{aligned} u &= \bar{u} + u' \\ v &= \bar{v} + v' \qquad p = \bar{p} + p' \qquad \theta = \bar{\theta} + \theta' \\ w &= \bar{w} + w' \end{aligned}$$

The transition from laminar to turbulent flow is triggered by the interaction of unsteady flow structures or small boundary layer disturbances. These disturbances may originate from fluctuations in the free stream, or they may be induced by surface roughness. The Reynolds number is the parameter that governs this transition:

$$Re_D = \frac{u_\infty D}{\nu}$$

where D represents the characteristic length. It is also possible to evaluate the critical location for this transition. Every flow exhibits a specific critical Reynolds number which may depend on various factors. Further details are discussed by Incropera [37].

2.7.2 Momentum Boundary Layer

The momentum boundary layer originates due to fluid viscosity. At the wall the velocity is equal to zero, respecting the no-slip condition; it increases its value along the normal coordinate until the free stream velocity value is reached. The velocity boundary layer thickness, and shear stress all depend on the streamwise coordinate. The shear stress τ is proportional to the velocity gradient and can be expressed using *Newton's law of viscosity*:

$$\tau = \mu \frac{\partial u}{\partial y}$$

where μ represents the dynamic viscosity of the fluid. When the shear stress is evaluated at the wall ($y = 0$), it is referred to as the *wall shear stress*:

$$\tau_w = \mu \left. \frac{\partial u}{\partial y} \right|_{y=0}$$

For turbulent boundary layer analysis, the *friction velocity* u_τ is introduced as a characteristic velocity scale for the near-wall turbulence. It is used to non-dimensionalize the velocity profile and define the *wall variables*:

$$u_\tau = \sqrt{\frac{\tau_w}{\rho}}$$

The velocity profile across the normal coordinate can be rewritten using:

$$u^+ = \frac{u}{u_\tau} \qquad y^+ = \frac{y u_\tau}{\nu}$$

From the asymptotic matching analysis the boundary layer over smooth and rough walls consists of two overlapping regions, which differ for the different lengthscale adopted to express the velocity profile [70].

1. *Inner Layer*: this region is attached to the wall and it is affected by viscosity and local flow parameters.
2. *Outer Layer*: located above the inner layer, this region is characterized by large-scale turbulent motions where viscous effects become negligible.

The outer region typically occupies 80–90% of the boundary layer thickness, whereas the inner layer spans the remaining 10–20% of δ. The inner region can be further subdivided into three distinct zones:

- *Viscous Sublayer*: this region is closest to the wall, where the velocity profile is approximately linear due to the dominance of viscous effects.
- *Buffer Layer*: a transitional zone characterized by the peak production of turbulent kinetic energy. In this region, the turbulent shear stress is of the same order of magnitude as the viscous one. No analytical relations are avaialable to describe the velocity profile within this layer.
- *Logarithmic Layer*: the velocity profile follows a logarithmic law, and the flow is governed by turbulent shear stresses.

Wall shear stress becomes less important far from the wall, where the turbulent stress tends to be significant. The velocity profile across the inner layer is reported below:

$$u^+ = \begin{cases} y^+ & 0 < y^+ \leq 5 \\ \dfrac{1}{\kappa}\ln(y^+) + C & 30 \leq y^+ \leq 500\text{-}1000 \end{cases}$$

where $\kappa = 0.41$ represents the von Karman constant and $C = 5.1$ is the Coles constant. The outer layer is unaffected by the direct influence of the wall. This region is also

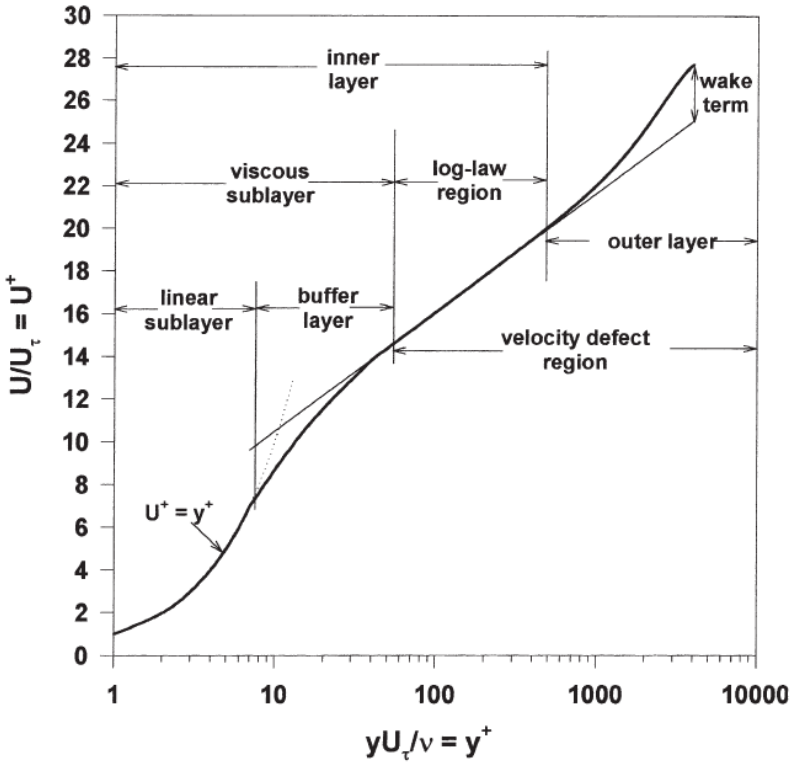


Figure 2.28: Normalized velocity profile u^+ vs y^+ [25]

named the defect layer due to the velocity defect with respect to the free stream. In order to cover this region Coles modified the log-law velocity profile by introducing the *wake function* [70].

$$u^+ = \frac{1}{\kappa}\ln(y^+) + C + \frac{\Pi(x)}{\kappa}\omega\left(\frac{y}{\delta}\right).$$

2.7.3 Thermal Boundary Layer

Temperature boundary layer originates when the bulk temperature of the flow and the wall temperature are different. The turbulent thermal boundary layer borrows various similarities to the corresponding momentum boundary layer. The differences are due to the variety of the different boundary conditions as well as the influence of the molecular and turbulent Prandtl numbers. The evaluation of the turbulent heat flux, defined as $\rho c_p \overline{v'T'}$ plays a key role for the determination of the heat flux, alongside with the molecular heat flux $\rho c_p \alpha \frac{\partial T}{\partial y}$. v' and T' represent the fluctuating components of velocity and temperature due to turbulent fluctuations. According to Prandtl's mixing length model, $\overline{v'T'} = \epsilon_H \frac{\partial T}{\partial y}$, where ϵ_H is the *thermal eddy diffusivity*. The total wall heat flux can be written as [27]:

$$\dot{q} = -\rho c_p(\alpha + \epsilon_H)\frac{\partial T}{\partial y}$$

In the same way, the wall shear stress can be written as:

$$\tau_w = \rho(\nu + \epsilon_M)\frac{\partial u}{\partial y}$$

where ϵ_M is the *momentum eddy diffusivity*. Prandtl's mixing length theory suggests $\epsilon_M = k\nu y^+$. The *turbulent Prandtl number* is introduced:

$$Pr_t = \frac{\epsilon_M}{\epsilon_H}$$

The molecular Prandtl number Pr is a constant value determined by the fluid properties; however, Pr_t is a property specific to turbulent conditions which is characterised as the resistance to heat transfer in turbulent flows. In the boundary layer, it can be assumed that the streamwise temperature gradient is negligible and temperature is a function of wall-normal coordinate alone. To study the turbulent thermal boundary layer, as it was done for the momentum boundary layer, the temperature profile $T(y)$ is expressed using the *friction temperature* Θ_τ defined as:

$$\Theta_\tau = \frac{\dot{q}}{\rho c_p u_\tau}$$

To express the normalized temperature profile the wall variable are used:

$$\Theta^+ = \frac{T(y) - T_w}{T_\tau} \qquad y^+ = \frac{y u_\tau}{\nu}$$

The thermal boundary layer can be divided into two regions based on the relative magnitude of ky^+/Pr_t:

1. *Conduction Sublayer CSL*: this region is attached to the wall, where molecular conduction dominates heat transfer and temperature gradient is mostly influenced by the fluid's thermal diffusivity rather than turbulent mixing.
2. *Logarithmic Layer*: above the CSL the flow can be described by a logarithmic law, where convective transport by turbulent eddies dominates the heat transport.

The temperature profile within the CSL can be expressed as [78]:

$$\Theta^+ = Pry^+, \qquad y^+ < \delta_\theta^+$$

where δ_θ^+ is the CSL's thickness, which depends on Pr. As Pr increases, the thermal diffusivity decreases relative to the viscous effect, resulting in slower conduction compared to convective transport due to momentum, hence reducing CSL's thickness. Pirozzoli [78] proposed this formulation for δ_θ^+:

$$\delta_\theta^+ \approx \begin{cases} \dfrac{1}{\kappa_\theta Pr} & Pr \ll 1 \\ \left(\dfrac{A_\theta^2}{\kappa_\theta Pr}\right)^{\frac{1}{3}} & Pr \gg 1 \end{cases}$$

where $A_\theta = 19.2$ and $k_\theta = k/Pr_t \approx 0.459$. The temperature profile within the log-layer is written as, for $y^+ > \delta_\theta^+$:

$$\Theta^+ = \frac{1}{\kappa_\theta} \ln y^+ + \beta(Pr)$$

$\beta(Pr)$ is a Prandtl number-dependent offset function, playing a crucial role in estimating the heat transfer coefficient. This function can be determined by:

$$\beta(Pr) = \lim_{y^+ \to \infty} \left[\Theta^+(y^+) - \frac{1}{\kappa_\theta} \ln y^+ \right]$$

Kader and Yaglom [11] reviewed some of the proposed correlations for $\beta(Pr)$ and derived this relation, which represents one of the most robust frameworks:

$$\beta(Pr) = 12.5 Pr^{2/3} + 2.12 \ln Pr - 5.3$$

Later, Kader revisted this formulation as follows:

$$\beta(Pr) = \left(3.85 Pr^{1/3} - 1.3\right)^2 + 2.12 \ln Pr$$

Pirozzoli [78] using an integral solution approach, analytically derived:

$$\beta(Pr) = \frac{\sqrt{3}\pi A_\theta^{2/3}}{6\kappa_\theta^{1/3}} Pr^{2/3} + \frac{1}{\kappa_\theta} \ln Pr - \frac{1}{\kappa_\theta} \ln A_\theta$$

The lack of a precise correlation for $\beta(Pr)$ affects the vertical shift of the logarithmic layer, resulting in an uncertainty when plotting temperature profile across the thermal boundary layer.

Researcher	Roughness type	$k_s^+{}_{\text{Smooth}}$	$k_s^+{}_{\text{Rough}}$
Nikuradse	Uniform sand-grain	5	70
Ioselevich and Pilipenko	Sand-grain roughness	2.5	90
Ligrani and Moffat	Packed sphere bed	15	50
Langelandsvik et al.	Commercial steel pipes	1.4	18
Shockling et al.	Honed pipe	3.5	30
Schultz and Flack	Surface scratch	2.5	25
Lewkowicz and Musker	Ship-hull roughness	17	40
Cebeci and Bradshaw	Sand-grain roughness	2.25	90

Table 2.2: Values of roughness Reynolds number limits for different roughness types

2.7.4 Turbulent Flow over Rough Surface

The surface roughness alters the characteristics of turbulent flows. One of the most significant effects of wall roughness is increased drag. The boundary layers over smooth and rough walls possess quite different structures governed by different length scales in the inner layer, while the outer layer remains unaffected by the surface texture. Other effects include the modification of the near-wall boundary layer and turbulence generation.

When the surface roughness height is larger than the thickness of the viscous sublayer, a new scale must be adopted to express its effect on the flow field. The *sand-grain* roughness height is used for roughness characterization in rough wall flows. This approach was first pioneered by Nikuradse and Schlichting [3].

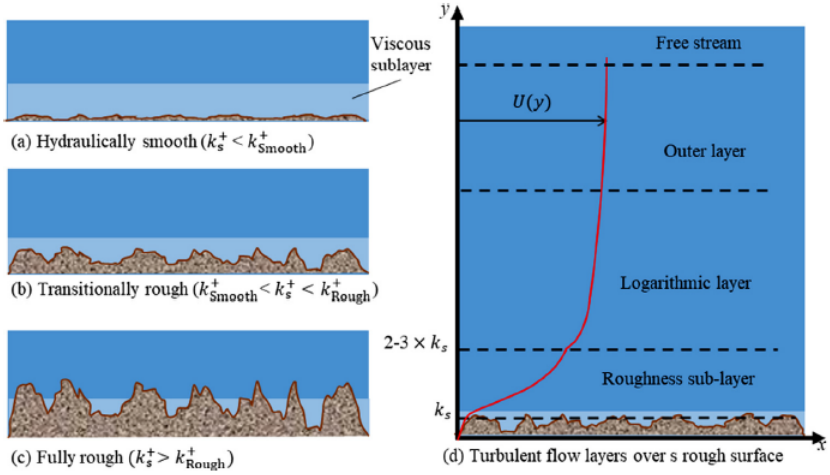


Figure 2.29: Turbulent rough flows regimes

This approach characterizes surface roughness using a single length scale. The sur-

face topology is modeled as a densely packed monolayer of uniform spheres, whose diameter defines the sand-grain roughness height, k. However, when the shape of roughness deviates from the sand-grain, a single parameter cannot describe the sand-grain roughness anymore. When the roughness differs from this configuartion other geometrical parameters should be considered to characterize the flow.

Colebrook and White [5] introduced an equivalent length scale, the *equivalent sand grain roughness* k_s. This length scale can be seen as an equivalent roughness height for irregular, and non-uniform rough surfaces that produce the same results as the uniform sand-grain of the Nikuradse for a fully rough flow regime. Since the roughness affects the flow, the law of the wall seen for smooth surface has to be modified using the *roughness Reynolds number* k_s^+ defined as:

$$k_s^+ = \frac{k_s u_\tau}{\nu}$$

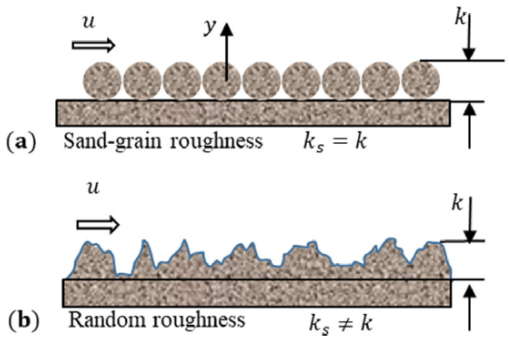


Figure 2.30: Equivalent sand-grain roughness

Corresponding to the three regions of the wall affected the turbulent boundary layer, the rough flow regimes can be classified into three main categories. Consider k^+_{smooth} and k^+_{rough} as two critical limits of the roughness Reynolds number, the three roughness regimes are defined :

- *Hydraulically Smooth Regime*: when $k_s^+ \leq k^+_{smooth}$ the roughness elements are entirely embedded in the viscous sublayer and skin friction and drag coefficients are not modified.
- *Transitionally Rough Regime*: when $k^+_{smooth} \leq k_s^+ \leq k^+_{rough}$ the influence of the surface roughness is complex. Both viscous and pressure forces influence the friction coefficient. The transitionally rough regime is associated with the reduced sublayer thickness.
- *Fully Rough Regime*: $k_s^+ \geq k^+_{rough}$ the rough elements protrude into the fully turbulent region shifting the logarithmic profile downwards. The viscous sublayer is entirely destroyed by the intense turbulent mixing caused by the roughness

elements. The friction drag significantly increases due to pressure forces on the roughness.

There are different values for the critical limits adopted to classify the three rough regimes in the literature and they are reported in Table 2.2. The variety of reported values for the onset of the transitionally rough and fully rough regimes for different roughness types indicates difficulty in defining universal scaling parameters applicable for all roughness regimes. Many empirical correlations are available in the literature to estimate k_s, as reviewed by Kadivar et al. [70].

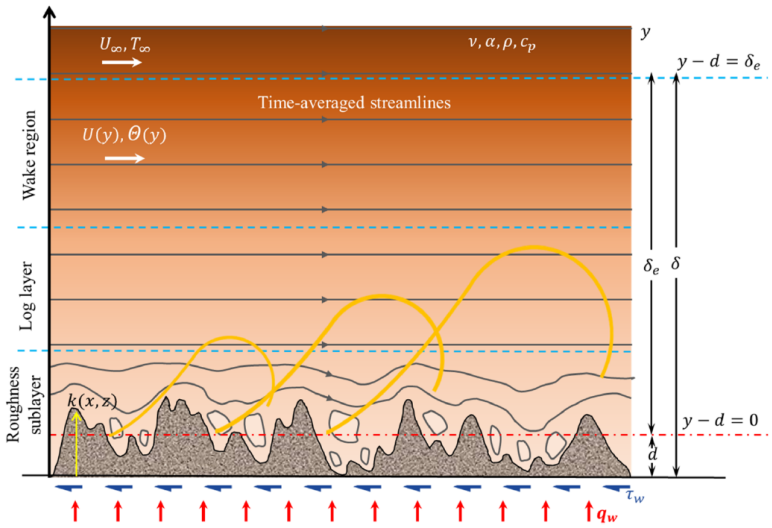


Figure 2.31: Schematic of rough-wall boundary layer problem

In order to analyze rough-wall flows, many studies focused on the extension of the smooth models for the velocity and the temperature profiles. The velocity and temperature profiles are consequently changed near the wall. The impact of surface roughness is reflected in a downward shift of the logarithmic mean velocity profile, known as roughness function ΔU^+ [87], as displayed in Figure 2.32. According to Clauser [7] the logarithmic velocity over roughness can be obtained by modifying the smooth-wall log-law:

$$u_R^+ = u_S^+ - \Delta U^+ = \frac{1}{\kappa} \ln(y-d)^+ + C - \Delta U^+$$

where $C \approx 5.5$ is the smooth wall intercept. The subscripts R and S refers to rough and smooth conditions. Hama [8] proposed another formulation of the roughness function:

$$\Delta U^+ = \frac{1}{\kappa} \ln k_s^+ + C - B$$

where B is the roughness constant, which takes a value of $B \approx 8.5$ in the fully rough

regime. Since the roughness function reflects the momentum deficit due to friction drag by the roughness, it can be written as:

$$\Delta U^+ = \sqrt{\frac{2}{C_{f,S}}} - \sqrt{\frac{2}{C_{f,R}}}$$

This equation is a straightforward method for determining roughness functions in experimental studies and where C_f represents the friction coefficient detailed in the following section.

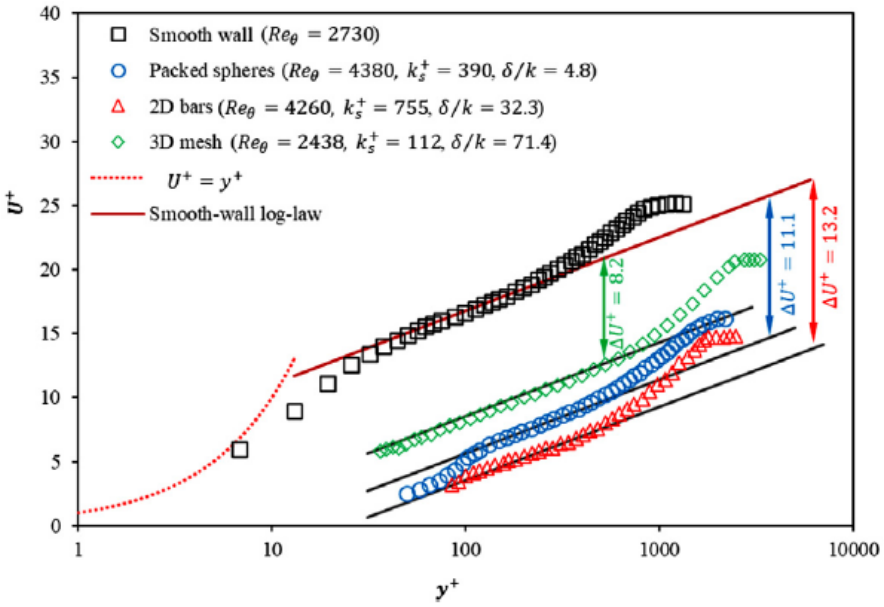


Figure 2.32: Mean velocity profiles of experimental turbulent flows over 2D bars and 3D mesh [33, 35]

2.8 Wall Bounded Turbulent Flows

The internal flow configuration represents a convenient geometry for heating and cooling fluids used in chemical processing, environmental control, and energy conversion technologies. When considering external flow, it is necessary to ask only whether the flow is laminar or turbulent. However, for an internal flow we must also be concerned with the existence of entrance and fully developed regions. Regarding internal flows, the vast majority of foundational studies have been carried out on circular pipes. However it is possible to adapt the results by using the *hydraulic diameter*:

$$D_h = \frac{4A}{P}$$

where A is the cross sectional area and P is the wetted perimeter of the channel. Considering a laminar flow entering a circular pipe, with a uniform velocity. The contact between the fluid and the wall produce viscous effects that make the development of the boundary layer possible. This development occurs at the expense of a shrinking inviscid flow region and concludes with boundary layer merger at the centerline. The entire cross section and the velocity profile no longer changes with increasing x. The flow is then said to be fully developed, and the distance from the entrance at which this condition is achieved is termed the *hydrodynamic entry length*, $x_{fd,h}$. The extension of the entry region depends on whether the flow is laminar or turbulent. The Reynolds number built based on the duct diameter is used to assess at which fluid-dynamic condition the transition from laminar to turbulent occurs. For circular pipes the critical Reynolds number $Re_D \approx 2300$. However, higher Reynolds are needed to achieve fully turbulent conditions usually around $Re_D \approx 10000$. For laminar flow the hydrodynamic entry length can be calculated as:

$$\left(\frac{x_{\mathrm{fd},h}}{D}\right)_{\mathrm{lam}} \approx 0.05\, Re_D$$

There is no satisfactory general expression for the entry length in turbulent flow. It is independent of Reynolds number and can be estimated as:

$$10 \leq \left(\frac{x_{\mathrm{fd},h}}{D}\right)_{\mathrm{turb}} \leq 60$$

It is usually assumed $(x/D) > 10$ for a fully developed turbulent flow.

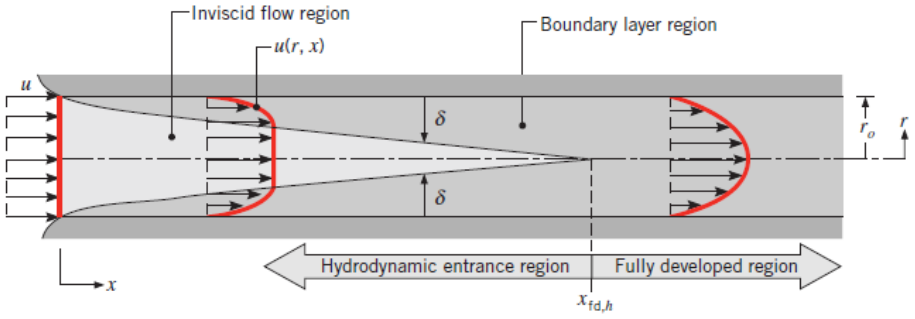


Figure 2.33: Hydrodynamic boundary layer development in a circular tube

Incropera et al. [37] developed a complete analytical formulation to determine the velocity profile within the circular duct, which is omitted here. The pressure drop needed to sustain the internal flow can be evaluated from the *Moody diagram*, shown in Figure 2.34, where the *Darcy friction factor* f_D is plotted:

$$f_D = -\frac{dp}{dx}\frac{2D}{\rho \bar{U}^2}$$

where $\frac{dp}{dx}$ represents the pressure gradient and $\bar{U}$ is the mean velocity inside the channel. This dimensionless quantity is different from the *friction coefficcient* C_f, sometimes referred to as the Fanning friction factor, which is defined as:

$$C_f \equiv \frac{\tau_w}{\rho \bar{U}^2/2} = \frac{f_D}{4}$$

After some algebraic manipulations, the friction factor for the laminar flow regime can be written as:

$$f_D = \frac{64}{Re}$$

For fully developed turbulent flow, the analysis is more complex and is based on experimental results. In addition, the friction factor is a function of both the Reynolds number and the tube surface texture. Measured friction factors covering a wide range of conditions have been correlated by Colebrook [5]:

$$\frac{1}{\sqrt{f_D}} = -2.0 \log \left[\frac{e/D}{3.7} + \frac{2.51}{Re_D \sqrt{f_D}} \right]$$

where e/D is the relative roughness. As a first approximation, the ratio between the roughness element height and the hydraulic diameter can be used. Pethukov [10] developed a correlation for smooth surfaces for a large range of Reynolds number:

$$f_D = (0.790 \ln Re_D - 1.64)^{-2} \qquad 3000 \leq Re_D \leq 5 \times 10^6$$

From the Moody chart, in the fully rough zone, the friction factor is constant. Increasing the relative roughness generates a higher friction factor.

When the fluid enters a duct with a uniform temperature, different from the wall temperature, convective heat transfer occurs. The choice of a uniform wall temperature or uniform heat flux boundary condition can drastically change the shape of the fully developed temperature profile. For a laminar flow, the thermal entry length can be expressed as:

$$\left(\frac{x_{\mathrm{fd},t}}{D} \right)_{\mathrm{lam}} \approx 0.05 \, Re_D \, Pr$$

For turbulent flow, conditions are weakly dependent of the Prandtl number, and to a first approximation, $x_{\mathrm{fd,t}}/D = 10$ can be assumed. The existence of convective heat transfer between the surface and the fluid dictates that the fluid temperature must continue to change with x. For the momentum boundary layer in the fully developed

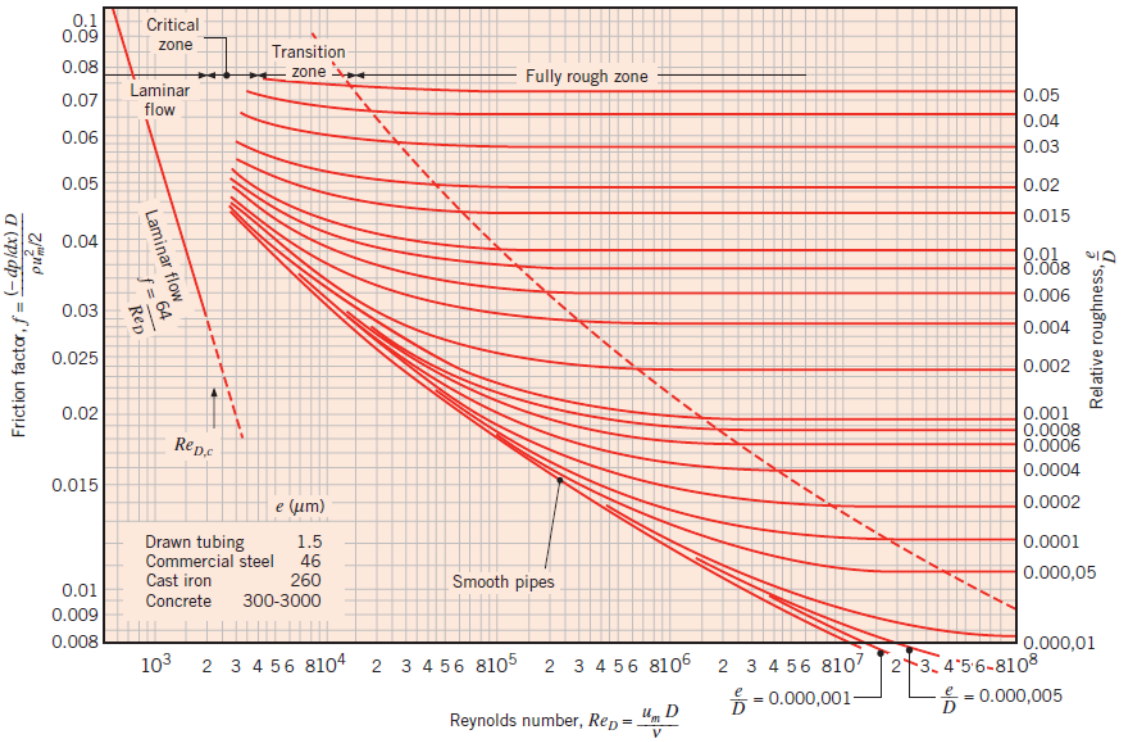


Figure 2.34: Moody Diagram

region, the velocity gradient satisfies $\frac{\partial u}{\partial x} = 0$. For the thermal one, this is not true anymore because the temperature changes at every radius along the streamwise direction of the pipe. Consequently, it might mistakenly appear that a thermally fully developed state can never be achieved. This apparent contradiction may be reconciled by working with a dimensionless form of the temperature introduced below:

$$\frac{T_w(x) - T(r,x)}{T_w(x) - T_m(x)}$$

The relative shape of the profile no longer changes and the flow is said to be thermally fully developed when the following condition is verified:

$$\frac{\partial}{\partial x}\left[\frac{T_w(x) - T(r,x)}{T_w(x) - T_m(x)}\right]_{\text{fd},t} = 0$$

where T_w is the surface temperature and T_m is the mean temperature inside the tube. By differentiating the previous relation with respect to the radial coordinate, it can be shown that, in the thermally fully developed region and for a flow with constant properties, the local convective heat transfer coefficient does not change. This condition is not true in the entrance region, where h varies with the axial direction x because the

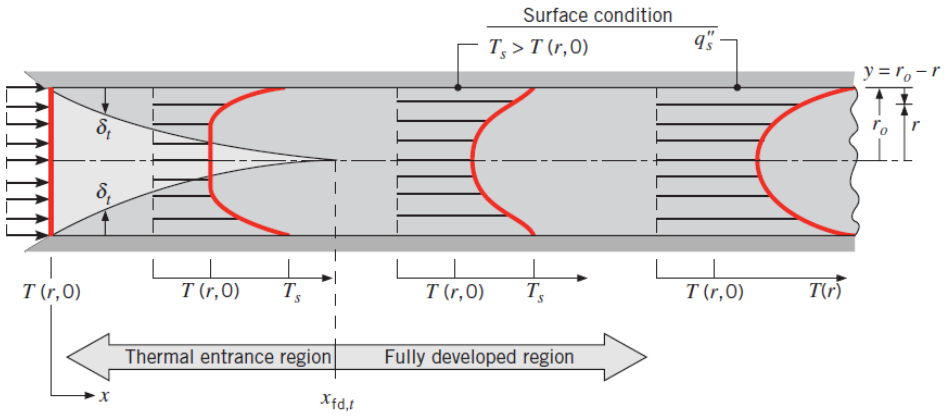


Figure 2.35: Thermal boundary layer development in a heated circular tube

thermal boundary layer is not yet fully developed. Figure 2.36 shows the behavior of h along the entrace and fully developed region.

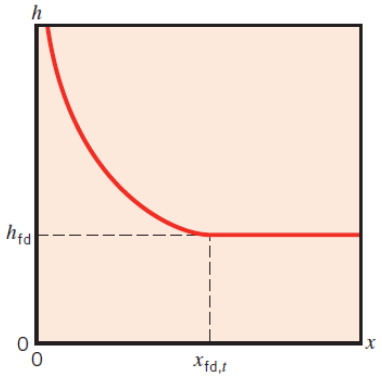


Figure 2.36: Axial variation of the convective heat transfer coefficient for flow in a tube

2.8.1 Heat Transfer Correlations

A brief overview of the most commonly used heat transfer correlations is presented for laminar and turbulent flows in both circular and non-circular ducts. Considering a laminar fully developed flow, with a constant heat flux boundary condition, after some manipulations reported in [37], the convective heat transfer coefficcient, hence the Nusselt number is constants and indipendent from the Reynolds and Prandt numbers. The same happens considering a costant wall temperature with a different value for the constant.

$$Nu = \begin{cases} 4.36 & \dot{q} = \text{const} \\ 3.66 & T_w = \text{const} \end{cases}$$

For a fully developed turbulent flow in a smooth circular pipe, the local Nusselt number can be estimated using the *Dittus–Boelter correlation* [22]:

$$Nu = 0.023\, Re^{4/5} Pr^{n} \qquad \begin{cases} 0.6 \leq Pr \leq 160 \\ Re_D \geq 10000 \\ L/D \geq 10 \end{cases}$$

where $n = 0.4$ for heating and $n = 0.3$ for cooling. This correlation was confirmed experimentally and it employed for small to moderate temperature differences, with all properties evaluated for mean temperature. For large property variations, Sieder and Tate [4] proposed:

$$Nu = 0.027\, Re_D^{4/5}\, Pr^{1/3} \left(\frac{\mu}{\mu_s} \right)^{0.14} \qquad \begin{cases} 0.6 \leq Pr \leq 16700 \\ Re_D \geq 10000 \\ L/D \geq 10 \end{cases}$$

where all properties except μ_s are evaluated at the bulk mean temperature. However the Dittus-Boelter and Sieder correlations are easily applied and are certainly satisfactory, errors as large as 25% may result from their use. Such errors may be reduced to less than 10% through the use of more recent, but generally more complex, correlations. One correlation, valid for smooth tubes over a large Reynolds number range including the transition region, is provided by Gnielinski [13]:

$$Nu = \frac{(f_D/8)(Re_D - 1000)\, Pr}{1 + 12.7\, (f_D/8)^{1/2} \left(Pr^{2/3} - 1 \right)} \qquad \begin{cases} 0.6 \leq Pr \leq 2000 \\ 3000 \leq Re_D \leq 5 \cdot 10^6 \end{cases}$$

where the friction factor is evaluated from the Moody diagram. If temperature differences are large, additional consideration must be given to variable-property effects and available options are reviewed by Kakac [17]. This correlation was developed for fully turbulent flow so it should be carefully adopted at low Reynolds number. Procedures for estimating the effect of wall roughness on convectibe heat transfer in fully developed turbulent flow are discussed by Bhatti and Shah [16]. Incropera et al. [37] reviewed heat transfer correlations for cross-sectional geometries different from the circular one.

Chapter 3

Research Methodology

This chapter presents the methodology employed for the SRHT rig, where the local heat transfer effects of the upscaled additively manufactured test objects were investigated. The first part is dedicated to explaining the main functions and the most important components of the experimental rig. This is then followed by a brief description of how the samples were designed and manufactured. Subsequently, the experimental data acquisition procedure is described, including the software employed for the analysis. Finally, the chapter concludes with an uncertainty analysis aimed at assessing the reliability of the conducted tests.

3.1 SRHT Rig

The SRHT rig was designed to assess the local heat transfer coefficient (HTC) distribution on the aforementioned AM test objects. The local HTC h is defined as:

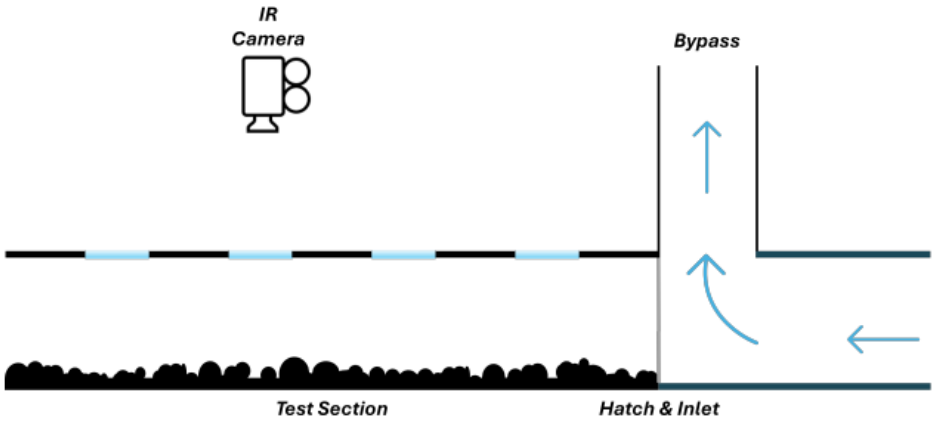
$$h = \frac{\dot{q}}{T_w - T_{bulk}}$$

where $\dot{q}$ is the surface heat flux while $T_w - T_{bulk}$ is the temperature difference between the wall and the bulk free stream temperature. Rather than considering the HTC values, the results of this experimental work are presented in terms of the dimensionless parameter named *Nusselt number* defined below as:

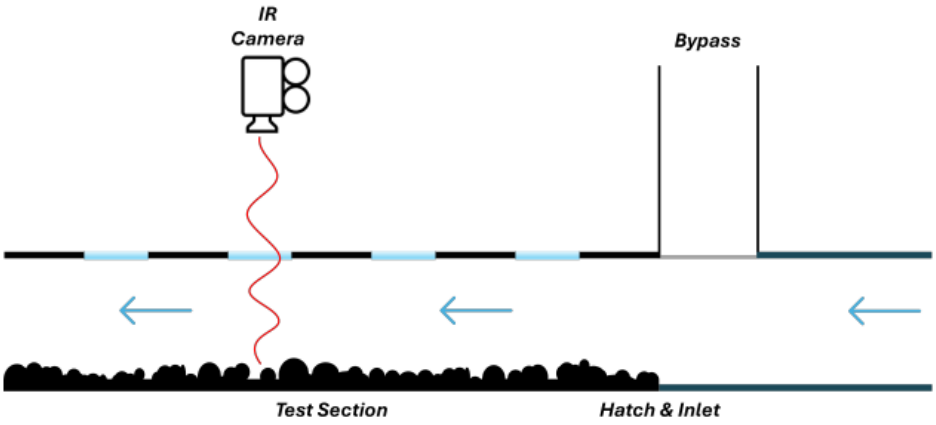
$$Nu = \frac{hL}{k} = \left.\frac{\partial T}{\partial y}\right|_{y=0} = 0$$

where L is a reference length scale and k is the thermal conductivity. It provides a measure of the convection heat transfer occurring at the surface. The Nusselt number is to the thermal boundary layer what the friction coefficient is to the velocity boundary layer [37]. The rig consists of a flow straightener, a bypass channel and a test section

where the test objects were installed. The ambient air is forced through a heating unit where its temperature is slowly increased. The heated air is then redirected to the bypass channel until the temperature stabilization is reached. Once the target temperature is achieved, as illustrated in Figure 3.1 the hatch is opened to allow the airflow to enter the test section. An infrared (IR) camera captures the transient evolution of the wall temperature by recording a video. The IR camera can be moved to several locations along the streamwise direction of the channel.



(a) Hatch closed and bypass opened



(b) Hatch opened and bypass closed

Figure 3.1: Schematic representation of the SRHT rig operation [86]

3.2 Working Principle

The SRHT rig works using a pressurized air system at 8 bar. The SRHT flow diagram is used to show the main components and instruments employed in the rig. *Valve 1* controls the main air flow and *Valve 2* is connected to the pneumatic actuator. Following the airflow path, downstream *Valve 1* the flow passes through an orifice meter, which

is used to evaluate the mass flow rate based on the pressure drop across the device. Later the air passes through the heater which gradually increases the fluid temperature. After passing the heater and before entering the test section, the flow enters the laboratory building as shown in Figure 3.2 with the dashed lines. *Valve 3* then reduces the pressure to 1.5 bar and it is used as a cold mass flow regulator. By adjusting this valve the mass flow rate can be controlled in order to achieve the desired *Re*. Downstream *Valve 3* a honeycomb is installed to reduce the turbulence intensity and lateral flow fluctuations. Thereafter the flow encounters the *Valve 4* which determines when the heated air enters the test section or continues through to the bypass channel.

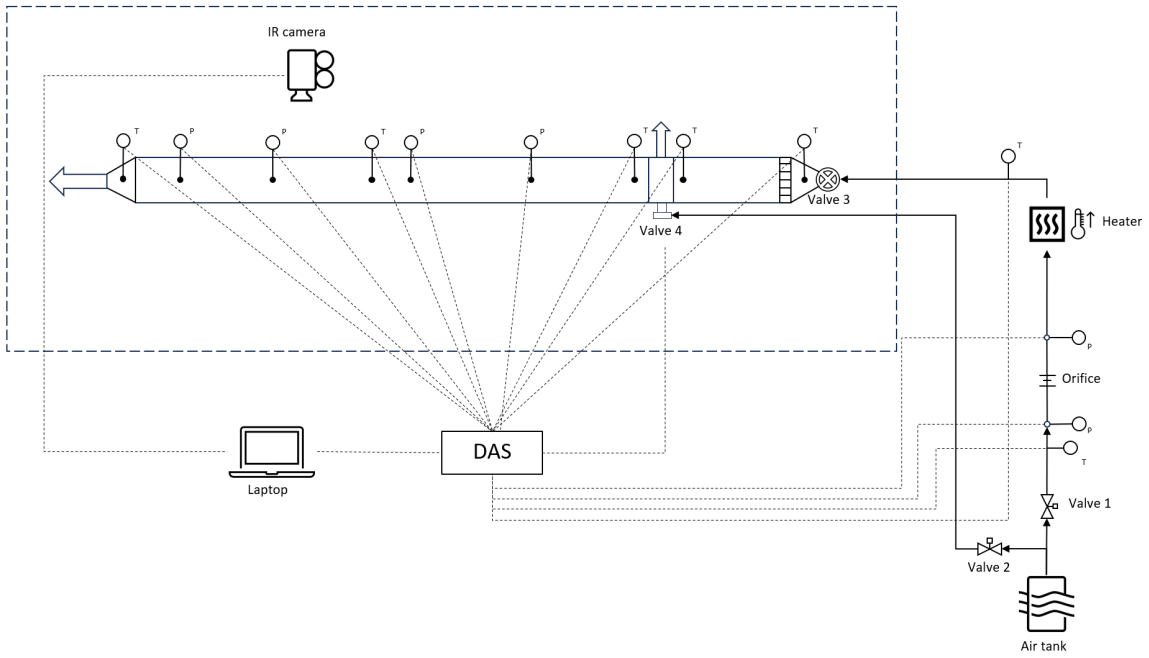


Figure 3.2: Schematic diagram of the SRHT rig

Before entering the test section, the air temperature is constantly monitored using *PT100* resistance temperature detector located at three different positions to measure the following temperature quantities:

1. *Heater Out*: the *PT100* sensor is positioned after the heater and the temperature registered should always be less than 120 °C for safety reasons.
2. *Safety*: the *PT100* sensor is positioned downstream of *Valve 3* and the temperature registered should always be less than 95 °C.
3. *Upstream Hatch*: the *PT100* sensor is positioned upstream of the hatch and the temperature registered by this probe was used to determine when the thermal stabilization is reached.

After crossing *Valve 4* the flow enters the test section. Several temperature and pressure probes are located within this section. In particular, three *k-type* thermocouples

are positioned along the longitudinal direction of the duct. Their readings are used to obtain the bulk flow temperature via linear interpolation. Although several pressure taps are present, they were not employed in this specific experimental work. Accurate test execution requires temperature stabilization and precise mass flow regulation via *Valve 3*. As introduced in Chapter 1, the main objective of the experimental investigation is to determine which SR parameters mostly influence heat transfer. To ensure reliable comparisons and achieve this goal, upscaled models were tested under flow conditions identical to those encountered within actual gas turbine cooling channels.

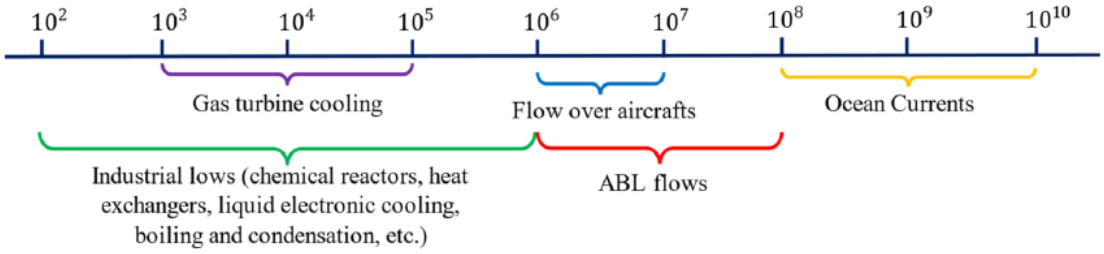
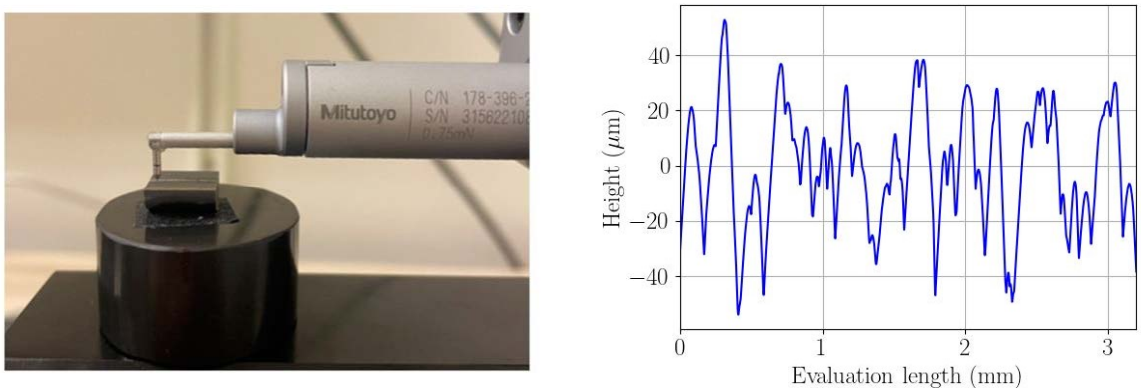


Figure 3.3: Typical bulk flow *Re* spectrum for natural and industrial heat transfer [87]

3.3 Analogue Rough Surface Modelling



(a) Skidless contact profilometer

(b) Surface profile

Figure 3.4: Surface roughness measurements

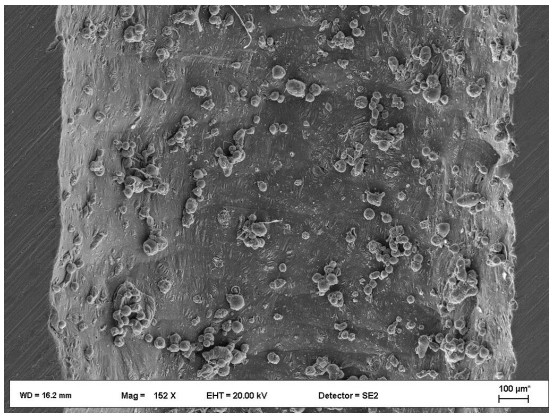
The upscaled roughness models investigated in this work do not reproduce any specific material employed in industrial gas turbines, unlike the models considered by Brogliato and Gissi [82, 86]. It is useful to review the evolution of the first upscaled roughness models introduced in the SRHT rig to comprehend how the research got to this point. Several test objects were designed based on the actual aluminum and INC939 cooling channels used in *Siemens Energy* gas turbines. For this purpose, a

skidless contact profilometer was employed to measure surface topography; additionally, high-resolution surface images were acquired for surface modelling using a *Jeol JSM-IT500* Scanning Electron Microscope (SEM) [82, 86, 91].

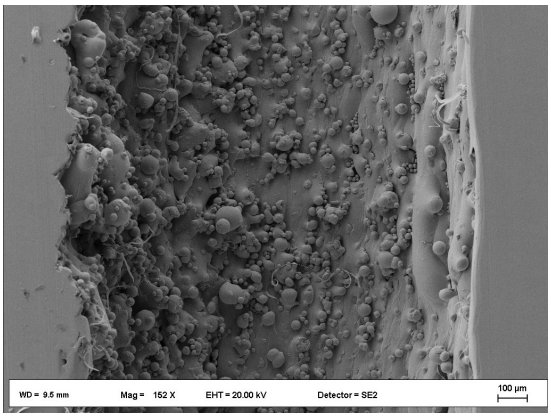
Because investigating local heat transfer effects on a real scale was unfeasible in the SRHT rig, upscaled test models were designed and tested. The technique of creating enlarged test objects is known as *Analogue Rough Surface* modeling. The upscaling factor s is obtained as the ratio between the hydraulic diameter of the SRHT duct to that of the real channel:

$$s = \frac{D_{h_{SRHT}}}{D_{h_{real}}}$$

Clemenson [56] first proposed the idea of studying AM surface roughness using upscaled models. Brogliato [82] in his work presents this approach highlighting the simplifications adopted.



(a) SEM image Aluminium



(b) SEM image Inconel 939

Figure 3.5: SEM images

As can be seen in Figure 3.5, there is a stochastic distribution of the residual features of AM process. The residual powder particles originated from the AM process were assumed to be spherical. Subsequently, the density of these spherical features and their height were considered relevant during the analogue surface modeling. The density ρ_s is defined as:

$$\rho_s = \frac{\text{number of spheres}}{A \cdot s^2}$$

where the numerator represents the total count of manually selected spheres from the SEM images, s is the upscaling factor, and A is defined as:

$$A = \frac{\pi}{2} R \cdot L$$

where R is the channel radius and L is the image length. The vertical height of the spheres, referred to as offset, is defined as the normalized vertical position of the spheres centroids:

$$\text{offset} = \frac{z}{D/2}$$

When the offset is equal to zero, it means that half of the sphere is embedded in the material, while the other half is exposed to the flow. Conversely, when the offset is equal to one, the sphere is completely exposed to the incoming flow. The dimensions of the rough test objects tested in this thesis work are reported in Table 3.1. The CAD model where designed starting from a Python code, where different parameters are set, including the spheres diameter, the offset and the spheres density. The rough surface was generated by importing this script in *Siemens NX* [61].

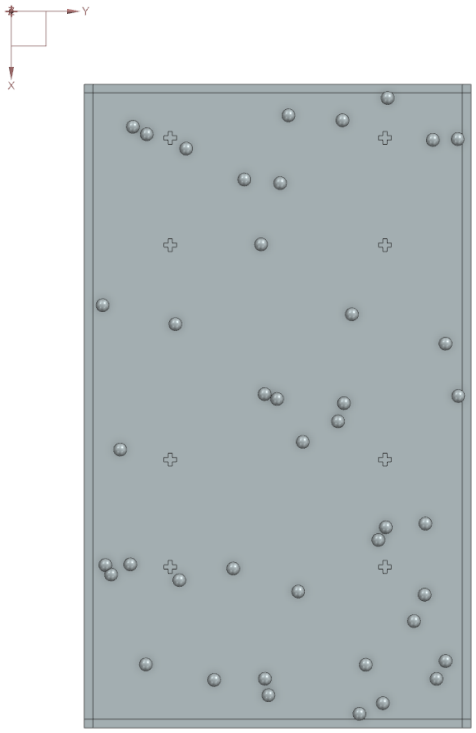
Parameter	**Value**
Length	150 mm
Width	90 mm
Height	15 mm
Layer thickness	0.1 mm

Table 3.1: Rough test object dimensions.

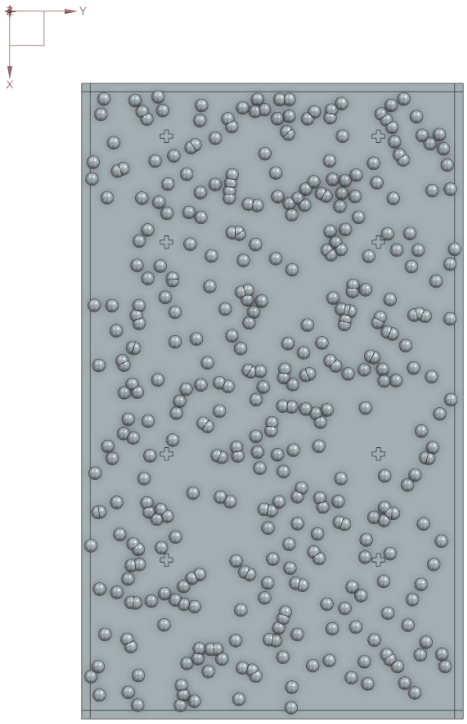
In Figure 3.6 are reported the four CAD models tested in the SRHT rig. Jankovskis in his work investigated the effect of the spheres diameter and compared his results with Gissi. As a conclusion, he proposed to investigate the effect of the spheres density. For this purpose several test objects were designed varying both the radius and the number of the spheres distribuited on the top surface. The offset was not changed and it has always been set to zero in both this and Jankovskis work. As a parametric study the aim is to understand the impact of each geometric and roughness parameters on heat transfer phenomena. For this reason, starting from the geomtries tested by Jankovskis, new test coupons with a higher and lower spheres density were generated and analyzed in this thesis. Table 3.3 summarizes the surface roughness parameters of the test objects studied.

3.4 SRHT-rig Setup

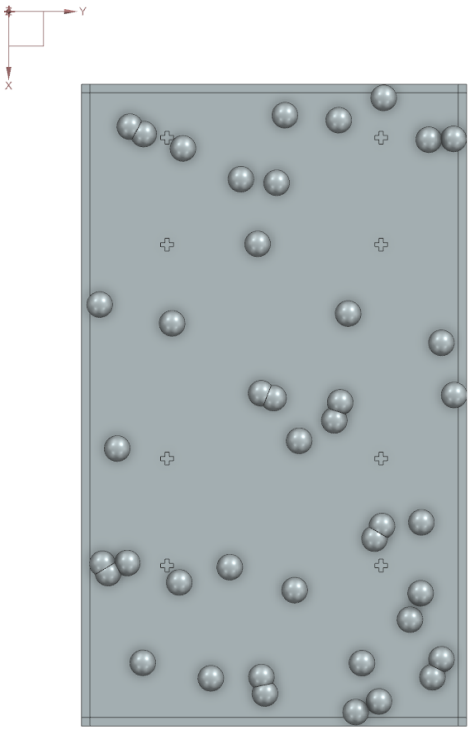
To comprehensively understand how the local HTC distribution was evaluated, this section provides a detailed overview of the main components of the facility, the associated measurement instrumentation, and the overall experimental setup.



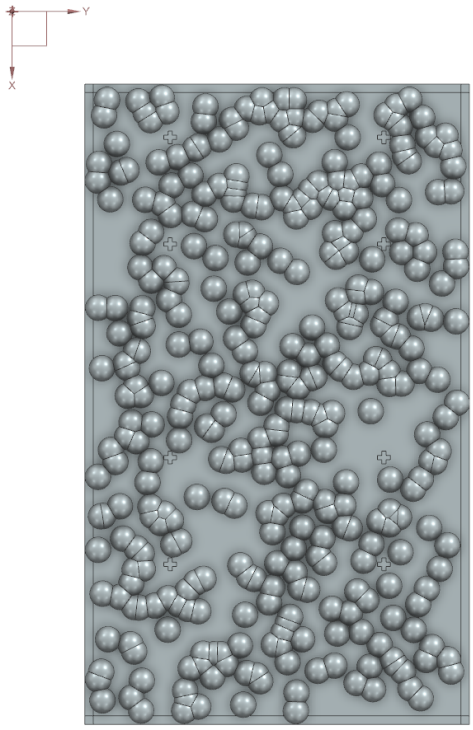
(a) *Rz*_015_00033 sparse



(b) *Rz*_015_003 dense



(c) *Rz*_030_00033 sparse



(d) *Rz*_030_003 dense

Figure 3.6: CAD models of the upscaled surface roughness plates

Geometry	D_s **[mm]**	***off***	**pts/mm^2**
Rz_015_00033_sparse	3	0	0.0033
Rz_015_003_dense	3	0	0.0300
Rz_030_00033_sparse	6	0	0.0033
Rz_030_003_dense	6	0	0.0300

Table 3.2: Python code parameters for rough model generation

Geometry	R_z **[mm]**	λ_p
Rz_015_00033_sparse	1.5	0.022
Rz_015_003_dense	1.5	0.1813
Rz_030_00033_sparse	3.0	0.0839
Rz_030_003_dense	3.0	0.5542

Table 3.3: Surface roughness parameters of the analyzed configurations

3.4.1 Test Rig

Table 3.4 reports the flow straightener dimensions. It is connected to an aluminium chamber featuring two outlets, one directed toward the bypass channel and the other toward the test section duct. A pneumatic actuator operates a shaft-mounted hatch capable of selectively blocking either the bypass or the test section inlet as schematically shown in Figure 3.1. The hatch cross-sectional area is slightly larger than that of the test section, generating a small step of 5 mm at the interface. This step generates a disturbance in the boundary layer development.

The test section is made of one top plate, two side plates and one bottom plate where the test objects are positioned. The top plate presents several circular openings at different streamwise positions along the duct. Every opening is covered by lids except for the one being tested, which is instead closed with an IR transparent window. The IR camera is located right above the IR window.

The dimensions of the test section are listed in Table 3.5. Along the bottom plate of the test section is possible to insert 10 plates. The plates and the test section have been produced by *Accura Xtreme Grey* using stereolithography (SLA). This AM technique employs a light source to cure a photopolymer resin contained within a reservoir [76]. The material used is a combination of plastic powder and the thermal properties are detailed in Table 3.6. The thermal properties differ from axial to radial direction [55]. The axial direction refers to the layer direction, whereas the radial one refers to in plane properties. Silicone gaskets and O-rings are used to reduce leakage between all the components of the rig.

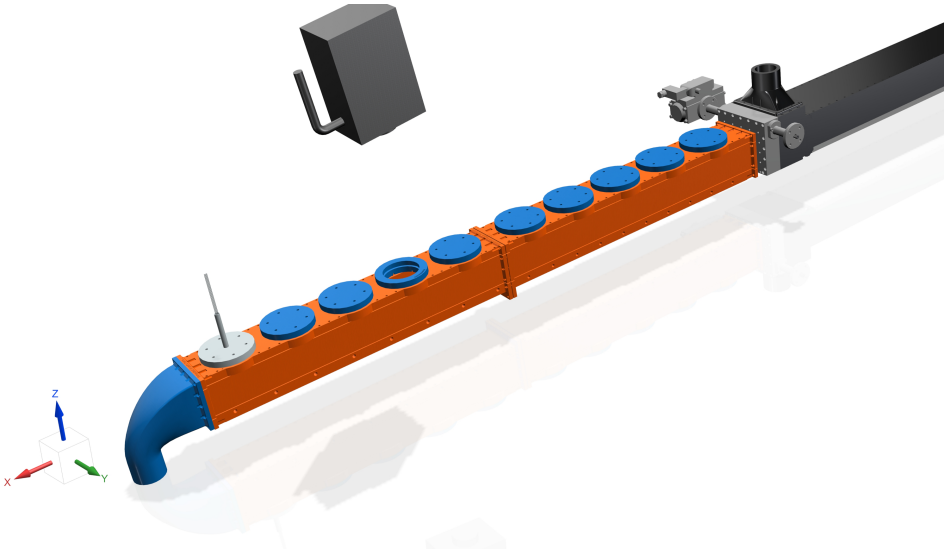


Figure 3.7: CAD model of the SRHT rig

Parameter	Value [mm]
Length	1000
Width	150
Height	97

Table 3.4: Flow straightener dimensions

3.4.2 Heater

The heater provides the thermal energy required to raise the air temperature to the desired target value. The system is composed of a power supply unit connected to resistive elements that generate heat through the Joule effect. The heater's operating conditions are set by the operator through a dedicated *Arduino* control system. To ensure safe operation, the system includes several protection devices.

3.4.3 IR Camera

The IR camera is the device used to register the transient temperature of the test objects, located at the bottom of the test section. The model that has been used is the *Titanium 560M* by *Cedip Infrared Systems*. Table 3.7 reports the technical details of the IR camera. In order to record the video of the experiment the IR camera was operated using the *FLIR ResearchIR* software. Once the IR camera was switched on it needed a couple of minutes to warm up before connecting to the software. When it was connected, an aluminium foil positioned on the bottom of the test section was used for two reasons:

Parameter	Value
Length	1000 mm
Width	150 mm
Height	97 mm
Fillet radius	5 mm
Hydraulic diameter	96.7 mm
Test section cross area	8980 mm^2
Layer thickness	0.1 mm

Table 3.5: Test section's geometrical dimensions.

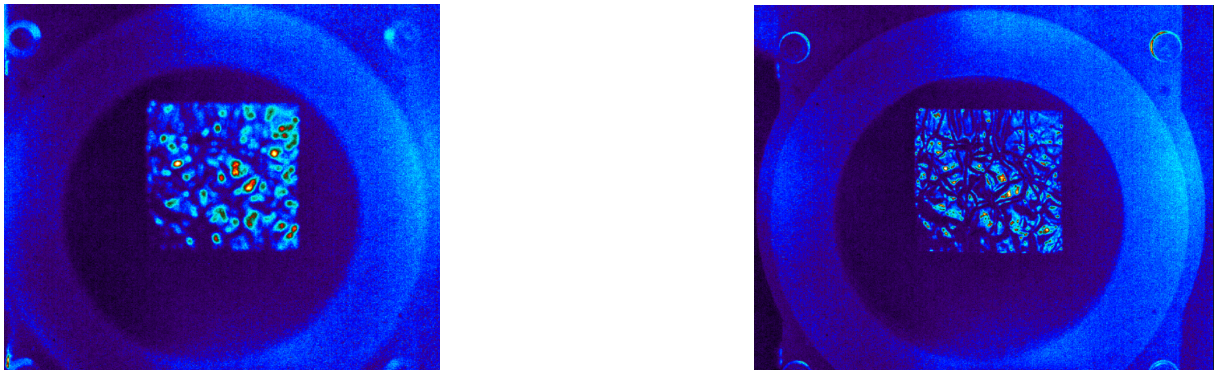
$\mathbf{T}$ [°C]	$\mathbf{k_{ax}}$ [W/mK]	$\mathbf{k_{rad}}$ [W/mK]	$\mathbf{c_p}$ [J/kgK]
30	0.224	0.211	1442.4
50	0.227	0.237	1735.9

Table 3.6: Accura Xtreme Grey thermal properties in axial and radial directions

1. *IR Camera's Focus*: by rotating the camera's len it is possible to obtain a clean image as shown in Figure 3.8.
2. *IR Camera's Position*: achieving the optimal camera position and configuration is a crucial factor for successful testing. To do so, the camera is mounted on a rigid support that allows adjustments across three degrees of freedom. The regulation is done to avoid the reflection of the camera on the IR window, to minimize the sidewall reflections and to have a clear top-down view of the test section. Further details about the specific angles adopted to ensure a good recording are given in the final section of this chapter.

The IR camera calibration is a crucial part in this experimental work. The IR camera does not directly capture the temperature but the radiometric signal. To account for this, a calibration function is introduced. Based on the expected temperature range of 20 °C to 70 °C, the camera's *Integration Time* (IT) was set to 1200 µs. Integration time corresponds to the duration during which the detector accumulates incident infrared energy before readout. The frame rate chosen was of 10 Hz.

Within the framework of IRT, two critical aspects frequently lead to measurement inaccuracies: the lack of knowledge of surface emissivity and the geometric limitations related to the spot size [29]. An IR calibration source was employed to correlate the radiometric signal to the actual temperature. This device is shown in Figure 3.9(b) and it is the *DIAS CS110* by *DIAS Infrared System*. This device features a known emissivity of $\varepsilon_{CS} = 0.98 \pm 0.01$ and a calibration temperature range of −15°C to 110°C



(a) Not focused (b) Focused

Figure 3.8: IR camera focus procedure

(258.15 K to 383.15 K), with an uncertainty of $\Delta T_{CS} = \pm 0.5\,\mathrm{K}$ [96]. Gissi [86] performed the calibration, and for every temperature step, a radiometric signal was registered and corrected for the calibrator's emissivity. A curve-fitting approach is typically used in IRT to establish a continuous relationship between radiometric signals and absolute temperatures [29]:

$$T = A \cdot S^{1/2} + B \cdot S^{3/2} + C \cdot S^2 + D \cdot \ln(S) + T_0$$

A, B, C, D and T_0 represent the parameters for the fitting curve while S is the detected radiometric signal.

Parameter	**Value**
Sensor Type	InSb
Waveband	3–5 μm or 8–12 μm
Pixel Resolution	640×512
Integration Time	1200 μs
Frame Rate	10 Hz
Calibration Temperature Range	$-15\,^{\circ}\mathrm{C}$ to $+100\,^{\circ}\mathrm{C}$
Calibration Device	DIAS CS110

Table 3.7: *Titanium 560M technical details*

In Figure 3.10 the calibration function curve is reported, alonside its regression error. In Table 3.8 the values of the correlation constants used for the curve fitting are reported. Once the calibration function is determined, it is possible to transform the raw signal into temperature values. The calibration function is referred to as $F_{S \to T}$. Additionally, Gissi determined the inverse function $F_{T \to S}$, from temperature to signal, using a numerical interpolation in *Matlab*.



(a) Titanium 560M (b) DIAS CS110

Figure 3.9: IR camera and calibration device

Parameter	A	B	C	D	T_0
Value [K]	-0.2549	2.0853×10^{-5}	-8.3719×10^{-8}	38.578	-9.1824

Table 3.8: Values of the fitting curve parameters

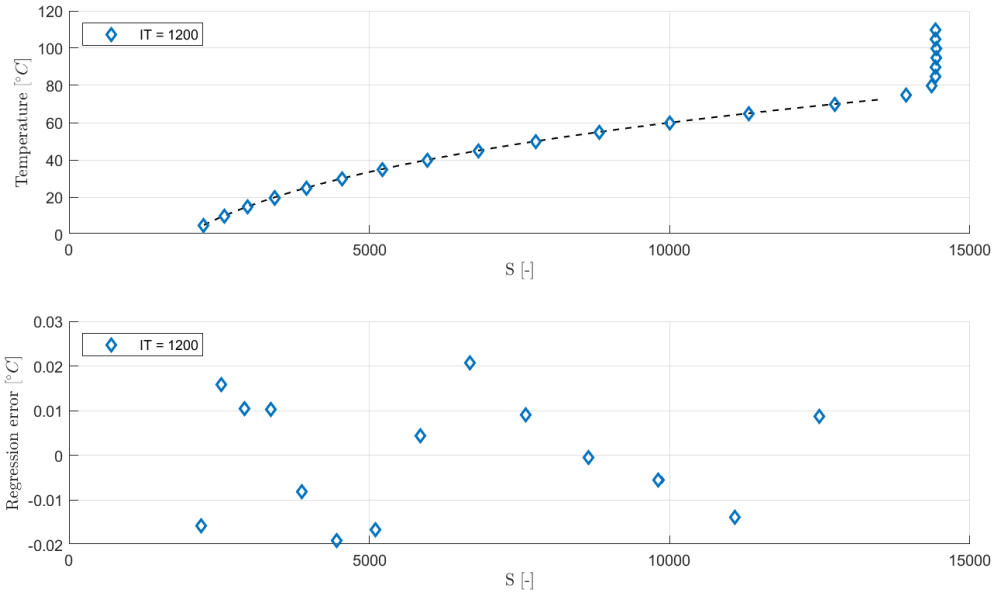


Figure 3.10: IR camera calibration curve and its regression error [86]

3.4.4 IR Window

An IR window is needed for any kind of IRT experiments. The one employed in the SRHT rig is the *IRW-4C* designed and built by *FLIR*. It is made of high-transmissivity calcium fluoride, which is the perfect solution for any length wave IR imaging. The optical properties were initially unknown and were experimentally determined by Lehmann [77]. The optical properties of the IR window and the black paint are listed in Table 3.9 alongside the IR window optical dimensions.

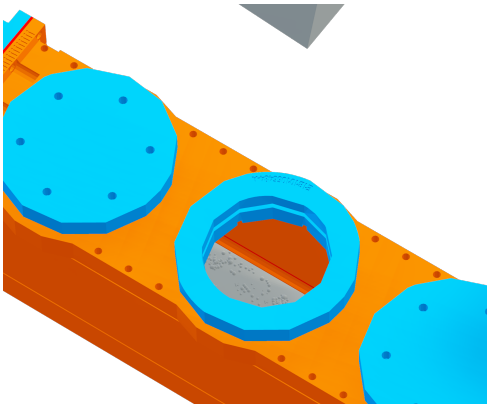


Figure 3.11: Top view of the IR window

3.4.5 IR Paint

Using black paint for IRT experiments can enhance the quality of the captured results by improving the emissivity of the target body. The closer this emissivity is to that of an ideal blackbody, the higher the measurement accuracy [29]. For this reason, the test objects and the inner surfaces of the test section were coated with a thin layer of high emissivity black paint. The paint used for this purpose is a *Senotherm* product, whose thermal and emissivity properties were not known. The optical properties of the black paint were determined by Lehmann[77] and reported in Table 3.9.

	IR window	**Black Paint**
Emissivity ε	—	0.9072 ± 0.0274
Reflectivity ρ	0.9489 ± 0.0334	0.0540 ± 0.0062
Transmissivity τ	0.0501 ± 0.0068	—
Optical diameter	95 mm	—
Window thickness	29.15 mm	—

Table 3.9: Optical properties of the IR window and black paint

3.4.6 Data Acquisition Systems

The DAS (Data Acquisition System) used in the SRHT rig consists of a series of elements in order to:

- Measure the physical quantities.
- Amplify and filter the signals collected using signal conditioning units.
- Digitize the signals using an analog-to-digital converter.

To monitor the real-time evolution of the physical quantities, an in-house program named *RigView* was employed. Additionally, the software can collect and store data from all the measurement devices distributed along the rig.

Netscanner 9116 and the *Keysight Agilent 34972A* are the two units employed in the rig. The former is a 16-channel piezoresistive pressure transducer, with a pressure measurement range from −100 psi to 100 psi, and a full-scale accuracy of ±0.05 %. The latter is a data logger used to monitor temperature readings, mass flow, and the ambient absolute pressure. The ambient pressure is measured using a *Rosemount 2008* and a gauge pressure transmitter. These units are connected to the computer via the TCP/IP protocol.



(a) Netscanner 9116 (b) Keysight Agilent 34972A (c) Rosemount 2008

Figure 3.12: Data Acquisition System

For evaluating local heat transfer effects the rig is equipped with several temperature probes. Two types of probes were used:

- *PT100*: it is a resistance temperature detector (RTD) based on the temperature dependence of platinum's electrical resistance. Its working principle is based on the linear increase in resistance as temperature rises, with a nominal resistance of 100 Ω at 0 °C. PT100 sensors provide highly accurate and stable measurements

over a wide temperature range. However, their response time is generally slower compared to thermocouples.

- *K-Type Thermocouple*: they operate according to the Seebeck effect, where a voltage is generated between two dissimilar metals subjected to a temperature gradient. The main advantages of this sensor are its wide operating temperature range, fast response time, and high mechanical robustness, making it suitable for harsh environments and easy to integrate into the rig architecture. However, they provide a lower accuracy than PT100.

3.5 Experimental Data Acquisition

To assess the heat transfer coefficient (HTC) distribution, a comprehensive understanding of data collection and processing is required. This section outlines how experimental data were collected and processed. Four upscaled rough models were tested during this experimental campaign, at five different streamwise locations along the duct, at four Reynolds numbers. Table 3.10 reports all the experimental and fluid-dynamic conditions. Testing a single geometry, for all the positions and fluid-dynamic conditions, required a minimum of twenty tests, considering that each run was successful. Between consecutive tests, a minimum time of three hours was required to allow the test samples to return to initial temperature. As shown below, the mass flow rate is the only physical quantity used to define the correct fluid-dynamic condition, once the hydraulic diameter and the cross-sectional area are known.

$$Re = \frac{D_h \dot{m}}{\mu_{air} A}$$

The air viscosity μ_{air} is determined using the *Sutherland's law* and it depends on the measured air temperature.

$$\mu_{air}(T) = \mu_0 \left(\frac{T}{T_0} \right)^{3/2} \frac{T_0 + S}{T + S}$$

where $\mu_0 = 1.716 \times 10^{-5}$ Pa s, $T_0 = 273.15$ K and $S = 110.4$ K. As widely explained, the core idea of the SRHT rig is to heat the air to a target temperature and, once thermal stabilization is reached, open the hatch, allowing the hot air to flow into the test section duct. The $Re = 10000$ condition is the most challenging in terms of temperature stabilization, as multiple input adjustments are needed to execute the test safely. Thermal stabilization is assumed when air temperature does not change more than 1 °C over the last two minutes before the test is started. For the HTC evaluation, two temperature measurements are required:

1. *Wall Temperature*: the IR camera records a video of the bottom part of the duct where the test objects are located. The video captures the transient evolution of

the sample's wall temperature, pixel by pixel, which is converted into temperature data using the calibration function.

2. *Bulk Air Temperature*: three k-type thermocouples are positioned at the inlet, middle, and outlet location of the duct. The temperature readings are subsequently linearly interpolated to obtain the bulk temperature, under the linear temperature profile assumption along the duct.

Parameter	**Value**
Windows tested	1, 2, 5, 9, 10
Re	10000, 15000, 20000, 25000
$\dot{m}$	10.0, 28.5, 38.0, 47.5 $\mathrm{g\,s^{-1}}$
Test duration, t	110 s
Sampling frequency, f_s	10 Hz
Target temperature	70 °C

Table 3.10: Experimental and Fluid-Dynamic Conditions

3.6 Data Processing

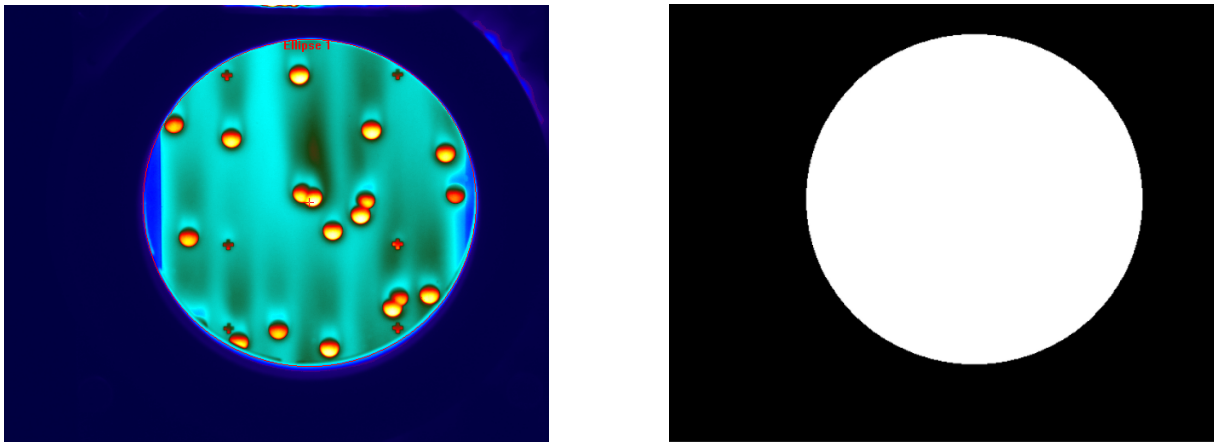
In this section, the details regarding the transient test data are analyzed and presented. The inputs consist of an IR video and a *.txt* file where all the sensor readings acquired during the test run are stored. A reduced-size CAD model of the test object is then generated to create a computationally less expensive mesh. Using a mapping procedure it was possible to move from the IR camera coordinate system into the real coordinate system, enabling the HTC spatial distribution calculation. Using in-house finite element software, it was possible to obtain the HTC distribution from the collected data. Finally, the results are presented and discussed in Chapter 4.

3.6.1 IR Video

The IR video was acquired using the *FLIR ResearchIR* software and stored in a *.PTW* format. The IR recording is used for several reasons:

1. *Starting Frame*: the exact starting frame can be identified by synchronizing a light source located next to the IR window with the pneumatic actuator employed to open the hatch.

2. *Region of Interest*: an elliptical ROI is manually selected for each test as shown in Figure 3.13(a). Only the data within this region are used to calculate the HTC distribution. The ROI is exported as a binary mask, as shown in Figure 3.13(b), and the calibration function is used to convert the radiometric signal into temperature data.



(a) IR video frame (b) ROI binary mask

Figure 3.13: Elliptical ROI

3. *Flat Point*: a reference point within the flat region of the ROI is manually selected as far as possible from the side walls. Its spatial coordinates are used to extract the local wall temperature, which is then taken as the representation of the wall temperature.
4. *Reference Points*: a minimum of six reference points at different heights were selected to ensure an accurate mapping process. Four of these reference points are chosen by selecting the center of four crosses that form a square ROI.

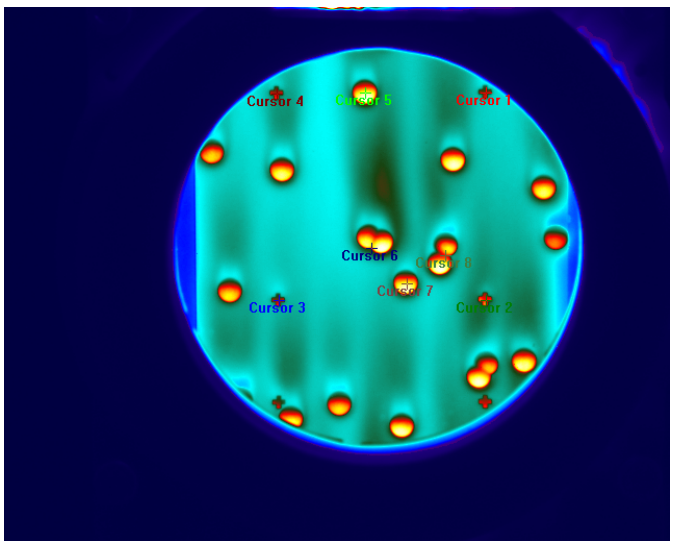


Figure 3.14: Reference Points

Figure 3.15 presents a schematic representation of the radiative sources that contribute to the detected signal S_{det} from the IR camera. The signal captured by the IR camera is influenced by its positioning above the IR window. A sensitivity analysis was necessary to assess the impact of the camera's location on the HTC distribution. The detected

signal captured by the IR camera consists of multiple contributions, which include the radiation coming from the painted test objects, the ambient radiation reflected by both the paint and the IR window, and the radiation emitted by the inner sidewalls of the duct.

$$
\begin{aligned}
S_{\text{det}} = {} & \varepsilon_{\text{paint}} \tau_{\text{IRW}} S_B && \text{(a) Plate emission} \\
& + \tau_{\text{IRW}}^2 \rho_{\text{paint}} S_{\text{amb}} && \text{(b) Ambient reflected by plate} \\
& + \rho_{\text{IRW}} S_{\text{amb}} && \text{(c) Ambient reflected by window} \\
& + \varepsilon_{\text{paint}} \rho_{\text{paint}} \tau_{\text{IRW}} S_w && \text{(d) Wall emission reflected by plate}
\end{aligned}
$$

where S_{det} is the radiation signal recorded by the camera, S_b is the radiation emitted by a blackbody which is at the same temperature as the painted test object, S_w is the radiation emitted by the channel sidewalls, and S_{amb} is the ambient radiation signal.

As mentioned before, the channel wall temperature is evaluated using the *Flat Point*. Alternative approaches were not feasibile due to space constraints about camera positioning and the difficult integration of other sensors for measuring the sidewalls temperature. Assuming $S_b = S_w$ it is possible to isolate S_w.

$$
S_w = \frac{S_{\text{det,flat}} - \left(\rho_{\text{IRW}} + \rho_{\text{paint}} \tau_{\text{IRW}}^2\right) S_{\text{amb}}}{\varepsilon_{\text{paint}} \tau_{\text{IRW}} \left(1 + \rho_{\text{paint}}\right)}
$$

Once S_w is known, the corrected blackbody signal S_b, which takes in consideration all these radiometric contributions, can be written as:

$$
S_B = \frac{S_{\text{det}} - \left(\rho_{\text{IRW}} + \rho_{\text{paint}} \tau_{\text{IRW}}^2\right) S_{\text{amb}} - \varepsilon_{\text{paint}} \rho_{\text{paint}} \tau_{\text{IRW}} S_w}{\varepsilon_{\text{paint}} \tau_{\text{IRW}}}
$$

Finally using the calibration function the corrected signal S_b can be converted into surface temperature.

3.6.2 Mapping

Reflections can significantly affect the results obtained from IRT. A perpendicular alignment of the camera with respect to the IR window was not adopted to avoid reflections from the camera itself. This makes the *mapping* process necessary for two reasons. First, the IR camera captures a geometrically distorted scene due to its inclination. Second, mapping is required to transform the measurements from the camera coordinate system to the physical space of the test object.

To successfully perform the mapping process, a mesh was generated from the CAD model in *Siemens NX*. The details regarding the mesh generation are reported in Table 3.11. Moreover, to reduce the computational cost of the mesh, two different mesh

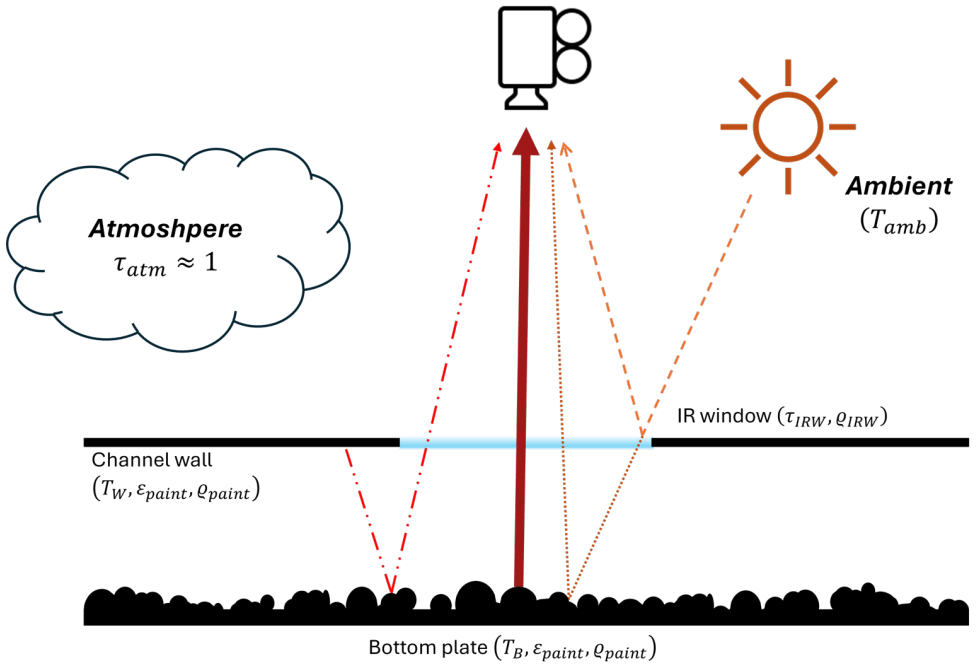


Figure 3.15: Schematic representation of the main contributions to the detected signal

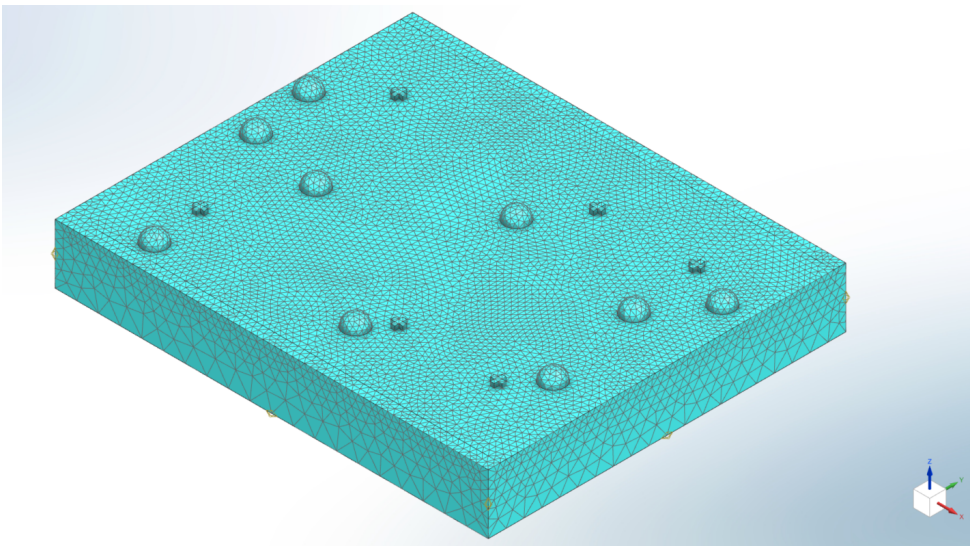


Figure 3.16: Mesh of the reduced CAD model in *Siemens NX*

controls of type *Number on Edge* were applied. The first mesh control was assigned to the four vertical edges, while the second one was assigned to the edges of the bottom face as shown in Figure 3.16.

A camera projection matrix is essential to perform the geometrical transformation to the real coordinate system.

$$\begin{bmatrix} u \\ v \\ 1 \end{bmatrix} = \begin{bmatrix} p_{11} & p_{12} & p_{13} & p_{14} \\ p_{21} & p_{22} & p_{23} & p_{24} \\ p_{31} & p_{32} & p_{33} & p_{34} \end{bmatrix} \begin{bmatrix} X \\ Y \\ Z \\ 1 \end{bmatrix}$$

where (u, v) are the camera coordinates and (X, Y, Z) are the 3D CAD coordinates. The camera projection matrix P accounts for both camera's intrinsic parameters and the specific geometric transformation matrices. It can be written as:

$$P = K[Rt]$$

where K is the intrinsic calibration matrix that contains the focal length and lens distorsion effect, R is the rotation matrix and t is the translation vector. The camera projection matrix can be rewritten as a vector p:

$$p = \begin{bmatrix} p_{11} & p_{12} & p_{13} & p_{14} & p_{21} & p_{22} & p_{23} & p_{24} & p_{31} & p_{32} & p_{33} & p_{34} \end{bmatrix}^T$$

Each 3D-to-2D point correspondence provides two equations. Therefore, at least six points at different heights are required to solve the system. Using more points ensures greater precision in the calculation. These *Reference Points*, chosen from the CAD model, must be the same as those chosen from the IR video otherwise, the transformation cannot be successfully performed.

The mapping result is reported in Figure 3.17. The blue dots represent the mesh points in the elliptical ROI. The blue circles represent the points selected from the IR video while the black asterisks represent the results of the projection with the matrix P.

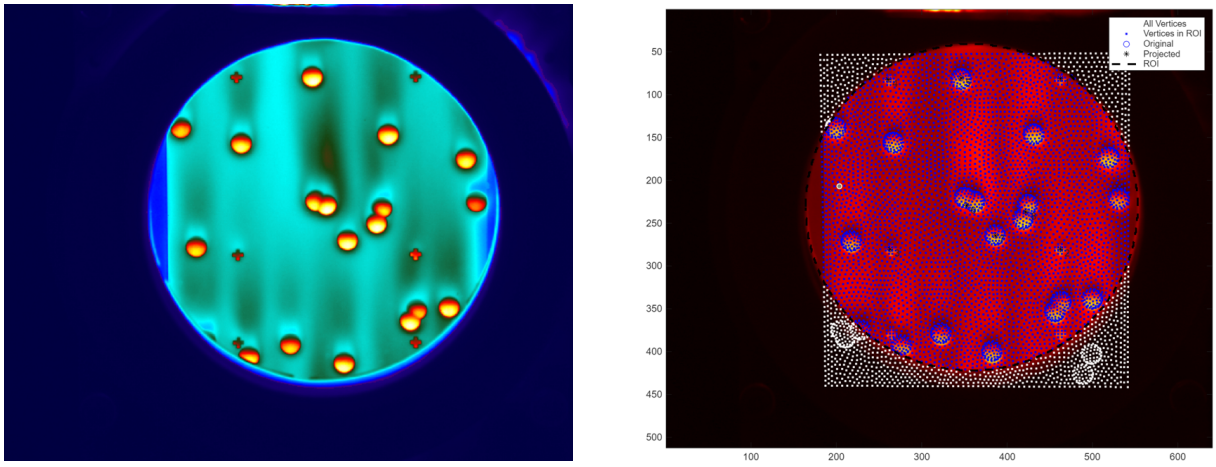
The visual alignment, along with the fact that blue circles and black asterisks almost completely overlap, shows the accuracy of the mapping procedure. Furthermore, with the parameters used for the mesh generation, a good mesh is guaranteed, especially on the spherical elements and where they merge. Consequently, the resulting HTC distribution can be considered accurate.

3.6.3 C3D Software

C3D is the finite element software employed to extract the HTC distribution. It is an in-house proprietary software of Siemens Energy AB and for this experimental work it was mainly used to calibrate the temperature field, recorded by the IR camera, and

MESH RECIPE INFORMATION	
Element Type	DC3D10
MESH PARAMETER	
Automatic Element Size	False
Element Size	1.5 mm
Surface Maximum Growth Rate	1.5
Surface Meshing Methods	Mesh From Facets
SURFACE MESH SETTINGS	
Minimum Element Size (% of target element size)	2.6
Minimum Element Size	0.039 mm
Level of Discretisation Based on Curvature	25
Distance Based Refinement	false
Surface Proximity Based Refinement	False
Edge Proximity Based Refinement	False
VOLUME MESH SETTING	
Internal Mesh Gradation	1
Target Internal Edge Length Limit	False
Minimum Two Elements through Thickenss	True
MODEL CLEANUP OPTIONS	
Small feature tolerance (% of element size)	15.5
Minimum element length (read only)	0.2325

Table 3.11: Mesh Generation Properties



(a) IR video last frame (b) Mapping result

Figure 3.17: Mapping Procedure

the numerical results computed by the software. More details are provided in the following section, where the solver methodology is accurately explained. Once the mesh is created and the mapping process is completed, it is possible to prepare the software for the simulation. In *Siemens NX* the mesh is exported as a *.inp* file, to be later imported inside *C3D*. A specific region named *mapping* is created by selecting only the mesh faces within the camera line of sight. For this reason, at least one layer of faces was not selected due to this camera constraint. Figure 3.18 shows how the mapping region was created. This operation drastically reduces the calibration error.

Boundary conditions were applied, including both HTC and gas temperature conditions, to the top, bottom, and lateral edges. The values are listed in Table 3.12.

Boundary Conditions	**Top**	**Bottom**	**Edges**
HTC [W/m^{2}K]	40	10	0
Gas Temperature [°C]	70	20	0

Table 3.12: Boundary conditions applied to the numerical model

The *Gas Temperature Scaling Curve* is created as described in the C3D manual [62]. It is used to provide boundary values for the created regions. When the scaling curve is created the first column represents the time steps, whereas the second one contains the corresponding temperature values. The actual boundary condition is applied using this formulation:

$$T = T_{ref} + s(T_{ss} - T_{ref})$$

where T_{ref} is the reference temperature. A value of 20 °C was used. T_{ss} is the steady

state temperature ideally of 70 °C that it is desiderable to obtain in the test section and s is the *scaling factor*. The scaling factor s is defined as:

$$s = \frac{T_{bulk}}{T_{ss}}$$

where T_{bulk} is the bulk temperature inside the test section, linearly interpolated based on the readings of the three thermocouples.

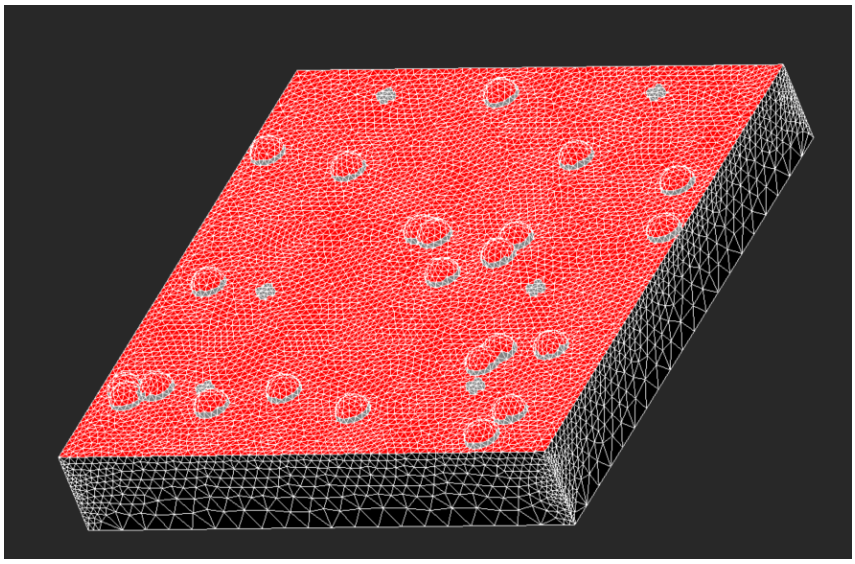


Figure 3.18: C3D Mapping Region

The material properties listed in Table 3.6 were used to generate the material inside C3D. A new region was created and named *rough* where all the mesh surfaces were selected. The rough region was used to apply the boundary conditions and to assign the scaling curve. The main reason two specific regions were created is that the mapping region is used to map the CAD model to the data registered by the IR camera. Conversely, the rough region is where boundary conditions were applied.

A *Conjugate Solver* is subsequently executed using the assigned boundary conditions. A *Transient Simulation* is performed using time steps assigned in the transient scale curve and reported below:

$$t = [0, 10, 20, 40, 70, 100]\,\mathrm{s}$$

The result of the conjugate simulation is reported in Figure 3.19. Under the Aero View section, all Aero Faces were selected excluding the vertical edges of the crosses. They represent the wetted region where the fluid directly impinges on the surface. More details are provided in [62].

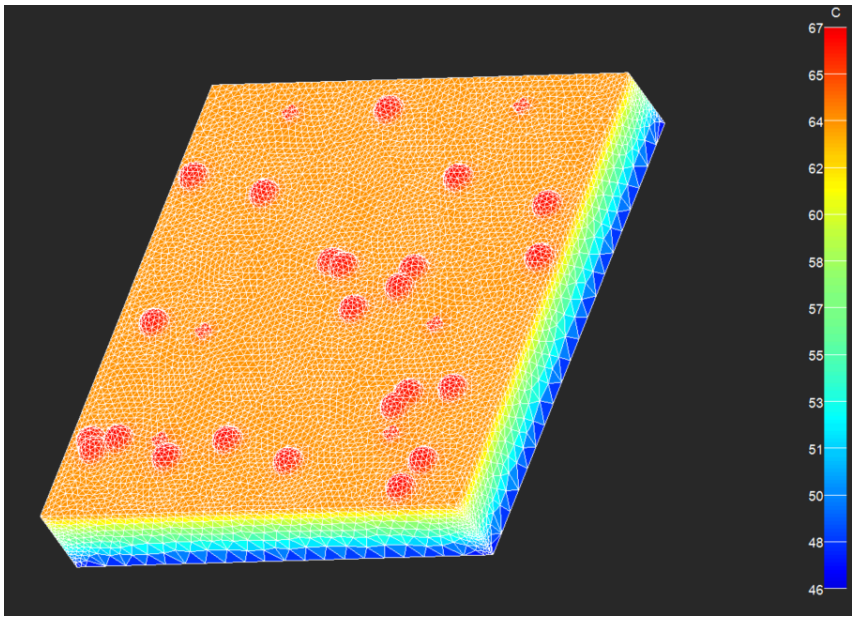


Figure 3.19: Temperature field after conjugate simulation

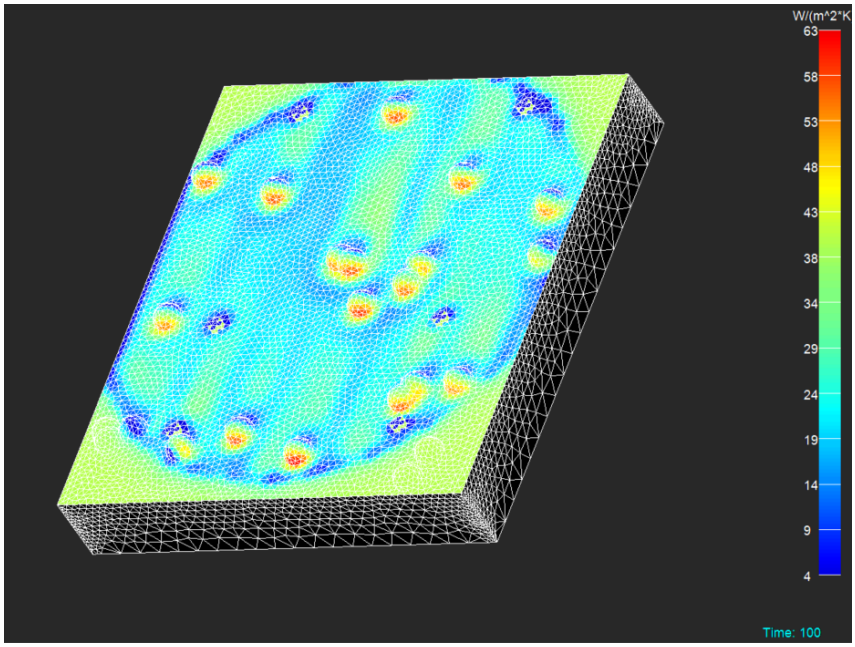


Figure 3.20: HTC spatial distribution after the calibration simulation

The final part is concerned with the calibration setting preparation. Once the mapping has been completed and the test executed, it is necessary to edit the gas scaling curve, replacing the scaling factor s with the appropriate values calculated from the linearly interpolated bulk temperature. For each time step, the IR camera data are imported into C3D, which then has two different temperature distributions: the numerical field computed within C3D based on the assigned boundary conditions, and the experimental field representing the recorded temperature data. Using the *Calibration Solver* is possible to match these temperature fields and extract the HTC distribution. The final result, shown in Figure 3.20, is the HTC distribution on the top surface of the rough plate. The spatial HTC distribution is finally exported and post-processed. These results are discussed in Chapter 4.

3.6.4 Underlying Equations

This section outlines the core equations employed to extract the HTC distribution. The theoretical equations used in the 1D solver to determine the thermal performance of smooth plates are reported in the works of Gissi and Brogliato [82, 86].

A three-dimensional approach is required for the rough test samples analyzed in this work due to the rough spherical features on the surface. The HTC distribution is evaluated through an inverse procedure that involves solving both the direct and adjoint problems. Adjoint equations are suited for optimization problems where a scalar-valued target function is optimized with respect to a large number of design variables [52].

This procedure is implemented in in-house software named *C3D*. After the mapping process, the HTC distribution is continuously adjusted, iteration by iteration, so that the calculated surface temperature matches the recorded surface temperature. The target function is a least-squares fit between calculated and measured transient metal temperatures. The design variables consist of heat transfer coefficients on a set of mesh facets for a finite element mesh. The governing equations for the direct problem are:

$$\begin{cases} \rho c \dfrac{\partial T}{\partial t} = \nabla \cdot (k \nabla T) & \text{in } \Omega, \quad 0 \le t \le t_f, \\ k \dfrac{\partial T}{\partial \hat{n}} = h\left(T - T_g\right) & \text{on } \Gamma, \quad 0 \le t \le t_f, \\ T(x, t=0) = T_0(x) & \text{in } \Omega. \end{cases}$$

where $k(x,T)$ is the thermal conductivity of the material, $\rho(x,T)$ is the density, $c(x,T)$ is the heat capacity, $h(x,t)$ is the heat transfer coefficcient, $T_g(x,t)$ is the gas temperature and n is the outward normalized vector. Ω denotes the solid domain and Γ its border. The objective is to modify the HTC in order to minimize the target function defined as:

$$J = \frac{1}{2}\int_0^{t_f}\int_\Gamma \left(T(x,t) - T_m(x,t)\right)^2 \, d\Gamma \, dt$$

where $T(x,t)$ is the calculated temperature and $T_m(x,t)$ is the measured metal surface temperature recorded by the IR camera. $T(x,t)$ has to satisfy the governing system of equations. According to the Lagrangian formulation, solving this minimization problem requires finding stationary points of the corresponding Lagrangian function $L(h,\lambda)$.

$$L(h,\lambda) = J + \int_0^{t_f}\int_\Omega \lambda(\mathbf{x},t)\left(\rho c\frac{\partial T}{\partial t} - \nabla\cdot(k\nabla T)\right) d\Omega dt$$

where λ is the *Lagrange multiplier*. Stationary points of the Lagrangian function can be found by imposing that the variations δL_λ and δL_h are equal to zero. The finite difference formula is used to approximate δL_h. A variation of δh causes a change δT in the temperature field. The variation δL_h, after some algebraic manipulations detailed by Jaksch [52], becomes:

$$\begin{aligned}\delta L_h = &\int_0^{t_f}\int_\Omega \delta T\left(-\rho c\frac{\partial \lambda}{\partial t} - \nabla\cdot(k\nabla\lambda)\right) d\Omega\, dt \\ &+ \int_0^{t_f}\int_\Gamma \delta T(T - T_m)\, d\Gamma \, dt + \int_\Omega \lambda\rho c\, \delta T(t = t_f)\, d\Omega \\ &+ \int_0^{t_f}\int_\Gamma k\left(\delta T\frac{\partial \lambda}{\partial n} - \lambda\frac{\partial \delta T}{\partial n}\right) d\Gamma \, dt\end{aligned}$$

The δL_h has to be equal to zero at a stationary point of the Lagrangian formulation. The variation δT is an arbitrary function and λ is selected to satisfy this system:

$$\begin{cases} -\rho c\frac{\partial \lambda}{\partial t} = \nabla\cdot(k\nabla\lambda) \quad \text{in } \Omega, \quad 0 \le t \le t_f \\ k\frac{\partial \lambda}{\partial \mathbf{n}} = h\lambda - (T - T_m) \quad \text{on } \Gamma, \quad 0 \le t \le t_f \\ \lambda(\mathbf{x}, t_f) = 0 \quad \text{in } \Omega \end{cases}$$

With this choice of λ the variation δL_h becomes:

$$\delta L_h = -\int_0^{t_f}\int_\Gamma \delta h\lambda(T - T_g) d\Gamma \, dt$$

Using the substitution $\tau = t_f - t$ is possible to obtain:

$$\begin{cases} \rho c \frac{\partial \lambda}{\partial \tau} = \nabla \cdot (k \nabla \lambda) \quad \text{in } \Omega, \quad 0 \leq \tau \leq t_f \\ k \frac{\partial \lambda}{\partial \mathbf{n}} = h\lambda - (T - T_m) \quad \text{on } \Gamma, \quad 0 \leq \tau \leq t_f \\ \lambda(\mathbf{x}, 0) = 0 \quad \text{in } \Omega \end{cases}$$

which is the adjoint problem that looks almost identical to the direct problem. Due to the temporal transformation $\tau = t_f - t$, this system must be integrated backward in time, which in turn requires the temperature field T to be accessible across the entire optimization window. For large-scale numerical simulations, storing the full time history of T imposes a severe memory bottleneck. To overcome this limitation, a checkpointing strategy was implemented: the forward solution is saved to disk only at discrete time intervals. The temperature values $T(\tau)$ needed during the adjoint sweep are subsequently reconstructed via linear interpolation between consecutive checkpoints. Similarly, taking the variation with respect to λ (δL_λ) recovers the original forward (direct) problem, whose explicit derivation is omitted here for brevity.

It is important to assess how a change in h can affect the target function J. The sensitivity of J is defined as the derivative of the target function with respect to the value of h at a certain location x and time t and denoted as J'_h. The operating method procedure can be finally outlines:

1. Solve the direct problem to obtain the temperature distribution $T(x,t)$ for an initial guess of h.
2. The calculated temperature $T(x,t)$ and the measured temperature by the IR camera are then used as an input to solve the adjoint problem to calculate $\lambda(x,t)$.
3. With $\lambda(x,t)$ and the temperature field the sensitivity is evaluated.
4. To update the heat transfer coefficient and reduce the target function J a gradient optimization method is employed.
5. This process will be repeat until the residuals would be very low.

The time steps used in the simulations are detailed in the previous section where the transient scale curve was introduced. The time step corresponding to $t = 0$ is included because the first frames of the IR recording were acquired while the hatch was still closed.

3.7 Uncertainty Analysis

Uncertainty analysis is essential for validating experimental results. The term refers to the process of quantifying the impact of individual measurement uncertainties on the final calculated result. The error in a measurement is defined as the difference between its true value and the measured value. While this definition is conceptually clear, it is not practically helpful; in experimental work, every result is affected by various types

of errors, and the true value is almost always unknown. Considering a variable defined as X_i, which is affected by a known uncertainty of δX_i, it is expressed as:

$$X_i = X_i(\text{measured}) \pm \delta X_i$$

where X_i(measured) represents the observation in a single-sample experiment or the mean of a set of N observations in a multiple-sample experiment. The value of δX_i represents 2σ for a single-sample analysis, where σ is the standard deviation of the population of possible measurements from which the single sample X_i was taken. The standard deviation is defined as:

$$\sigma = \sqrt{\frac{1}{N}\sum_{i=1}^{N}(X_i - \bar{X})^2}$$

Errors are typically divided into two categories:

- *Systematic errors*: these errors are unidirectional inaccuracies linked to faulty instrumentation, wrong calibration, or not robust experimental methodologies. They introduce a constant bias that shifts all measurements away from the true value in the same direction. By repeating the experiment, this source of error cannot be reduced. To reduce systematic errors global corrections and recalibration are often required.
- *Random errors*: these are fluctuations caused by uncontrollable environmental variations, structural vibrations, or inherent limitations in human perception. They manifest as a scatter of data points around the mean value; unlike systematic errors, their impact can be effectively minimized and quantified by increasing the number of experimental trials and applying statistical analysis (e.g., standard deviation).

According to Coleman et al. [57], there are two methods for evaluating inaccuracies encountered in experimental studies. One is the Monte Carlo Method (MCM), which assumes different input variable distributions to get an output distributions with the related level of uncertainty. The second is the Taylor Series Method (TSM), which is based on the calculation of the derivatives of the measured physical quantity with respect to the variables that influence the experiment, neglecting higher order terms. The procedures used to evaluate uncertainties arising from the acquisition, HTC computation, and surface modeling processes are extensively detailed in previous works [77, 79, 82].

For this experimental campaign, a sensitivity analysis based on different IR camera angle configurations was performed to assess the sidewall reflection effect on the detected signal. Considering the coordinate system in Figure 3.7, three angles are defined below to detail the configuration adopted for each test:

1. *Roll Angle*: this angle was varied to observe its effect on the lateral wall reflections and consists of a rotation about the *X-axis*;
2. *Pitch Angle*: this angle was kept almost identical throughout all five tests conducted for this analysis and consists of a rotation about the *Y-axis*;
3. *Yaw Angle*: this angle was kept constant to ensure a straight image in the IR camera and consists of a rotation about the *Z-axis*;

Regardless of the different configurations tested, the same region of interest was used for the Nusselt number evaluation in order to have consistent results. In Table 3.13 are reported the details for each test. It was not feasible to perform higher roll angles because of the physical constraints of the IR camera support.

Test	Roll Angle (°)	Pitch Angle (°)
1	0.0	7.0
2	+2.0	8.5
3	+9.0	8.0
4	-3.5	8.0
5	-8.2	8.2

Table 3.13: Angles setup for sensitivity analysis

All five tests were executed under the same fluid-dynamic conditions, specifically $Re = 25000$. The window considered for this analysis was the final one where the flow is thermally fully developed. The geometry chosen was the `Rz_030_00033_sparse` in order to reduce the computational cost of each simulation.

In Figure 3.21, the globally averaged Nusselt number for each test is reported. This value was calculated using the Nusselt spatial distribution within the ROI. The dashed line represents the mean of all five averaged values, and the shaded area represents the standard deviation. It quantifies the uncertainty associated with camera positioning and test repeatability, and assumes a value of $\sigma = 2.38$. Despite the minor variations between the averaged Nusselt numbers, highly precise results can be achieved by utilizing a proper IR camera setup. It was observed that the optimal positioning for the camera, considering all physical and spatial constraints, required a roll angle of zero degrees and a pitch angle ranging from seven to nine degrees.

Figure 3.22 shows the laterally averaged Nusselt number along the streamwise coordinate for all five tests. The dashed colored lines represent the overall Nusselt number, while the markers refer to the local averaged values. The consistent trend shared by all five tests demonstrates excellent reliability and repeatability during the experimental campaign. Moreover, this plot, together with the previous one, highlights the impact of the camera inclination on both the global and local averaged values.

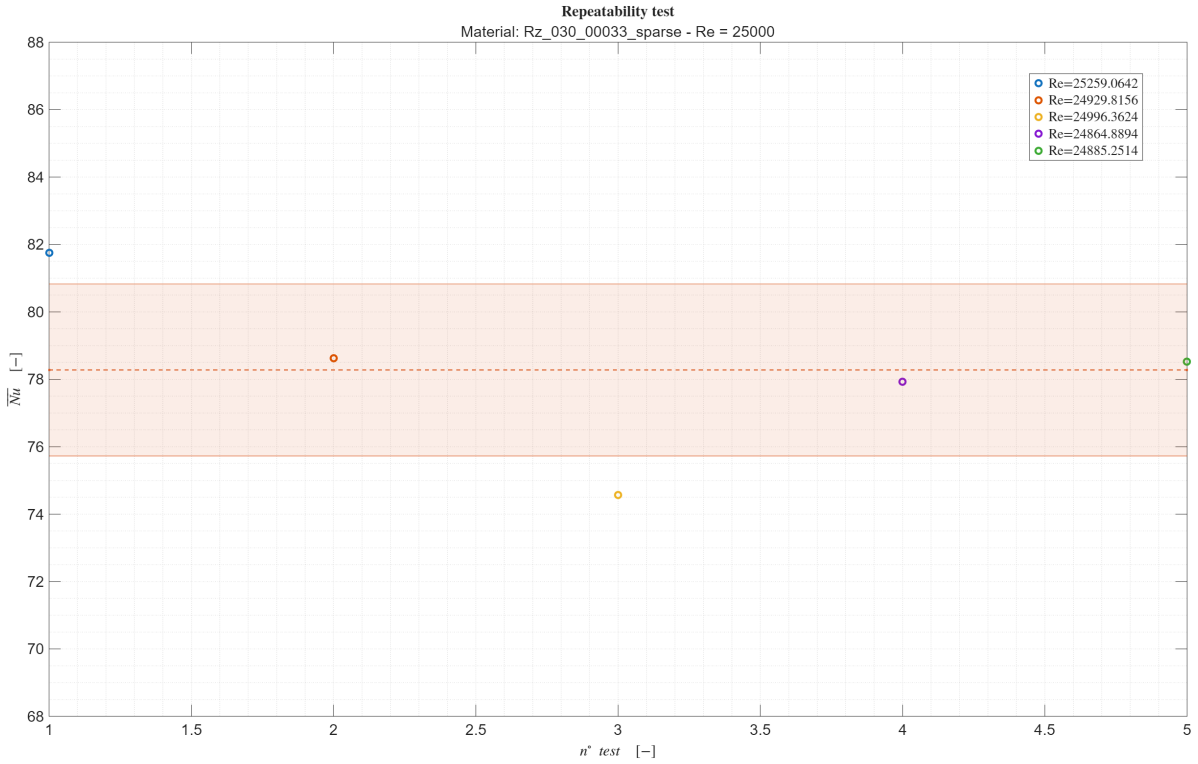


Figure 3.21: Globally avereged Nusselt number for each test

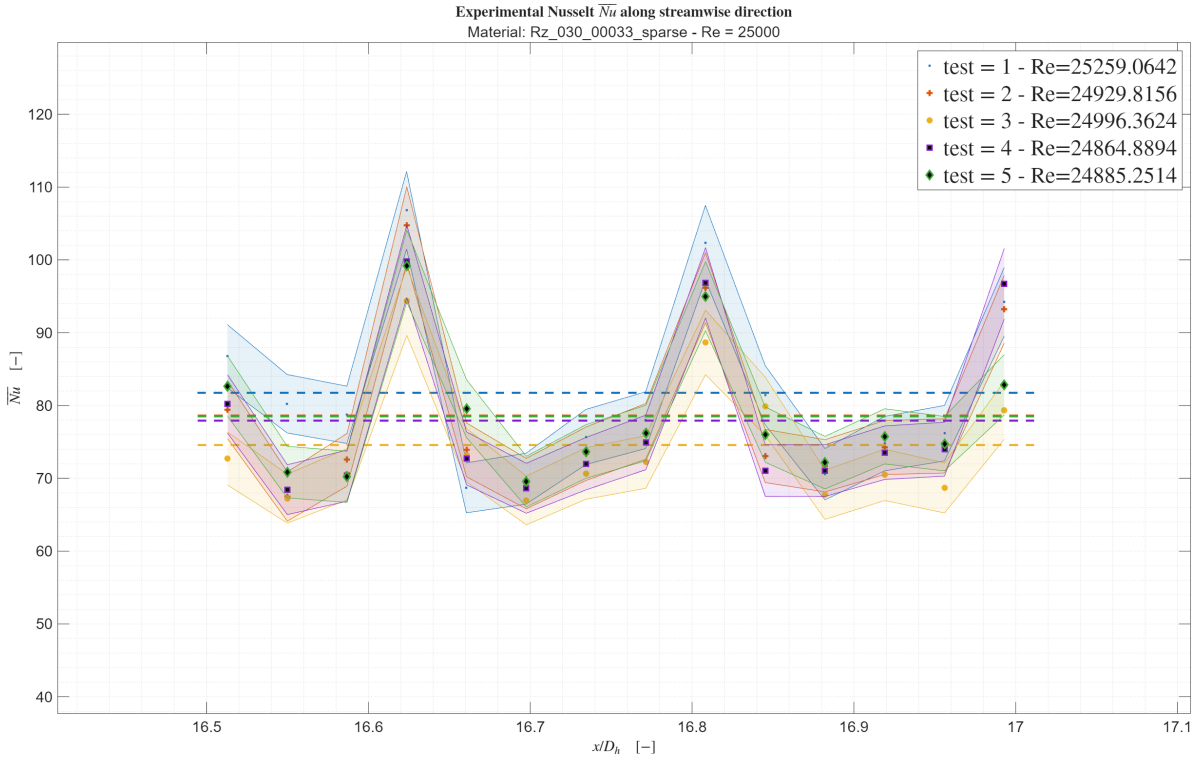
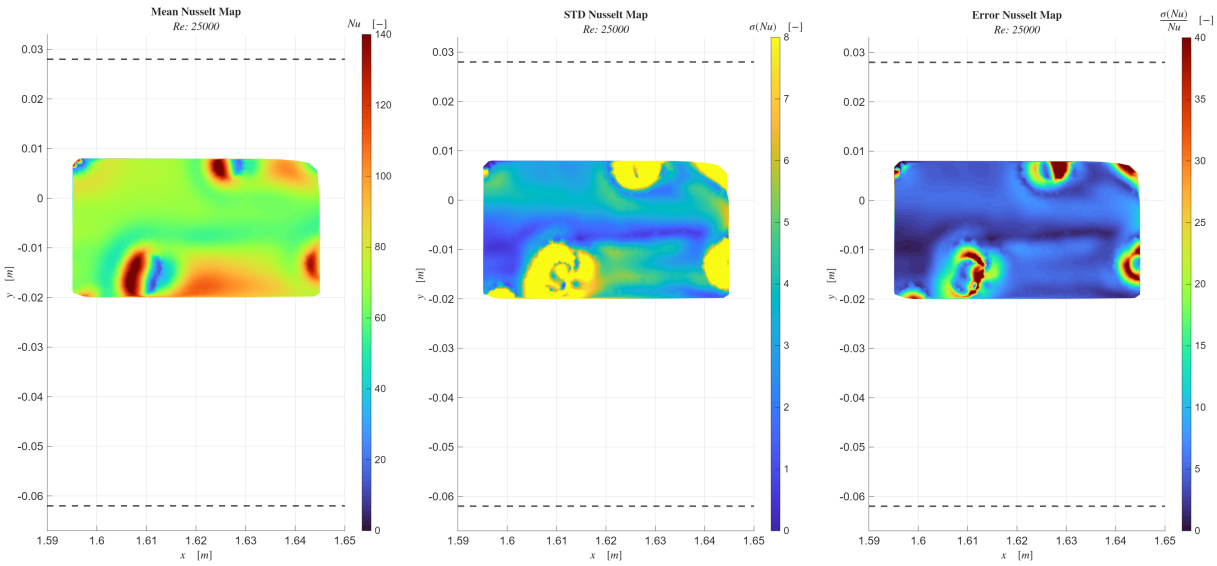


Figure 3.22: Laterally averaged Nusselt number along the streamwise direction for all five tests

Figure 3.23 displays the spatial distribution of the Nusselt number obtained by averaging all five tests. The mean local Nusselt value is reported in Figure 3.23(a), whereas Figure 3.23(b) shows the standard deviation distribution. High local uncertainties are visible, mostly due to the mapping errors. The camera setup affects the rough elements more than the flat areas, as visible in Figure 3.23(c). These results show how regions with high local enhancement are affected by significant errors, even if the test preparation is performed carefully.



(a) (b) (c)

Figure 3.23: (a) Mean local Nusselt number spatial distribution over the five test cases. (b) Standard deviation of the local Nusselt number. (c) Percentage error of the local Nusselt number

Chapter 4

Experimental Results

This chapter presents the results obtained in the SRHT rig. A new validation of the rig was not required since no major modifications were introduced to the experimental setup. Gissi and Jankovskis results were considered in this work, after adapting them to the upgraded version of the rig.

Afterwards, the rough test objects results are presented, focusing on the surface roughness parameters and the Reynolds number effect. Particular attention has been given to the spherical elements density effect on the heat transfer phenomena, as this parameter is studied here for the first time. Thermal boundary layer profiles are reported, accounting for the physical limitations of this measurement and the constraints of the available experimental equipment.

Finally a comparison with PIV and qSSHT rig data is proposed. The PIV comparison provides a fluid-dynamic perspective on the heat transfer mechanisms. The comparison with the qSSHT rig, where real cooling geometries are typically tested, demonstrates that the two different methodologies yield almost identical results.

4.1 Rig Modification

The SRHT rig has not undergone any significant modifications. Improvements were made by Gissi [86], who enabled the full thermal development of the flow by extending the test section and shortening the flow straightener. The corresponding validation process is presented in his work. However, making the test section longer has drastically reduced the available space around the rig, complicating the positioning of the IR camera.

In Jankovskis' work, the bulk temperature computed from the three streamwise thermocouple readings was lower than the expected target of 70 °C. This discrepancy was attributed to the last thermocouple, which was positioned right after the blend where the impinging flow caused significant thermal losses through the wall. A new temperature sensor was added upstream of the blend, as shown in Figure 4.1.

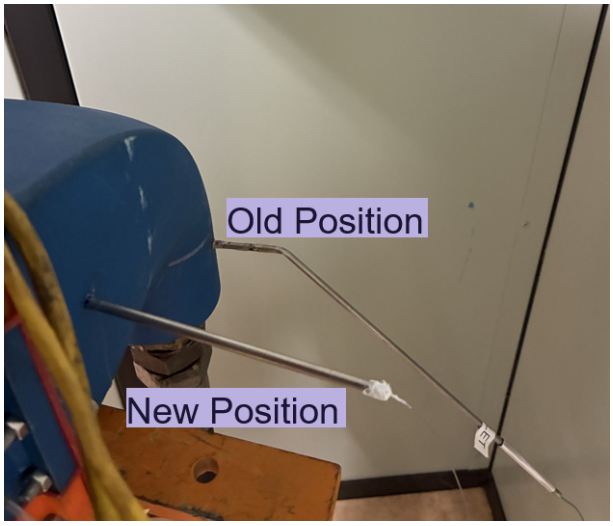


Figure 4.1: Modification of the final thermocouple position

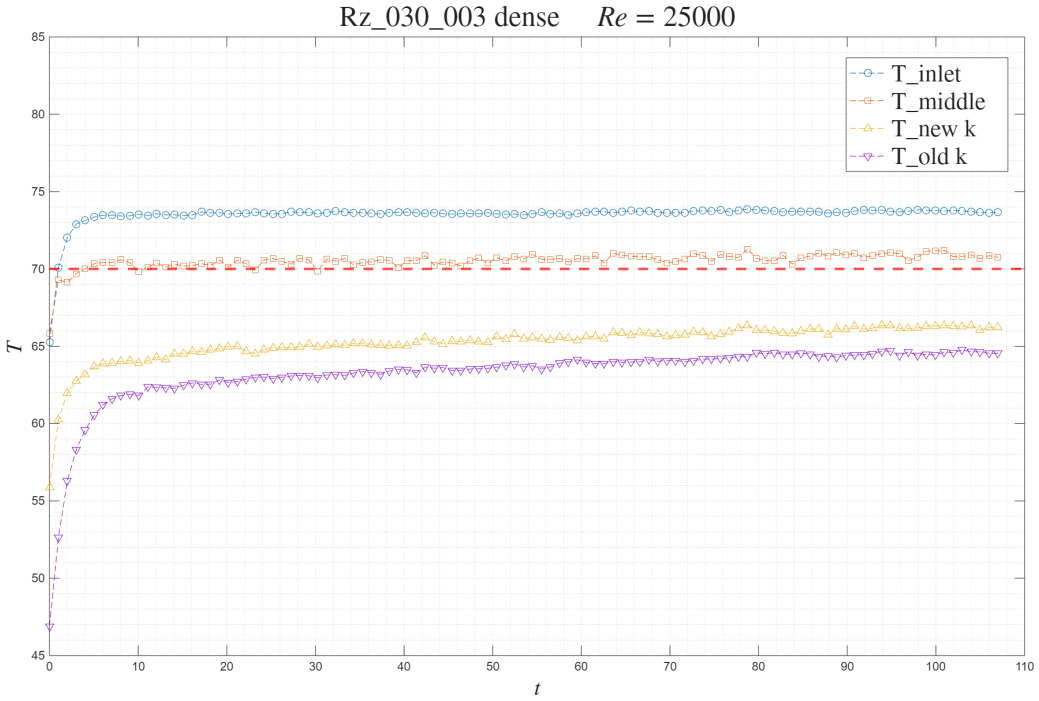


Figure 4.2: Transient thermocouple's temperature readings

A test was conducted in order to evaluate the temperature difference between these last two thermocouples. As illustrated in Figure 4.2 a difference of almost 3 °C is evident between the old sensor and the new one positioned upstream of the blend. Additionally, the experimental inlet temperature, T_{inlet}, is usually higher than the target temperature. This behavior is attributed both to thermal conduction through the hatch wall, since the first thermocouple is located only a few centimeters away, and to the entry effect detailed in the following section.

4.2 Nusselt Results

Several plots are presented to show either the local and the global HTC distribution. All the results are based on the dimensionless Nu number defined as:

$$Nu = \frac{D_h h}{k_{air}}$$

Considering the same coordinates system used in Figure 3.7, at a specific streamwise position x_i, the lateral average of the Nusselt number is determined by averaging across all discrete lateral locations y_j:

$$\overline{Nu}_i = \frac{1}{N} \sum_{j=1}^{N} Nu(x_i, y_j)$$

Subsequently, the global average Nusselt number within the designated region of interest is evalueted as:

$$\overline{Nu} = \frac{1}{M} \sum_{i=1}^{M} \overline{Nu}_i$$

Instead of the elliptical ROI, this global average value is calculated within a smaller rectangular region of interest centered between the four crosses, thereby minimizing wall effects.

The laterally averaged Nusselt number $\overline{Nu}_i$ is plotted against the non-dimensional streamwise coordinate x/D_h in Figures 4.4 and 4.5, while Figure 4.3 displays the global average Nusselt number along the streamwise direction. Due to time constraints, it was not possible to test all the windows of the rig. The common trend for all rough models is a monotonic decrease along the streamwise direction until a plateau is reached, which ensures fully developed thermal conditions. Consequently, the last two locations turn out to be the most relevant results for any subsequent comparison.

Compared to the smooth model results reported in Gissi's work, the main difference lies in the presence of sharp oscillations and spikes. The random SR distribution generates a non-uniform HTC distribution. Consequently, since the markers in Figure 4.4 represent the $\overline{Nu}_i$ values and the dashed lines refer to the global average $\overline{Nu}$, multiple physical mechanisms contribute to this oscillatory behavior. These include flow separation, vortex shedding behind the roughness elements, and fluid interaction with the bounding walls, as discussed in detail within the PIV comparison section.

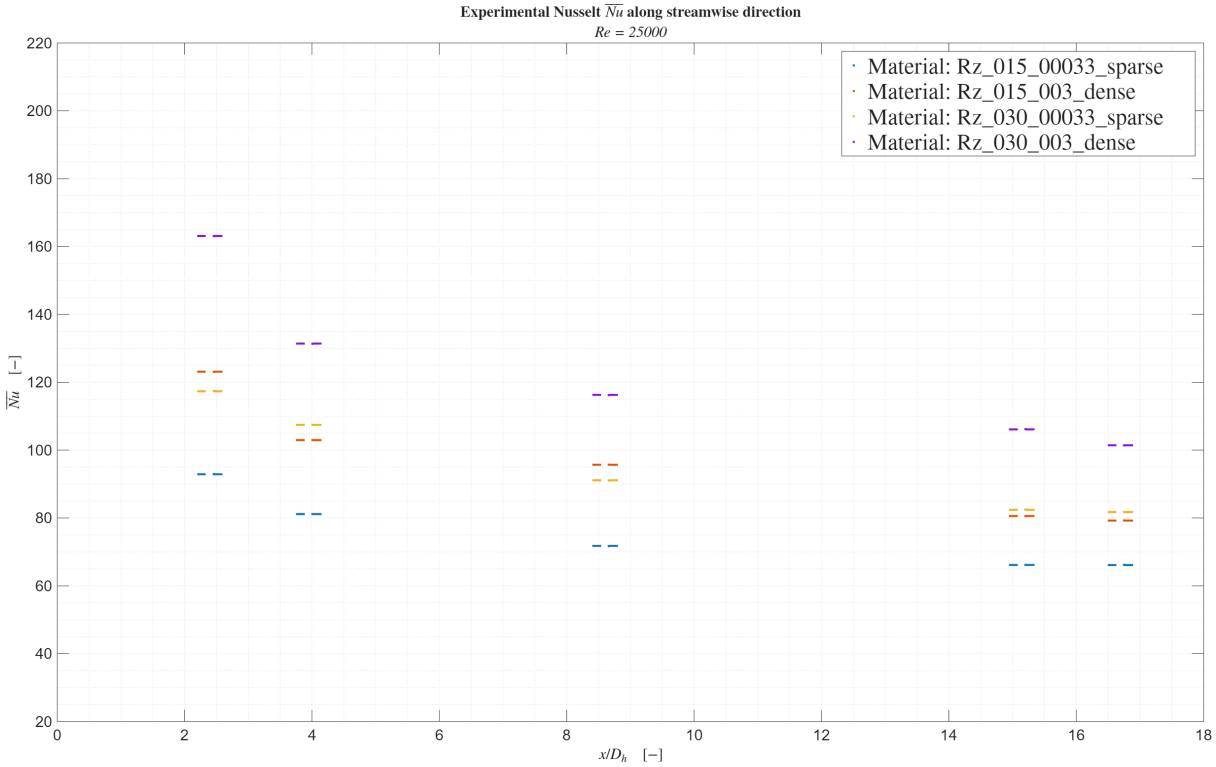


Figure 4.3: Globally averaged Nu along streamwise direction $Re = 25000$

The Reynolds number effect is highlighted when comparing Figure 4.4 and Figure 4.5. SR parameters also significantly influence the heat transfer behavior. Increasing the size of the roughness elements increases the wetted area, thereby enhancing the Nusselt number (Nu). A similar trend is observed for the spatial density of the spheres, with minor distinct variations that are discussed in detail within the density effect section. The enhanced heat transfer can be primarily attributed to the following mechanisms:

1. *Entry Region Effect*: the highest Nu values are registered within the first two windows of the test section. In this region, the fluid experiences a preheating effect upstream, accumulating thermal energy before entering the channel. Additionally, a conduction contribution is present due to thermal conductivity through the hatch wall.

2. *Reynolds Number Effect*: this effect aligns perfectly with existing literature corre-

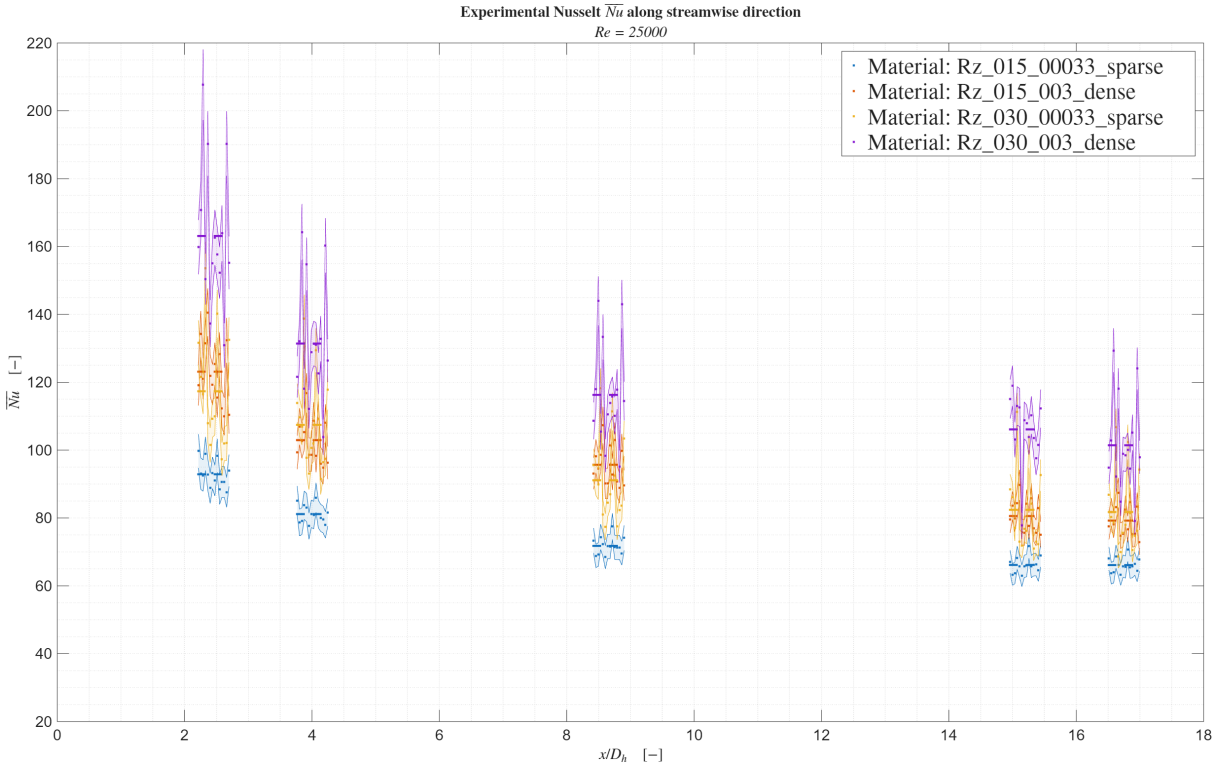


Figure 4.4: Globally and laterally averaged Nu along streamwise direction $Re = 25000$

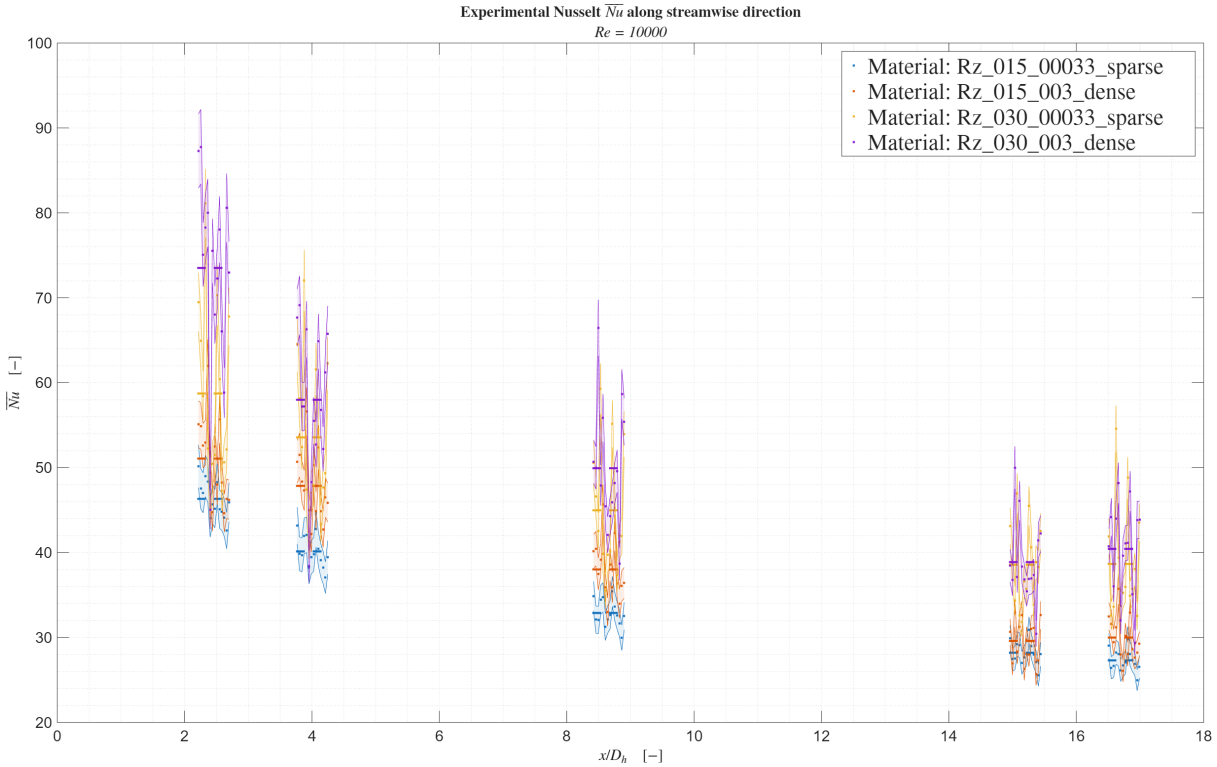


Figure 4.5: Globally and laterally averaged Nu along streamwise direction $Re = 10000$

lations where a direct proportionality is experienced between the Reynolds and Nusselt numbers.

3. *Surface Roughness Effect*: the surface roughness reduces the entrance length required for thermal development. The roughness parameters considered in this work demonstrate a positive contribution to the HTC distribution. R_z results to be a key driver of thermal performance, establishing a robust statement with Jankovskis' work. Furthermore, while initial findings are promising, the spatial density of the spheres warrants deeper investigation; it contributes to a substantial increase in Nu, particularly at higher Reynolds numbers. Simultaneously increasing both the density and size of the spheres introduces pronounced oscillations in the laterally averaged Nusselt number, driven by alternating zones of high and low heat transfer.

Focusing on the last two windows of the plot in Figure 4.4, the geometry with the highest averaged Nu is `Rz_030_003_dense`, due to its larger sphere size and higher spatial density. This demonstrates how these two SR parameters enhance the heat transfer mechanism. However, further studies regarding the fluid-dynamic impact of these geometries are required to assess the associated pressure losses in real cooling channels. On the other hand, the geometry with the lowest heat transfer performance is `Rz_015_00033_sparse` due to the smaller sphere size and density distribution.

It looks interesting to note how much overlap there is between the laterally averaged points of `Rz_015_003_dense` and `Rz_030_00033_sparse`. The former has a smaller R_z but higher density, whereas the latter is completely the opposite. This shows how using different geometric configurations can lead to similar results. All three of these effects can be better observed in the *Experimental Nusselt Map* in Figure 4.6. The dashed black lines represent the physical boundaries of the test section. In these plots, all four rough models are reported and their Nu spatial distribution along the longitudinal coordinate is presented. From these plots, the *Entry region Effect* is visible in the first two windows, where a higher Nusselt distribution is shown characterized by dark red contours. This behavior is not as clearly visible in the last two windows, where the fully developed thermal condition has already been reached.

A closer look at the last window is necessary to compare all rough models tested and better understand the HTC spatial distribution induced by the roughness. This can be done using the plot reported in Figure 4.8. The spatial density of the rough elements plays a key role in the Nusselt distribution. The main differences between the four test samples are highlighted. For each tested geometry, the frontal area of the spheres is directly exposed to the upcoming flow, generating a high Nu region due to flow impingement. The extent of this area is proportional to the sphere size, representing a typical behavior for upscaled roughness geometries. The two sparse configurations share a common fluid-dynamic feature: once the flow impacts the spheres, a recirculation zone is formed behind them. This wake region is more pronounced in the `Rz_030_00033_sparse` geometry due to the larger sphere size. The flow has sufficient space downstream of the recirculation zone to reattach and re-accelerate.

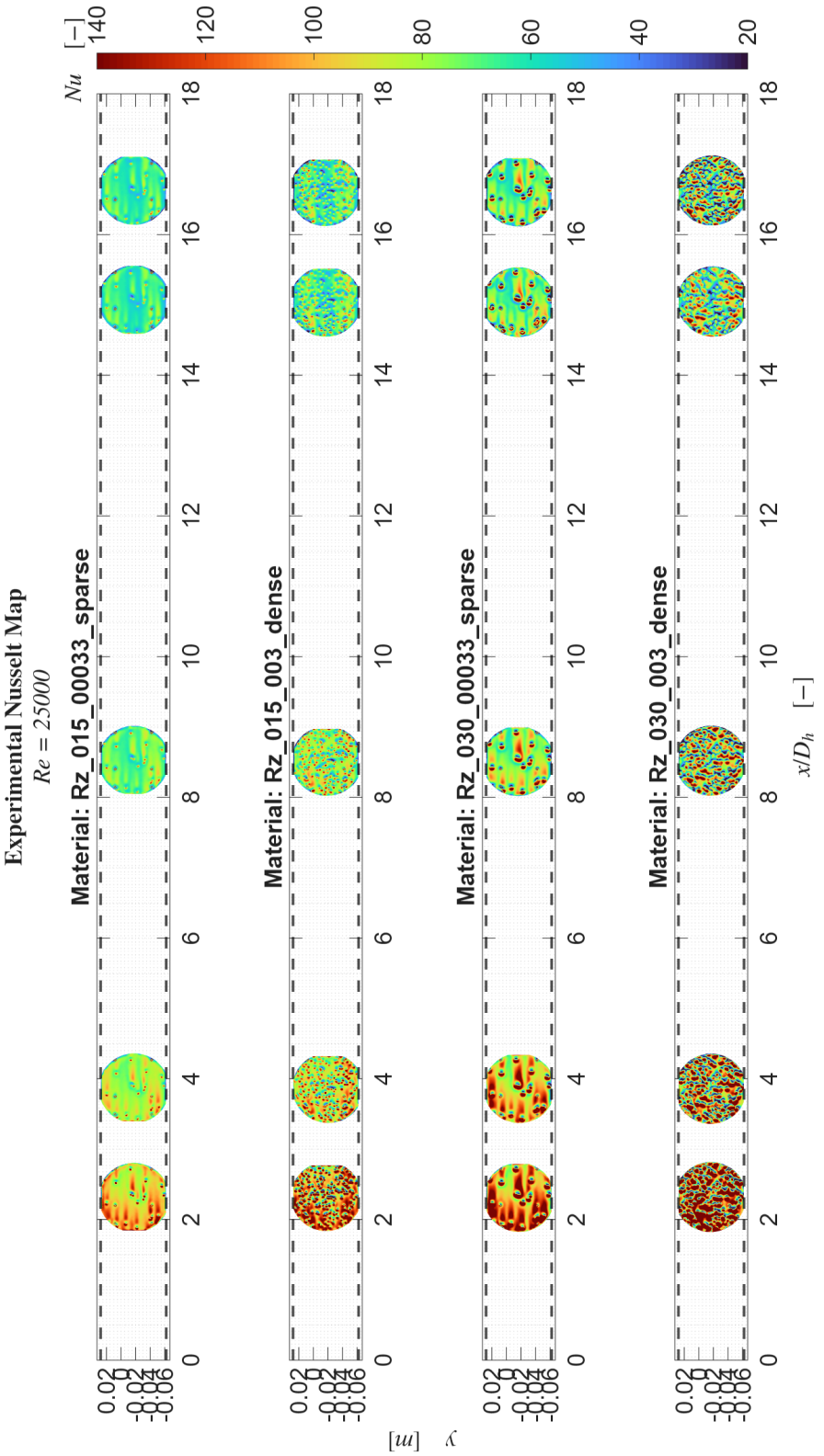


Figure 4.6: Experimental Nusselt Map $Re = 25000$

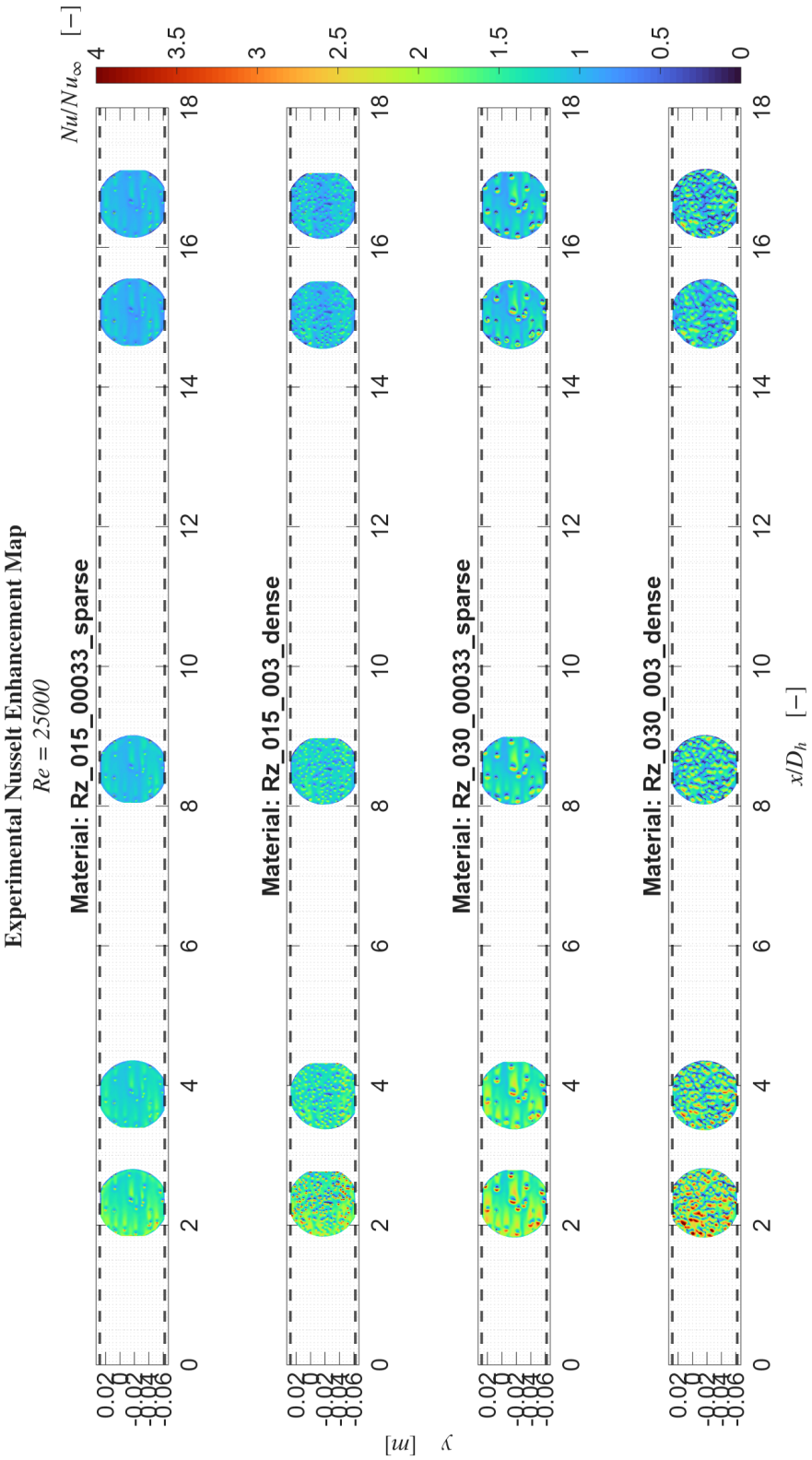


Figure 4.7: Experimental Nusselt Enhancement Map $Re = 25000$

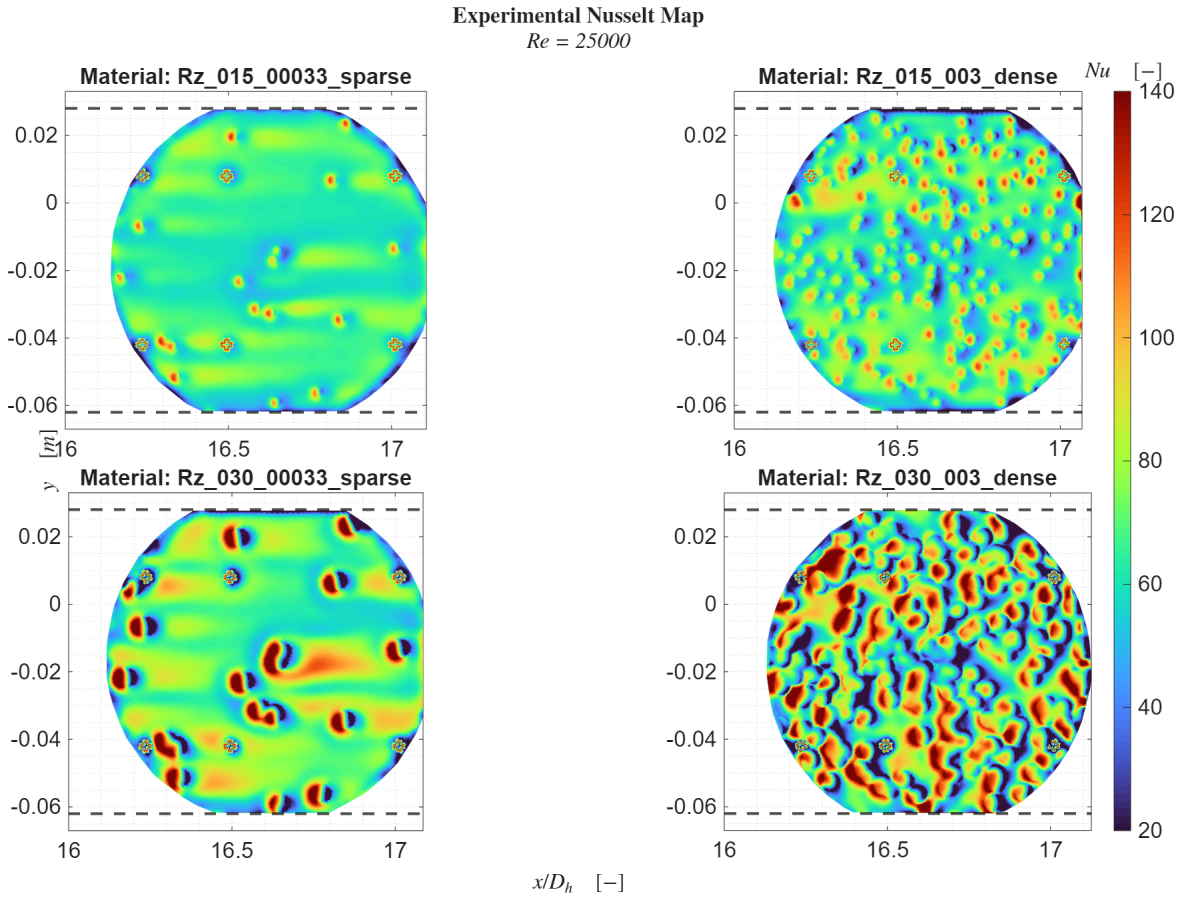
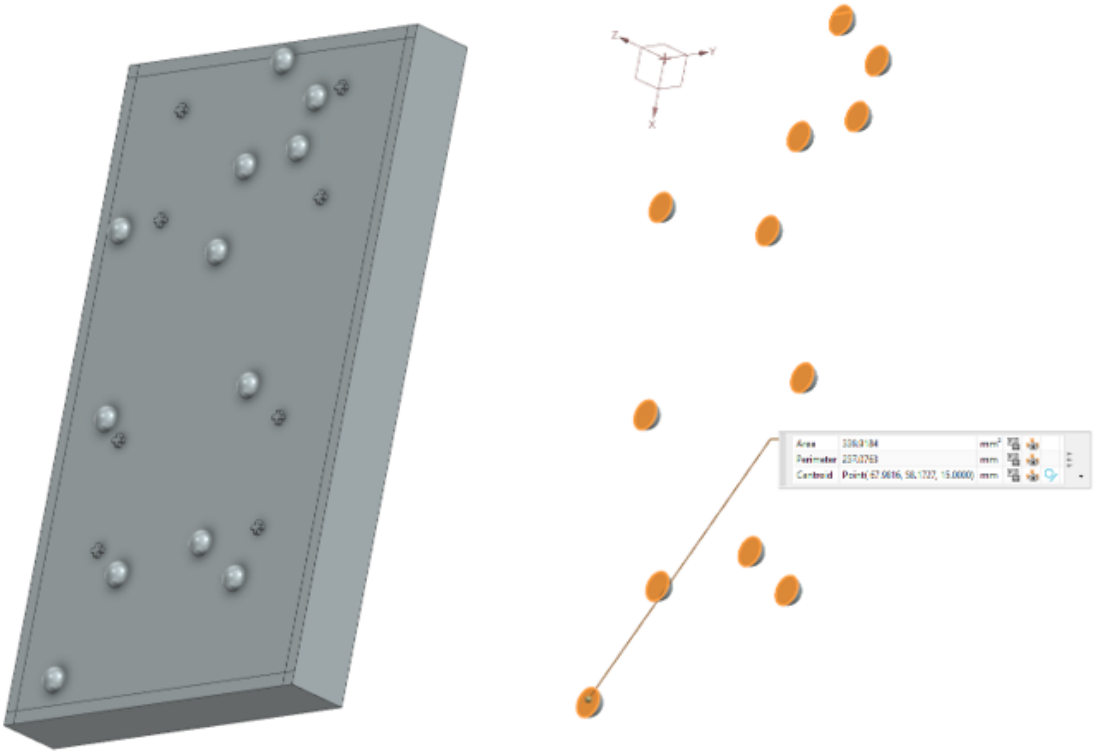


Figure 4.8: Experimental Nusselt Map comparison between the four rough models at $Re = 25000$ and in the last window

This is demonstrated by the longer Nu streaks behind the spheres. Conversely, this behaviour does not happen for the dense geometries due to the limited available flat area between the spherical elements. For these geometries, the recirculation zones are widespread, and the flow remains blocked between elements without the possibility of reattachment. However, even though the available flat area is reduced, the high number of spheres provides a sufficient surface area enhancement to achieve very high Nu values, as detailed in the next section.

4.3 Density Effect



(a) CAD model (b) Plan area of the spheres

Figure 4.9: Spatial density calculation from the CAD model

This section outlines the impact of the sphere density on the HTC distribution. In this thesis work, two different density configurations for $R_z = 1.5\,\text{mm}$ and $R_z = 3\,\text{mm}$ were tested. For a more robust comparison, the geometries tested by Jankovskis were re-evaluated to account for the small changes of the rig, presented in the beginning of this chapter. Two different plots are presented to explain the effect of the spatial density: first, the $Nu - Re$ trend is provided, followed by the $Nu - A_s/A_{tot}$ plot. The contribution of the R_z is analyzed separately, before being integrated at the end of this section for a global comparison. In Table 4.1 are reported the values of the SR

parameters considered for this comparison. Figure 4.9 shows how the plan area of the spherical elements is calculated. The total flat area of the geometries, assumed as smooth flat surfaces, was computed by multiplying the length by the width reported in Table 3.1. The Nu values reported in these plots are evaluated by considering the square ROI formed by the four crosses visible within the IR window. Furthermore, a global average value for the Nu was adopted considering windows nine and ten. Investigating the density effect implies analyzing the impact of the *plan solidity* λ_p, as defined in Chapter 2.

Geometry	R_z **[mm]**	A_s/A_{tot} [-]
Rz_015_00033_sparse	1.5	0.0220
Rz_015_001	1.5	0.0642
Rz_015_003_dense	1.5	0.1813
Rz_030_00033_sparse	3.0	0.0839
Rz_030_001	3.0	0.2362
Rz_030_003_dense	3.0	0.5542

Table 4.1: SR parameters of the investigated roughness models

The $Nu - Re$ plot displays three curves, each corresponding to one of the three available density configurations. For each curve, the four markers represent the specific Reynolds numbers tested. As the Re increases, the three curves position themselves in order of increasing density: the lowest curve refers to the lowest density configuration, whereas the highest curve represents the highest density geometry.

A slight overlap is visible at $Re = 10000$ between the three curves because of experimental uncertainties and the specific fluid-dynamic condition. For $R_z = 1.5mm$ lower Nu values are registered compared with those for $R_z = 3mm$. However, the same trend is clearly visible in both Figures 4.10 and 4.11. Interestingly, at $Re = 10000$, in Figure 4.11, the overlap is more pronounced. At $Re = 10000$, the larger available flat area in the sparse geometries seems to contribute to the higher HTC distribution than the increased number of spheres. This might happen because, at such a low Reynolds number, the flow does not have the space and time required for boundary layer reattachment. To confirm this hypothesis, further analyses have to be carried out, focusing on intermediate density and R_z configurtions. Developing CFD models could help to gain deeper insights into the flow behavior under this specific condition.

Figures 4.12 and 4.13 display the $Nu - A_s/A_{tot}$ plots, which also outline the effect of the Reynolds number for the two different R_z values. Four curves are reported, each corresponding to one of the four Re investigated. For each curve, lines connect the three markers that represent the three different density configurations. The higher the

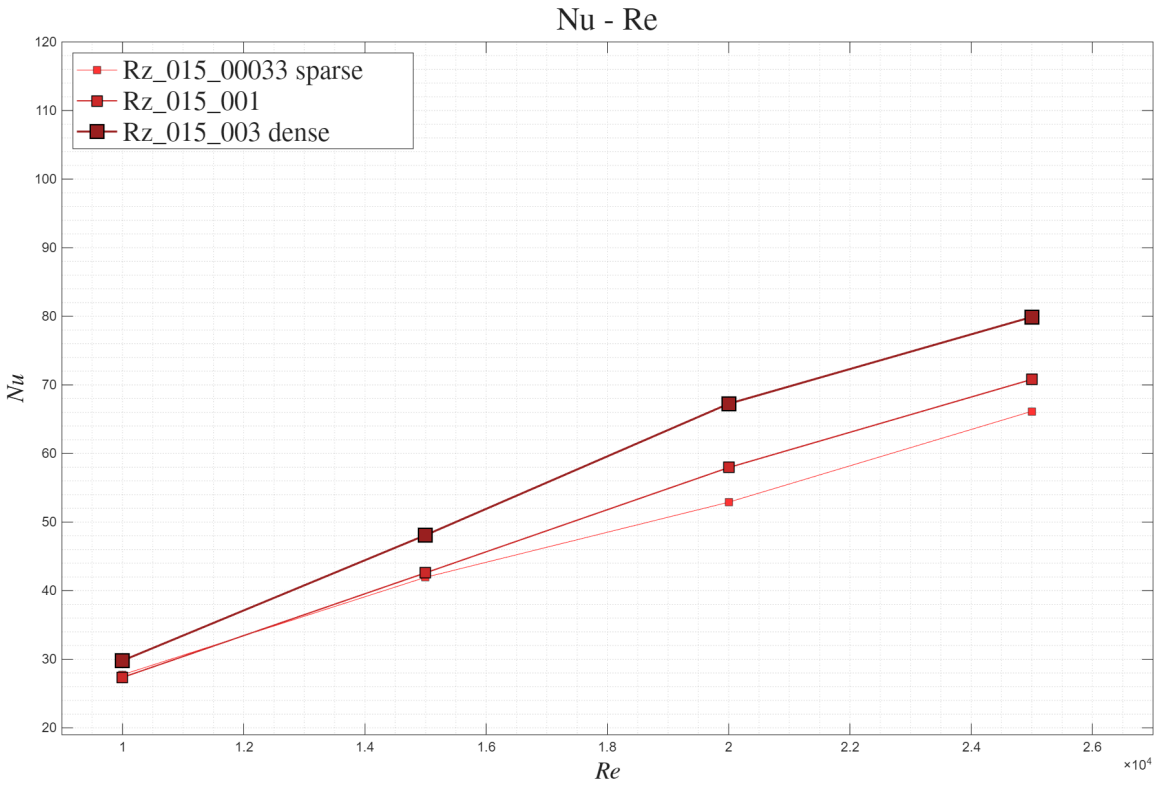


Figure 4.10: Density Effect on the $Nu - Re$ plot for Rz_{015}

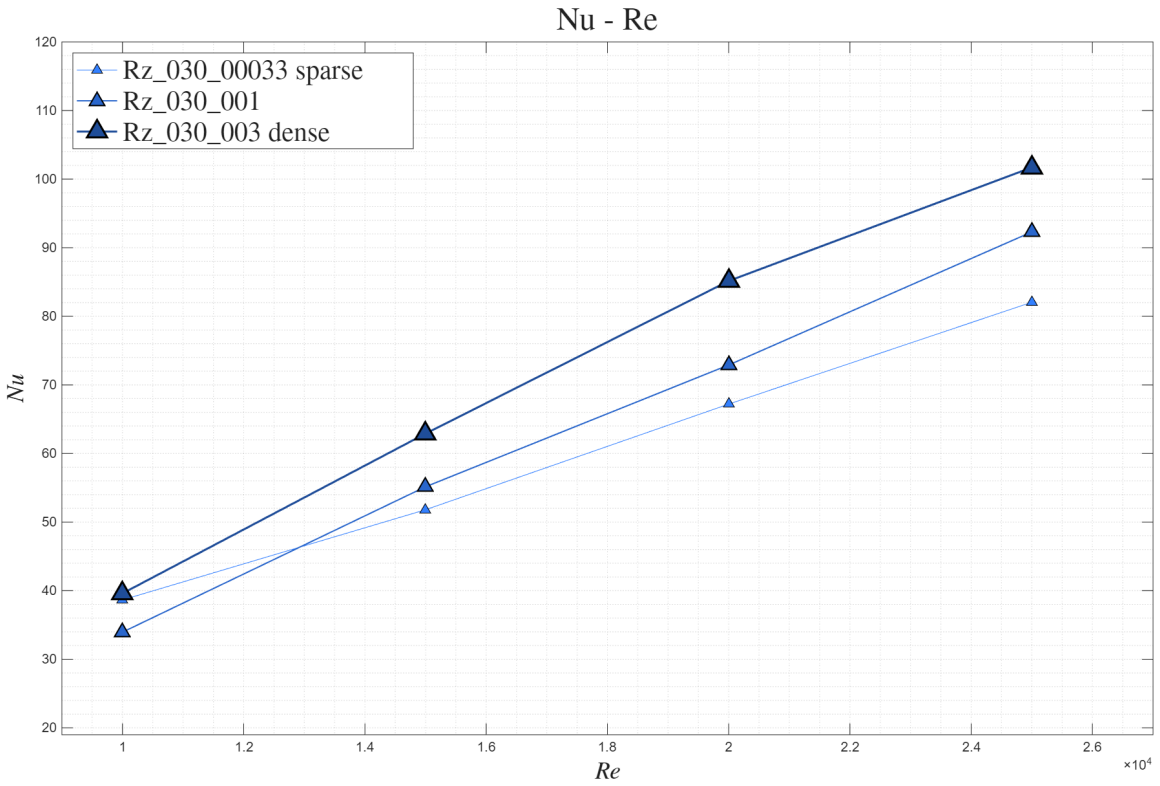


Figure 4.11: Density Effect on the $Nu - Re$ plot for Rz_{030}

Re, the higher the resulting HTC distribution. For a given flow condition, increasing the area ratio A_s/A_{tot} implies that the Nu increases as well. At $Re = 10000$ this trend is not replicated for the aforementioned reasons. The difference in these two plots is the overall higher Nu values for $R_z = 3mm$. Presenting the results for each geometry individually allows for a better comprehension of the phenomena.

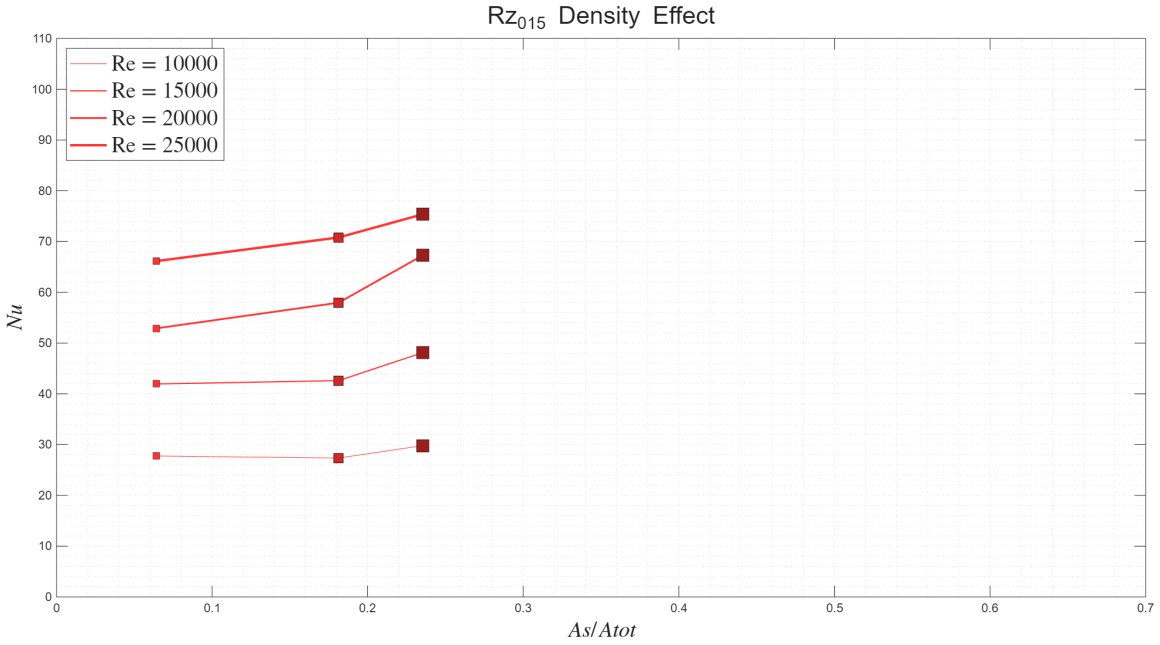


Figure 4.12: Reynolds Effect on the $Nu - A_s/A_{tot}$ plot for Rz_{015}

To conclude this section, a comprehensive comparison of all the rough models tested so far for this parametric study is presented. Figures 4.14 and 4.15 displays these results. Both plots include the smooth geometry as a baseline reference, alongside the $R_z = 6$ mm configuration, which was re-evaluated to account for the modified thermocouple position. It is evident how, for a given Re number, a specific HTC (Nu) averaged value can be achieved by different geometries, as shown in the overlap between dark red squares and light blue triangles in Figure 4.14. Rz_060_001 is still the rough test object with the higher values of averaged Nu. Furthermore, it induces larger oscillations than every other geometries in the laterally avereged Nu plot displayed in Figure 4.15.

4.4 Thermal Boundary Layer

Thermal boundary layer profiles are displayed within this section, highlighting the limitations and uncertainties of these results. In Figure 4.16 is shown the thermal boundary layer rake built by Gissi, who first implemented this instrumentation in the SRHT rig. It consists of five k-type thermocouples stacked vertically, using stainless steel tubes to ensure the perpendicular alignment of each probe. The limitations of this device and the uncertainties of the thermal boundary layer profiles are listed below:

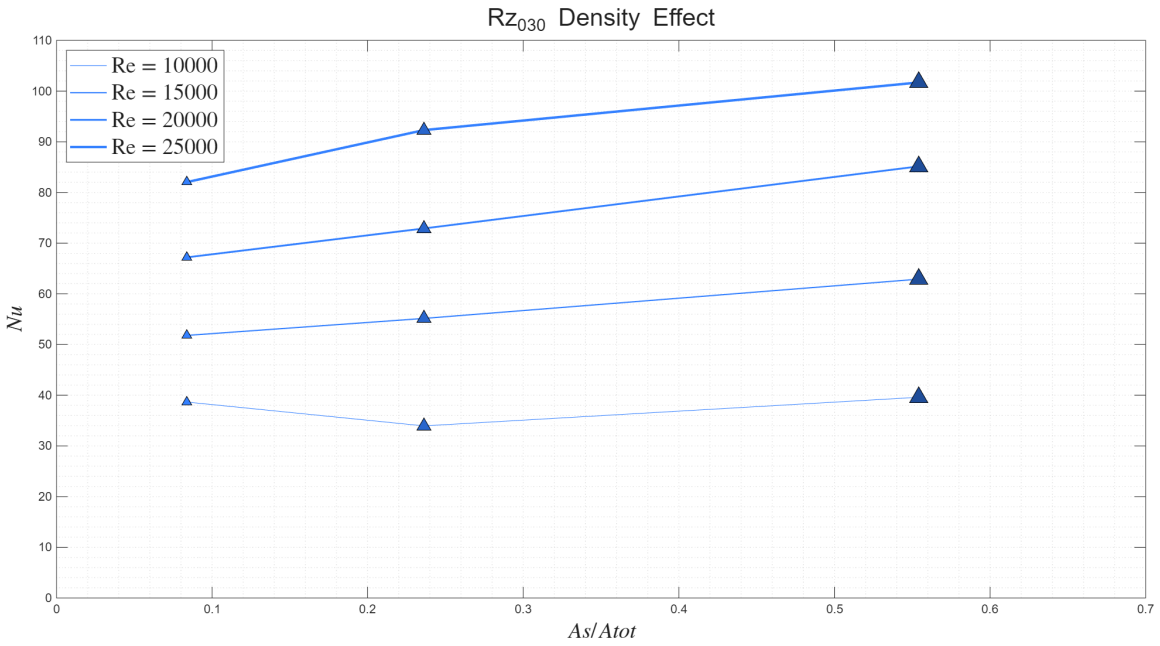


Figure 4.13: Reynolds Effect on the $Nu - A_s/A_{tot}$ plot for Rz_{030}

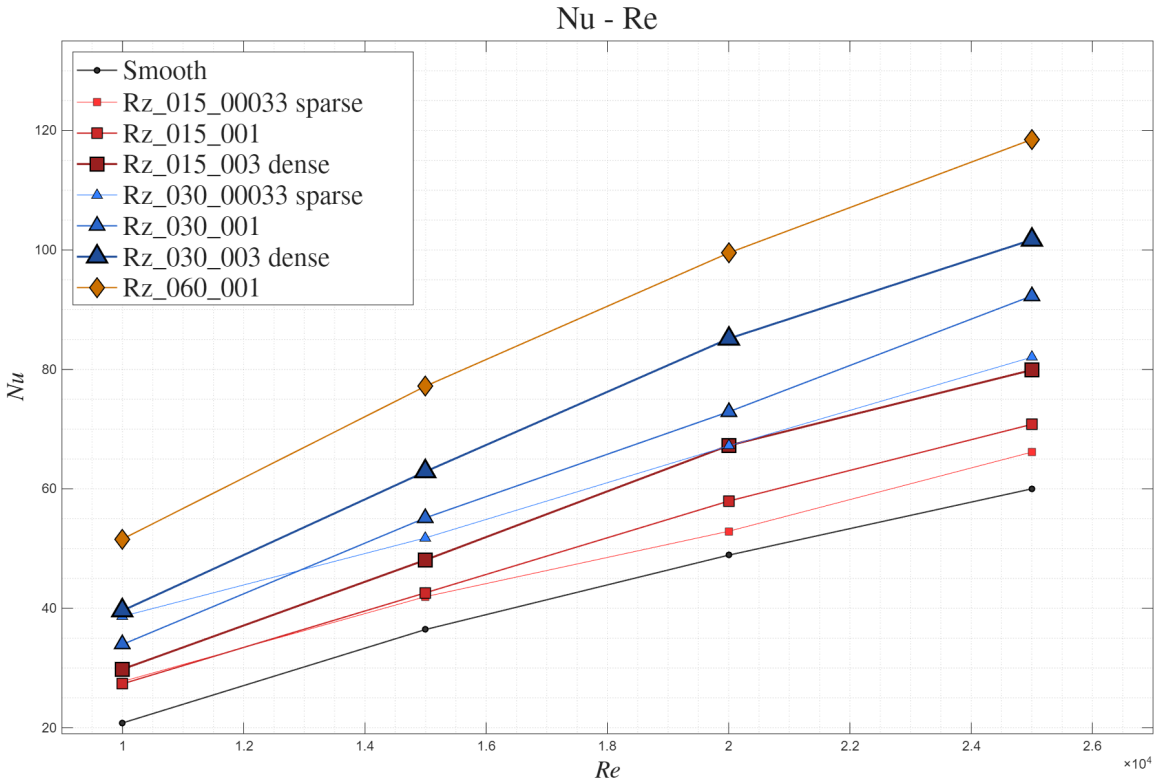


Figure 4.14: $Nu - Re$ plot with all the parametric geometries tested in the SRHT rig

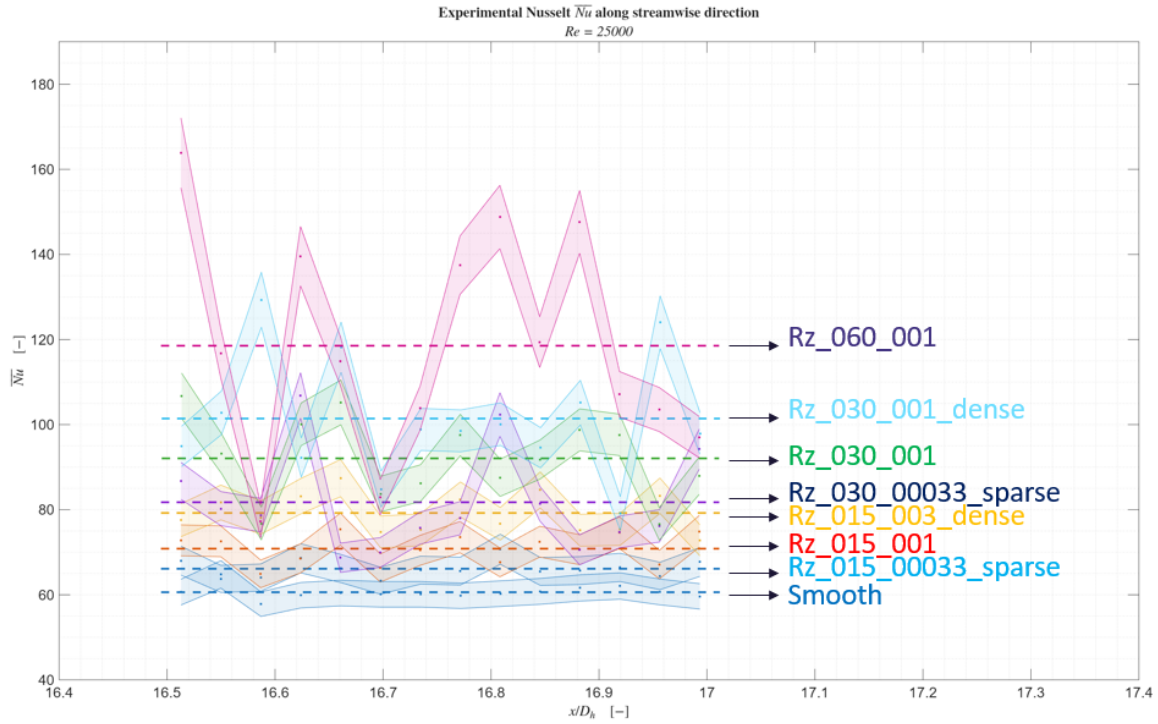


Figure 4.15: Geometry Comparison

- The SRHT was not designed for thermal boundary layer measurements since it is impossible to see the exact location of the probe and the distance from the wall from the outside of the rig.
- The rake is integrated with one of the lids used to seal the circular openings of the test section. For this reason, the alignment of the five thermocouples with respect to the oncoming flow is not always guaranteed.
- The rake is very fragile and the thermocouples tend to break easily.
- The rake cannot be moved along the normal coordinate, so it is impossible to collect more than five temperature points.
- The probe closest to the wall was damaged and, due to time constraints, it was not feasible to replace it. Only four points were used for temperature profiles.

Some temperature profiles lie above the thermal log-layer curve. Measurement errors are relevant in these cases.

To express the $\beta(Pr)$ function, the correlation proposed by Kader and Yaglom [11] was used. The choice of the correlation for $\beta(Pr)$ is crucial but, at the same time, introduces a degree of arbitrariness, since there are many formulations available in the literature. Additionally, while plotting the thermal boundary layer profile, the friction velocity u_τ used to nondimensionalize the temperature profile was obtained, as a first approximation, using the friction factor from the Moody diagram. As a measure of the

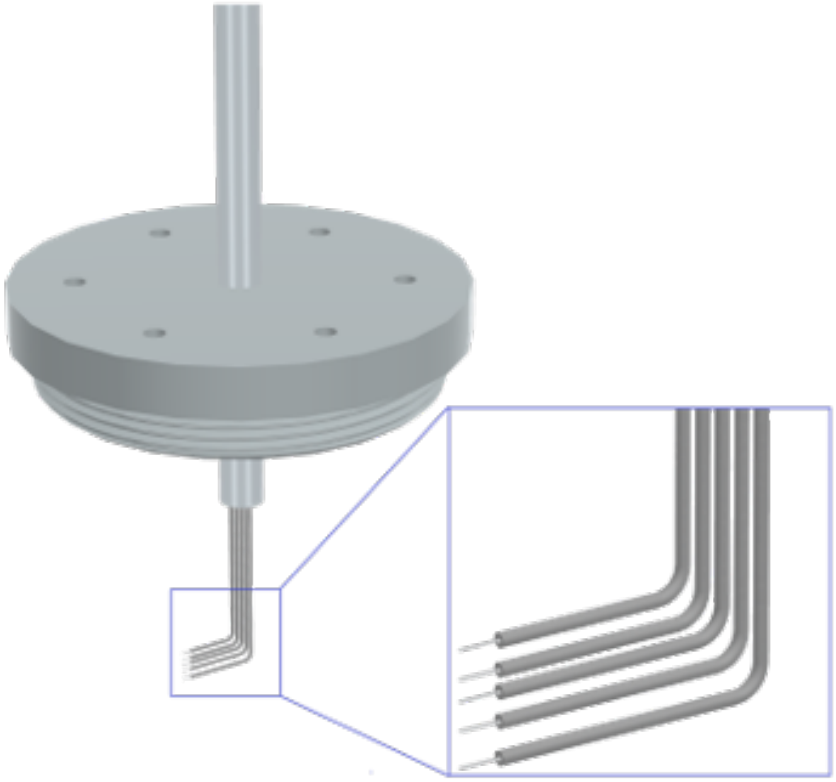


Figure 4.16: Thermal boundary layer rake

relative roughness, the ratio R_z/D_h was used. For a more accurate evaluation of the friction velocity, a parallel study with the PIV rig should be carried out to assess the Fanning coefficient C_f for the specific rough test object.

Despite the experimental limitations, good results were obtained and are shown in Figures 4.17 and 4.18. All the temperature profiles have the same slop of the log-layer curve. A downshift in the temperature profiles with the increasing of the density is visible, in both thermal boundary layer plots.

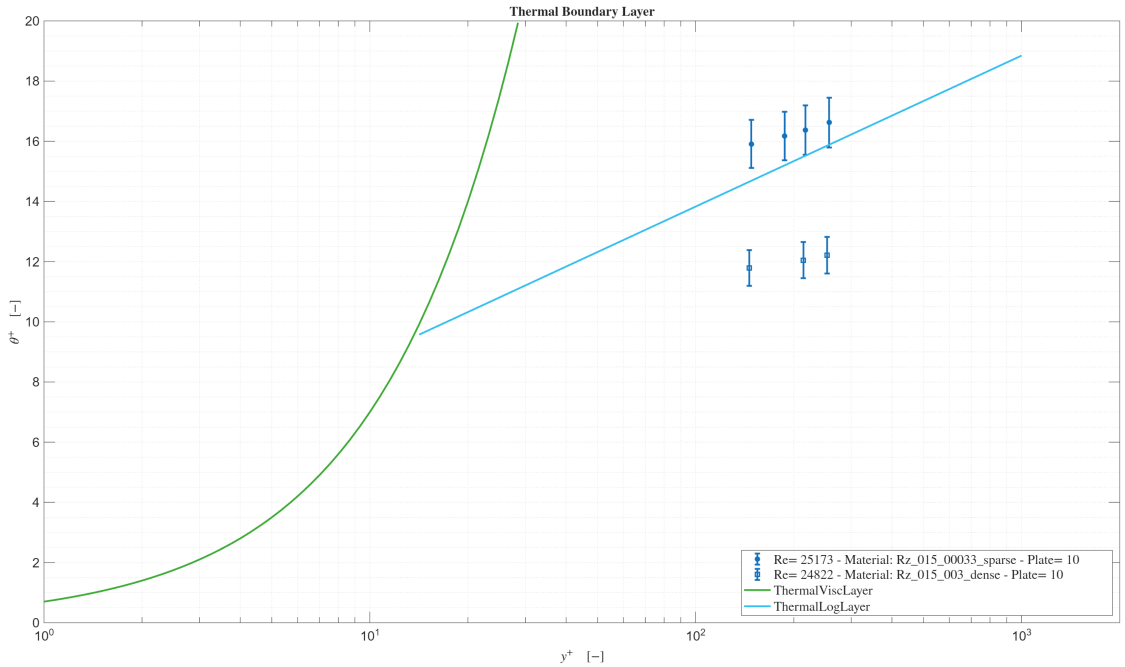


Figure 4.17: Thermal boundary layer profile for Rz_{015}

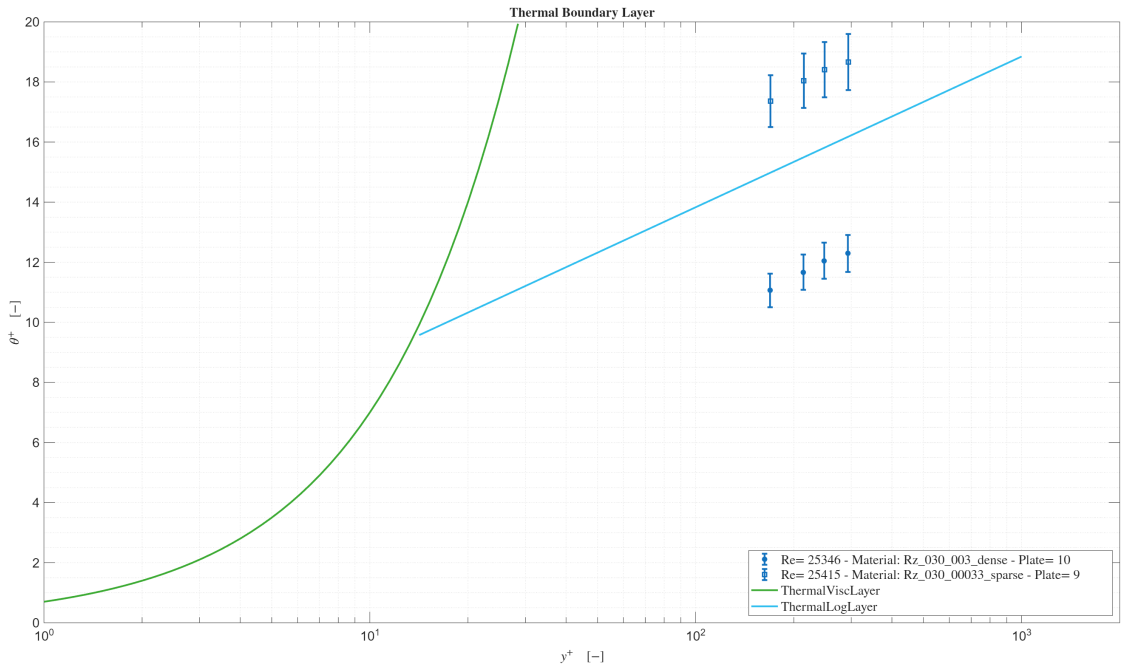


Figure 4.18: Thermal boundary layer profile for Rz_{030}

4.5 PIV Comparison

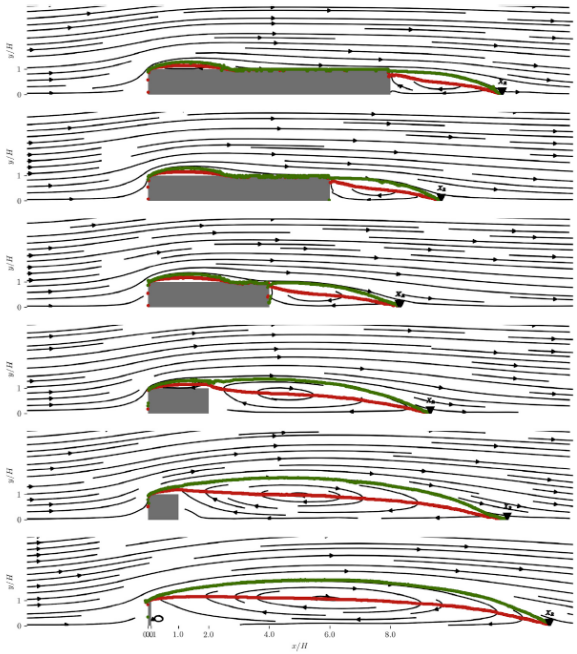


Figure 4.19: Mean flow streamlines obtained from PIV data that depicts the organization of the various recirculation regions around ribs of varying length [59]

The PIV methodology is a fluid-dynamic measurement technique used to visualize the velocity field around a body. It uses small particles mixed into the flow, a laser to illuminate these particles, and a camera to acquire the particle images at a very high frequency. Comparing PIV methodology with the experimental Nu map helps explain the non-homogeneous HTC distribution. Additionally, it leads to a better undertanding of heat transfer mechanisms from a fluid-dynamic point of view. Gissi was the first to propose this comparison between SRHT and PIV rig since in these rigs are investigated the same geometries. Brogliato and Marìn hypothesized that zones downstream of roughness elements could lead to Nusselt number reductions due to vortex formation and recirculation zones [82, 84, 86]. High roughness and high frontal area produce high Nu value as detailed by Gissi. Due to modifications in the PIV rig, not all geometries could be compared with the SRHT results. The primary limitation of the PIV data arises from the obstacles in front of the camera, which prevent the analysis of highly dense configurations. The fluid dynamic condition chosen is $Re = 25000$.

It is well established from previous works which flow structures govern surface roughness models; for that reason, considering the PIV limitations, another approach was followed to present a new comparison. According to the work by Van Der Kindere [59], it was demonstrated how different square element configurations can affect the wake shape downstream of these roughness elements in terms of *reattachment length*. In Van Der Kindere work several configurations referred to as ribs were studied and reported in Figure 4.19.

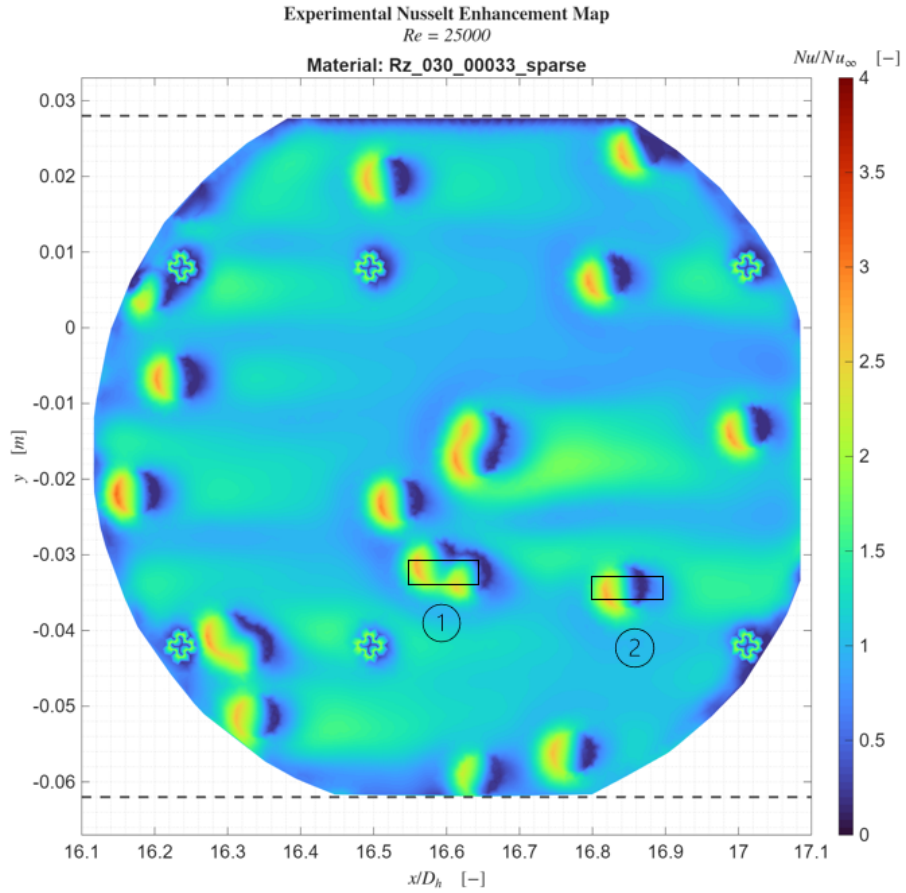
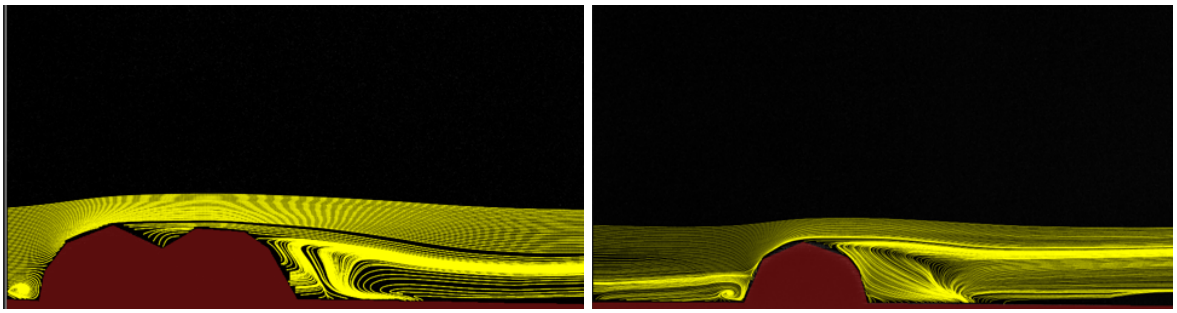


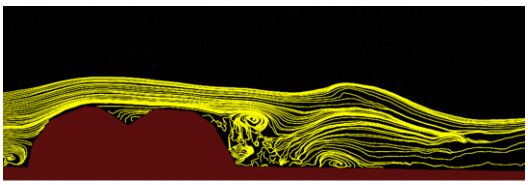
Figure 4.20: Surface spots analyzed for the PIV comparison



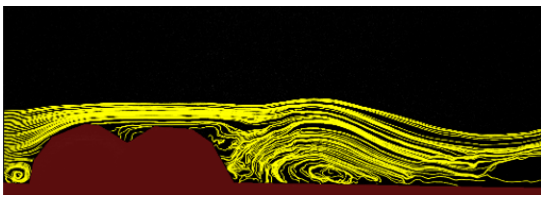
(a) Spot 1 (b) Spot 2

Figure 4.21: Mean Velocity Field from PIV results [92]

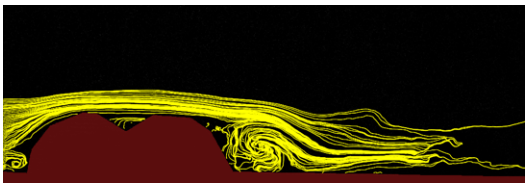
The spheres distributed on the flat surface of the test objects can be assimilated to the geometries studied by Van Der Kindere. Only two configurations were found to be similar to those shown in Figure 4.19; specifically corresponding to Spot 1 and Spot 2 of the Rz_030_00033_sparse in Figure 4.20. In both Region 1 and 2, a small confined vortex forms before the frontal face of the sphere due to the sharp 90° shape variation. Flow impinges on the windward slope, and recirculation forms in the wake region behind the roughness elements [87]. From the mean velocity field, reported in Figure 4.21, large recirculation zones originate behind these two regions. The reattachment length for these two configurations turns out to be slightly different as detailed in [59]. Considering the size of the roughness element, the downstream recirculation zone cannot be treated as a steady phenomenon. A periodic vortex shedding is expected to appear in the instantaneous velocity field, as shown in Figure 4.22. Considering the length of the Region 2 the reattachment of the flow is not occured on the top of the surface as may happen for longer rough elements.



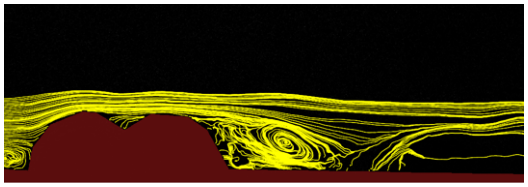
(a) Instantaneous velocity field, frame number 247



(b) Instantaneous velocity field, frame number 250



(c) Instantaneous velocity field, frame number 254



(d) Instantaneous velocity field, frame number 257

Figure 4.22: Vortex Shedding behind Spot 1 [92]

4.6 qSSHT Comparison

This section presents a comparison between the SRHT rig and the quasi-Steady State Heat Transfer (qSSHT) rig. In the qSSHT rig full-scale cooling channels are tested to assess the Nusselt enhancement. Air is used as the working fluid for both rigs, and a larger range of Reynolds numbers was tested due to the distinct experimental methodologies applied. The methodology employed is described in detail in Nepa's work [89]. The SRHT rig employes a heated main flow that transfers heat to a cold test section wall, whereas in the qSSHT rig is the actual cooling channel to be heated via Joule heating.

For this comparison, only smooth test objects were adopted. Figure 4.23 reports the Nu vs Re plot. Additionally, the Gnielinski correlation is reported, with a 10% uncertainty bar, alongside the experimental points. Three of the four experimental data points lie within the uncertainty band of the Gnielinski correlation, closely following the trend obtained from the qSSHT rig. Only for the Re = 10000 point a discrepancy is observed. Considering the experimental uncertainties in both rigs, these results demonstrate excellent agreement. This validation establishes a robust link between these two methodologies, enabling future comparisons on rough geometries.

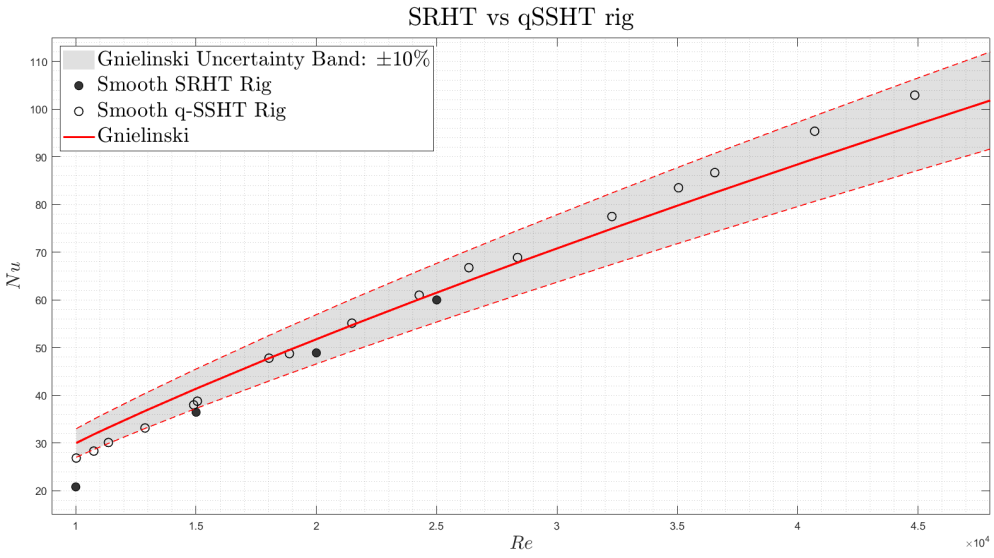


Figure 4.23: Smooth test objects comparison between SRHT and q-SSHT rigs

Chapter 5

Conclusion and Future work

5.1 Conclusion

The effect of the spatial density of the rough elements was studied for the first time in this experimental work, alongside the size of the spheres. Spatial density, also referred to as *plan solidity*, is a crucial SR parameter for heat transfer mechanisms. Its role becomes really important, especially at high Reynolds number. Previously tested geometries were re-evaluated in order to create a consistent dataset for further comparison. Thermal boundary layer measurements require more precise instrumentation to assess the impact of the upscaled surface roughness. PIV results reveal the fluid-dynamic features involved in convective heat transfer, such as recirculation zones and vortex shedding. Local heat transfer mechanisms on upscaled AM rough test objects must be studied in conjunction PIV methodology. This is because specific roughness parameters may affect heat transfer and fluid-dynamic behavior differently.

IRT is a robust methodology for investigating this topic, even when taking all measurement errors into consideration. The combined effect of R_z and λ_p has a huge impact in the HTC distribution. Finally, both R_z and λ_p prove to be major drivers of HTC enhancement. However, since distinct geometries can yield almost identical globally averaged Nu numbers, an evaluation method for PIV data must be developed to account for pressure and viscous losses.

5.2 Future Work

To further expand the number of rough models for the parametric study, new geometries were designed and presented in Figure 5.1 together with the original test objects. The criterion chosen for the design of these new models was to maximize the overlap in the $R_z/D_h - A_s/A_{tot}$ plot with respect to the existing configurations. This strategy enables a more accurate investigation of both the density and the size effects of the spherical elements on the flat surface. Consequently, the following roughness models

are proposed:

- A very low spatial density configuration of R_z 1.5 mm;
- A very low and very high spatial density configuration of R_z 3 mm;
- Five new density configurations for R_z 4.5 mm;
- Three low-density configurations for R_z 6 mm.

The goal of developing this extensive number of test objects is to find a correlation that can relate the fluid-dynamic conditions, expressed by the Reynolds number, and the most influential SR parameters, such as R_z and λ_p, with the Nusselt number. For this purpose, performing tests at higher or intermediate Reynolds numbers can increase the number of data points in the available dataset and facilitate the derivation of the empirical correlation. Other roughness parameters can be added to this correlation, once they are proven to influence the heat transfer mechanisms. The correlation can be written as a function of all of these terms, and is proposed in the following form:

$$Nu = coef \cdot \left(\frac{R_z}{D_h}\right)^a \cdot \left(\frac{A_s}{A_{tot}}\right)^b \cdot Re^n$$

A sensitivity analysis on the IR camera setup should be carried out at the most critical Reynolds number (Re = 10000). This should be combined with experimental tests to assess how spurious reflections affect the resulting HTC distribution.

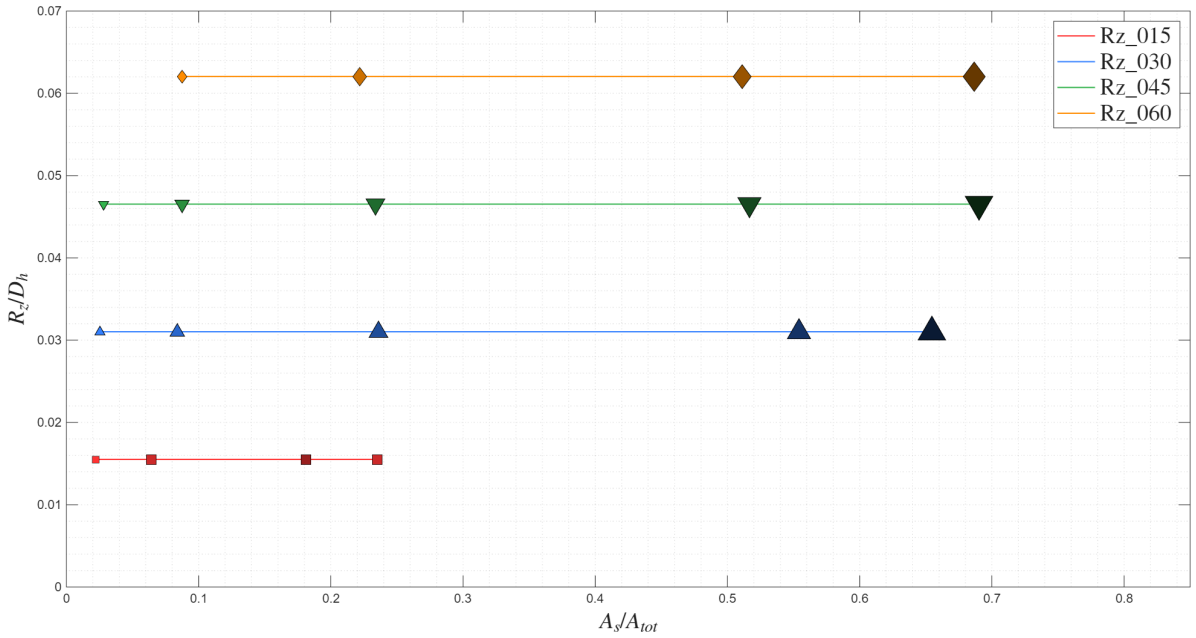


Figure 5.1: Geometrical Plot

A parallel investigation with the PIV rig should be carried out to evaluate the pressure and viscous losses of all these configurations. A better integrated thermal and

momentum boundary layer instrumentation could be integrated to the SRHT for analyzing the surface roughness impact on the temperature and velocity profile. However, this can require substantial modifications of the rig, such as creating a lateral transparent window, which can significantly modify the radiometric signal detected by the IR camera.

Bibliography

[1] G. Hagen, "Über den einfluss der temperatur auf die bewegung des wassers in röhren," *Math. Abh. Akad. Wiss. Berlin*, 1854.

[2] H. Darcy, *Recherches Expérimentales Relatives au Mouvement de l'Eau dans les Tuyaux*. Paris: Mallet-Bachelier, 1857.

[3] J. Nikuradse, "Strömungsgesetze in rauhen rohren," Verein Deutscher Ingenieure (VDI), Tech. Rep. 361, 1933.

[4] E. N. Sieder and G. E. Tate, "Heat transfer and pressure drop of liquids in tubes," *Industrial & Engineering Chemistry*, 1936.

[5] C. F. Colebrook and C. M. White, "Experiments with fluid friction in roughened pipes," *Proceedings of the Royal Society of London. Series A, Mathematical and Physical Sciences*, vol. 161, no. 906, 1937.

[6] J. Nikuradse, "Laws of flow in rough pipes," National Advisory Committee for Aeronautics (NACA), Technical Memorandum 1292, 1937.

[7] F. H. Clauser, "Turbulent boundary layers in adverse pressure gradients," *Journal of the Aeronautical Sciences*, vol. 21, no. 2, 1954.

[8] F. R. Hama, "Boundary layer characteristics for smooth and rough surfaces," *Transactions of the Society of Naval Architects and Marine Engineers*, 1954.

[9] W. D. Rannie, "Heat transfer in turbulent shear flow," *Journal of the Aeronautical Sciences*, vol. 23, no. 5, 1956.

[10] B. S. Petukhov, "Heat transfer and friction in turbulent pipe flow with variable physical properties," in *Advances in Heat Transfer*, T. F. Irvine and J. P. Hartnett, Eds., vol. 6, New York: Academic Press, 1970.

[11] B. A. Kader and A. M. Yaglom, "Heat and mass transfer laws for fully turbulent wall flows," *International Journal of Heat and Mass Transfer*, vol. 15, no. 12, 1972.

[12] T. Cebeci and A. M. O. Smith, *Analysis of Turbulent Boundary Layers*, 1st. New York: Academic Press, 1974.

[13] V. Gnielinski, "New equations for heat and mass transfer in turbulent pipe and channel flow," *International Chemical Engineering*, vol. 16, 1976.

[14] J. C. Han, L. R. Glicksman, and W. M. Rohsenow, "An investigation of heat transfer and friction for rib roughened surfaces," *International Journal of Heat and Mass Transfer*, vol. 21, no. 8, 1978.

[15] J. C. Han, J. S. Park, and C. K. Lei, "Heat transfer enhancement in channels with turbulence promoters," *ASME Journal of Engineering for Gas Turbines and Power*, vol. 107, no. 1, 1985.

[16] M. S. Bhatti and R. K. Shah, "Turbulent and transition flow convective heat transfer in ducts," in *Handbook of Single-Phase Convective Heat Transfer*, S. Kakac, R. K. Shah, and W. Aung, Eds., Hoboken, NJ: Wiley-Interscience, 1987, ch. 4.

[17] S. Kakac, "Single-phase convective heat transfer," in *Handbook of Single-Phase Convective Heat Transfer*, S. Kakac, R. K. Shah, and W. Aung, Eds., Hoboken, NJ: Wiley-Interscience, 1987, ch. 18.

[18] J. C. Han and J. S. Park, "Developing heat transfer in rectangular channels with rib turbulators," *International Journal of Heat and Mass Transfer*, vol. 31, no. 1, 1988.

[19] R. J. Moffat, "Describing the uncertainties in experimental results," *Experimental Thermal and Fluid Science*, vol. 1, no. 1, 1988.

[20] R. P. Taylor, "Surface roughness measurements on gas turbine blades," in *ASME Turbo Expo: Power for Land, Sea, and Air*, ASME Technical Paper, New York, NY: American Society of Mechanical Engineers, 1989.

[21] J.-C. Han and Y. M. Zhang, "High performance heat transfer ducts with parallel broken and V-shaped broken ribs," *International Journal of Heat and Mass Transfer*, vol. 35, no. 2, 1992.

[22] R. H. S. Winterton, "Where did the Dittus–Boelter equation come from?" *International Journal of Heat and Mass Transfer*, vol. 41, no. 4-5, 1998.

[23] C. S. B. Grimmond and T. R. Oke, "Aerodynamic properties of urban areas derived from analysis of surface form," *Journal of Applied Meteorology*, 1999.

[24] E. S. Gadelmawla, M. M. Koura, T. M. A. Maksoud, I. M. Elewa, and H. H. Soliman, "Roughness parameters," *Journal of Materials Processing Technology*, 2002.

[25] M. P. Schultz, J. A. Finlay, M. E. Callow, and J. A. Callow, "Three models to relate detachment of low form fouling at laboratory and ship scale," *Biofouling*, vol. 25, no. 1-2, 2003.

[26] B. Hof et al., *Science*, vol. 305, 2004.

[27] W. M. Kays, M. E. Crawford, and B. Weigand, *Convective Heat and Mass Transfer*, 4th. New York: McGraw-Hill, 2005.

[28] Y. A. Çengel and M. A. Boles, *Thermodynamics: An Engineering Approach*, Fifth. New York, NY: McGraw-Hill, 2006, ISBN: 978-0-07-288495-1.

[29] F. Liebmann, *Infrared calibration development at fluke corporation hart scientific division*, Technical Paper, Fluke Corporation, Hart Scientific Division, 799 Utah Valley Drive, American Fork, Utah 84003, 2007.

[30] J. M. Crosby, S. Lewis, J. P. Bons, W. Ai, and T. H. Fletcher, "Effects of temperature and particle size on deposition in land based turbines," *Journal of Engineering for Gas Turbines and Power*, vol. 130, no. 5, 2008.

[31] E. Napoli, V. Armenio, and M. De Marchis, "The effect of the slope of irregularly distributed roughness elements on turbulent wall-bounded flows," *Journal of Fluid Mechanics*, vol. 613, 2008.

[32] A. Bewoor and V. Kulkarni, *Metrology and Measurement*. New Delhi: McGraw-Hill Education, 2009.

[33] R. J. Volino, M. P. Schultz, and K. A. Flack, "Turbulence structure in a boundary layer with two-dimensional roughness," *Journal of Fluid Mechanics*, vol. 635, 2009.
[34] K. A. Flack and M. P. Schultz, "Review of hydraulic roughness scales in the fully rough regime," *Journal of Fluids Engineering*, vol. 132, no. 4, 2010.
[35] Y. Wu and K. T. Christensen, "Spatial structure of a turbulent boundary layer with irregular surface roughness," *Journal of Fluid Mechanics*, vol. 655, 2010.
[36] M. P. Boyce, *Gas Turbine Engineering Handbook*, Fourth. Oxford, UK: Elsevier / Butterworth-Heinemann, 2011, ISBN: 978-0-12-383842-1.
[37] F. P. Incropera, D. P. DeWitt, T. L. Bergman, and A. S. Lavine, *Fundamentals of Heat and Mass Transfer*, 7th ed. Hoboken, NJ: John Wiley & Sons, 2011.
[38] ASTM Committee F42 on Additive Manufacturing Technologies, *Standard Terminology for Additive Manufacturing Technologies*, West Conshohocken, PA: ASTM International, 2012.
[39] J.-C. Han, S. Dutta, and S. Ekkad, *Gas Turbine Heat Transfer and Cooling Technology*, 2nd. Boca Raton, FL: CRC Press, 2012, ISBN: 978-1439855669.
[40] E. et al., "Combined experimental and numerical method using infrared thermography and finite element analysis for estimation of local heat transfer distribution in an internal cooling system," in *Proceedings of the ASME Turbo Expo 2013: Turbine Technical Conference and Exposition*, vol. Volume 3B: Heat Transfer, San Antonio, Texas, USA: American Society of Mechanical Engineers, 2013.
[41] S. Hohenstein, J. Aschenbruck, and J. Seume, "Aerodynamic effects of non-uniform surface roughness on a turbine blade," in *Proceedings of ASME Turbo Expo 2013: Turbine Technical Conference and Exposition*, ser. GT2013-95433, San Antonio, Texas, USA: ASME, 2013.
[42] L. M. Wright and J.-C. Han, "Heat transfer enhancement for turbine blade internal cooling," in *Proceedings of the ASME 2013 Heat Transfer Summer Conference (HT2013)*, ser. HT2013-17813, Minneapolis, MN, USA: ASME, 2013.
[43] Y. Wu, H. Ren, and H. Tang, "Turbulent flow over a rough backward-facing step," *International Journal of Heat and Fluid Flow*, vol. 44, 2013.
[44] K. A. Flack and M. P. Schultz, "Roughness effects on wall-bounded turbulent flows," *Physics of Fluids*, vol. 26, 2014.
[45] J. Yuan and U. Piomelli, "Estimation and prediction of the roughness function on realistic surfaces," *Journal of Turbulence*, vol. 15, no. 6, 2014.
[46] K. Bhaganagar and L. Chau, "Characterizing turbulent flow over 3-D idealized and irregular rough surfaces at low Reynolds number," *Applied Mathematical Modelling*, vol. 39, 2015.
[47] I. Gibson, D. Rosen, and B. Stucker, *Additive Manufacturing Technologies: 3D Printing, Rapid Prototyping, and Direct Digital Manufacturing*, Second. New York, NY: Springer, 2015, ISBN: 978-1-4939-2112-6.
[48] C. K. Stimpson, J. C. Snyder, K. A. Thole, and D. Mongillo, "Roughness effects on flow and heat transfer for additively manufactured channels," in *Proceedings of ASME Turbo Expo 2015: Turbine Technical Conference and Exposition*, ser. GT2015-43940, Montréal, Canada: ASME, 2015.

[49] B. Lane and E. Whitenton, "Calibration and measurement procedures for a high magnification thermal camera," National Institute of Standards and Technology (NIST), Gaithersburg, MD, NIST Interagency/Internal Report NISTIR 8098, 2016.
[50] C. K. Stimpson, J. C. Snyder, K. A. Thole, and D. Mongillo, "Scaling roughness effects on pressure loss and heat transfer of additively manufactured channels," in *Proceedings of ASME Turbo Expo 2016: Turbomachinery Technical Conference and Exposition*, ser. GT2016-58093, Seoul, South Korea: ASME, 2016.
[51] P. Forooghi, A. Stroh, F. Magagnato, S. Jakirlić, and B. Frohnapfel, "Toward a universal roughness correlation," *Journal of Fluids Engineering, Transactions of the ASME*, vol. 139, no. 12, 2017.
[52] P. Jaksch, "Implementation of an adjoint thermal solver for inverse problems," in *Proceedings of 12th European Conference on Turbomachinery Fluid Dynamics & Thermodynamics ETC12*, Paper ID: ETC2017-336, Siemens Industrial Turbomachinery AB, Stockholm, Sweden, 2017.
[53] S. Naik, "Basic aspects of gas turbine heat transfer," in *Gas Turbines*, IntechOpen, 2017, ch. 6.
[54] H. Schlichting and K. Gersten, *Boundary-Layer Theory*, 9th ed. Springer, 2017.
[55] 3D Systems, *Accura® xtreme™, Ultra-tough grey plastic with outstanding durability, accuracy and aesthetics to replace cnc-machined polypropylene and abs articles*, 3D Systems, Inc., 2018.
[56] J.-M. Clemenson, T. A. Shannon, and S. T. McClain, "A novel method for constructing analog roughness patterns to replicate ice accretion characteristics," in *AIAA AVIATION Forum*, ser. 2018 Atmospheric and Space Environments Conference, Atlanta, Georgia: American Institute of Aeronautics and Astronautics, 2018.
[57] H. W. Coleman and W. G. Steele, *Experimentation, validation, and uncertainty analysis for engineers*, 4th. John Wiley & Sons, 2018.
[58] A. W. Gebisa and H. G. Lemu, "Additive manufacturing for the manufacture of gas turbine engine components: Literature review and future perspectives," in *Proceedings of the ASME Turbo Expo 2018: Turbomachinery Technical Conference and Exposition*, Oslo, Norway: ASME, 2018.
[59] J. van der Kindere et al., "Effect of length of two-dimensional obstacles on characteristics of separation and reattachment," *Journal of Wind Engineering and Industrial Aerodynamics*, vol. 178, 2018.
[60] M. Papapetrou, G. Kosmadakis, A. Cipollina, U. La Commare, and G. Micale, "Industrial waste heat: Estimation of the technically available resource in the EU per industrial sector, temperature level and country," *Applied Thermal Engineering*, vol. 138, 2018.
[61] S. Tickoo, *Siemens NX 12.0 for Designers*, 11th. Schererville, Indiana: CADCIM Technologies, 2018, ISBN: 978-1942689997.
[62] P. Jaksch, *C3d manual: Turbine cooling program c3d v. 3.0*, Technical report, Siemens Industrial Turbomachinery, Finspång, Sweden, 2019.

[63] O. Léon, P. Reulet, and F. Chedevergne, "Aerodynamic and heat transfer effects of distributed hemispherical roughness elements inducing step changes in a turbulent boundary layer," *International Journal of Heat and Fluid Flow*, vol. 85, 2020.
[64] E. Magsipoc, Q. Zhao, and G. Grasselli, "2d and 3d roughness characterization," *Rock Mechanics and Rock Engineering*, vol. 53, 2020.
[65] V. Navrotsky, S. Piegert, I. Fedorov, and O. Naryzhnyy, "Gas turbines performance improvement enabled by additive manufacturing," in *Technical Publication*, Siemens Energy AB and Siemens Energy AG, Finspång, Sweden and Berlin, Germany, 2020.
[66] Z. Qu, P. Jiang, and W. Zhang, "Development and application of infrared thermography non-destructive testing techniques," *Sensors*, vol. 20, no. 13, 2020.
[67] S. K. Saha, H. Ranjan, M. S. Emani, and A. K. Bharti, "2d roughness, 3d roughness and roughness applications," in *SpringerBriefs in Applied Sciences and Technology*, Springer Verlag, 2020.
[68] J. C. Snyder and K. A. Thole, "Effect of additive manufacturing process parameters on turbine cooling," *Journal of Turbomachinery*, 2020, Department of Mechanical Engineering, The Pennsylvania State University.
[69] International Organization for Standardization, "Geometrical product specifications (gps) – ISO Standard No. ISO 25178-2:2021," International Organization for Standardization, Geneva, Switzerland, Standard ISO 25178-2:2021, 2021.
[70] M. Kadivar, D. Tormey, and G. McGranaghan, "A review on turbulent flow over rough surfaces: Fundamentals and theories," *International Journal of Thermofluids*, vol. 10, 2021.
[71] T. Medjnoun, E. Rodriguez-Lopez, M. A. Ferreira, T. Griffiths, J. Meyers, and B. Ganapathisubramani, "Turbulent boundary-layer flow over regular multiscale roughness," *Journal of Fluid Mechanics*, vol. 917, 2021.
[72] International Energy Agency, "World energy outlook 2022," IEA, Paris, Report, 2022. [Online]. Available: `https://www.iea.org/reports/world-energy-outlook-2022`
[73] R. Pagani, "Experimental analysis of the thermal and hydraulic performance in straight and complex additively manufactured mini-channels," Master's thesis, Politecnico di Milano, 2022.
[74] U. Unnikrishnan and V. Yang, "A review of cooling technologies for high temperature rotating components in gas turbine," *Propulsion and Power Research*, vol. 11, no. 3, 2022.
[75] S. T. Vagge and S. Ghogare, "Thermal barrier coatings: Review," *Materials Today: Proceedings*, vol. 56, 2022.
[76] L. Zhou et al., "Additive manufacturing: A comprehensive review," *Sensors*, 2022.
[77] P. V. Lehmann, "Investigation of the local heat transfer characteristics on additively manufactured surfaces using infrared thermography," Ph.D. dissertation, Technical University of Munich, Munich, Germany, 2023.
[78] S. Pirozzoli, "Prandtl number effects on passive scalars in turbulent pipe flow," *Journal of Fluid Mechanics*, vol. 965, 2023.

[79] K. Wen, "Investigation of roughness effects on heat transfer of upscaled additively manufactured channels in the turbulent region using infrared thermography," Ph.D. dissertation, KTH Royal Institute of Technology, Stockholm, Sweden, 2023.

[80] A. J. Wildgoose, K. A. Thole, E. Tuneskog, and L. Wang, "Roughness related to cooling performance of channels made through additive manufacturing," in *Proceedings of ASME Turbo Expo 2023: Turbomachinery Technical Conference and Exposition*, ser. GT2023-103151, Boston, Massachusetts, USA: ASME, 2023.

[81] M. Abdelaziz, L. Djenidi, M. H. Ghayesh, and R. Chin, "On predictive models for the equivalent sand grain roughness for wall-bounded turbulent flows," *Physics of Fluids*, vol. 36, no. 1, 2024.

[82] A. Brogliato, "Investigation of the effect of additive manufacturing induced surface roughness on local heat transfer properties using ir thermography," Master's Degree Thesis, Politecnico di Torino, Turin, Italy, 2024.

[83] S. A. Dixit, A. Gupta, H. Choudhary, and T. Prabhakaran, "Generalized scaling and model for friction in wall turbulence," *Physical Review Letters*, vol. 132, 2024.

[84] A. Pedreño Marín, "Piv flow measurements for heat transfer characterization in upscaled am surface roughness," Ph.D. dissertation, TU Delft, Delft, Netherlands, 2024.

[85] D. Chung, N. Hutchins, M. P. Schultz, and K. A. Flack, "Predicting the drag of rough surfaces," *Annual Review of Fluid Mechanics*, vol. 57, 2025.

[86] F. Gissi, "Infrared thermography-based heat transfer analysis and thermal boundary layer evaluation on upscaled models of additively manufactured rough surfaces," Master's Degree Thesis, Politecnico di Torino, Turin, Italy, 2025.

[87] M. Kadivar and H. Garg, "Turbulent heat transfer over roughness: A comprehensive review of theories and turbulent flow structure," *International Journal of Thermofluids*, vol. 26, 2025.

[88] M. Kadivar, D. Tormey, and G. McGranaghan, "Influence of roughness density and prandtl number on convective heat transfer over artificial additive manufactured roughness," *Applied Thermal Engineering*, vol. 275, 2025.

[89] A. Nepa, "Heat transfer in air throug additively manufactured channels: Experimental evaluation of nusselt number via a coupled thermal-electric star-ccm+ model," M.S. thesis, Politecnico di Torino, 2025.

[90] O. Zhdanov, T. O. Jelly, and A. Busse, "Impact of windward and effective slope on the roughness effect of ratchet-type surfaces in turbulent channel flow," *International Journal of Heat and Fluid Flow*, vol. 116, 2025.

[91] M. Jankovskis, "Investigation of the effects of additive manufacturing-induced surface roughness on local heat transfer properties," Master's Degree Thesis, School of Industrial Engineering and Management, Stockholm, Sweden, 2026.

[92] Y. Mazed, "Investigating the velocity field close to an upscaled additively manufacturing induced roughness surface utilizing particle image velocimetry," Master's Degree Thesis, INSA Hauts de France, 2026.

[93] Siemens Energy. “Sgt-700 gas turbine for power generation and mechanical drive,” Accessed: Jun. 12, 2026. [Online]. Available: https://www.siemens-energy.com/global/en/home/products-services/product/sgt-700.html
[94] Astarita and Carlomagno, *Infrared Thermography for Thermo-Fluid-Dynamics*.
[95] ATTS Inc., *Gas turbine parts & their functions (explained in simple language)*, Accessed: May 2026. [Online]. Available: https://www.atts-inc.com
[96] DIAS Infrared Systems, *Pyrotherm cs 110: Infrared calibration source / black body*, Technical datasheet, accessed September 2025, DIAS Infrared Systems, Dresden, Germany. [Online]. Available: https://www.dias-infrared.com
[97] H. Schlichting, “Experimentelle untersuchungen zum rauhigkeitsproblem,”

Nomenclature

Acronyms / Abbreviations

Symbol	Description
AM	Additive Manufacturing
APS	Air Plasma Spray
CAD	Computer-Aided Design
CNC	Computer Numerical Control
DAS	Data Acquisition System
DMD	Direct Metal Deposition
DMLS	Direct Melting Laser Sintering
CFD	Computational Fluid Dynamics
EBM	Electron Beam Melting
EBPVD	Electron Beam Physical Vapor Deposition
FIR	Far Infrared
FOV	Field of View
FPA	Focal Plane Array
HTC	Heat Transfer Coefficient
IR	Infrared
IT	Integration Time
IRT	Infrared Thermography
LIR	Long Infrared
L-PBF	Laser Powder Bed Fusion
MCM	Monte Carlo Method
MIR	Middle Infrared

Symbol	Description
NIR	Near Infrared
NZE	Net Zero Emission
PIV	Particle Image Velocimetry
qSSHT	Quasi-Steady State Heat Transfer
ROI	Region of Interest
RTD	Resistance Temperature Detector
SEM	Scanning Electron Microscope
SLA	Stereolithography
SLM	Selective Laser Melting
SLS	Selective Laser Sintering
SR	Surface Roughness
SRHT	Surface Roughness Heat Transfer
STL	Standard Tessellation Language
TBC	Thermal Barrier Coating
TIT	Turbine Inlet Temperature
TSM	Taylor Series Method

Dimensionless Numbers

Symbol	Description	Definition
k_s^+	Roughness height in viscous units	$\frac{k_s u_\tau}{\nu}$
Nu	Nusselt number	$\frac{hD_h}{k}$
Pr	Prandtl number	$\frac{\nu}{\alpha}$
Pr_t	Turbulent Prandtl number	$\frac{\epsilon_M}{\epsilon_H}$
Re	Reynolds number	$\frac{u_\infty D}{\nu}$
x/D_h	Dimensionless streamwise coordinate	$\frac{x}{D_h}$

Symbols

Symbol	Description	Units
A	Cross-sectional area	m^2
α	Thermal diffusivity	m^2/s
C_f	Fanning coefficient	1
c_p	Specific heat capacity	$J/(kg \cdot K)$
D_h	Hydraulic diameter	m
δ	Momentum Boundary Layer Thickness	m
δ_T	Thermal Boundary Layer Thickness	m
ΔU^+	Velocity shift in wall units	1
ϵ_H	Thermal eddy diffusivity	m^2/s
ϵ_M	Momentum eddy diffusivity	m^2/s
f_D	Darcy friction factor	1
h	Convective heat transfer coefficient	$W/(m^2K)$
k	Thermal conductivity	W/(mK)
k_s	Equivalent sand-grain roughness height	m
λ_f	Frontal solidity	1
$\dot{m}$	Mass flow rate	g/s
μ	Dynamic viscosity	$Pa \cdot s$
ν	Kinematic viscosity	m^2/s
$\dot{q}$	Heat flux	W/m^2
ρ	Fluid density	kg/m^3
r_p	Pressure rattio	1
τ_w	Wall shear stress	Pa
T	Absolute Temperature	K
T_w	Wall Surface Temperature	K
T_∞	Bulk Temperature	K
θ^+	Non-dimensional temperature in inner units	1
$\bar{U}$	Bulk velocity	m/s
u_∞	Free stream velocity	m/s
u^+	Non-dimensional velocity in inner units	1
y^+	Wall-normal coordinate in inner units	1